ORNL/TM-2014/310

FY14 Status Report: CIRFT Testing Results on High Burnup UNF

Fuel Cycle Research & Development

Prepared for
US Department of Energy
Used Fuel Disposition Campaign
J.-A. Wang, H. Wang, and H. Jiang
B. B. Bevard and R. L. Howard
Oak Ridge National Laboratory

September 2014
M2-FCRD-UFD-2014-000053

DOCUMENT AVAILABILITY

Reports produced after January 1, 1996, are generally available free via US Department of Energy (DOE) SciTech Connect.

Website http://www.osti.gov/scitech/

Reports produced before January 1, 1996, may be purchased by members of the public from the following source:

National Technical Information Service
5285 Port Royal Road
Springfield, VA 22161
Telephone 703-605-6000 (1-800-553-6847)
TDD 703-487-4639
Fax 703-605-6900
E-mail info@ntis.gov
Website http://www.ntis.gov/help/ordermethods.aspx

Reports are available to DOE employees, DOE contractors, Energy Technology Data Exchange representatives, and International Nuclear Information System representatives from the following source:

Office of Scientific and Technical Information
PO Box 62
Oak Ridge, TN 37831
Telephone 865-576-8401
Fax 865-576-5728
E-mail reports@osti.gov
Website http://www.osti.gov/contact.html

This report was prepared as an account of work sponsored by an agency of the United States Government. Neither the United States Government nor any agency thereof, nor any of their employees, makes any warranty, express or implied, or assumes any legal liability or responsibility for the accuracy, completeness, or usefulness of any information, apparatus, product, or process disclosed, or represents that its use would not infringe privately owned rights. Reference herein to any specific commercial product, process, or service by trade name, trademark, manufacturer, or otherwise, does not necessarily constitute or imply its endorsement, recommendation, or favoring by the United States Government or any agency thereof. The views and opinions of authors expressed herein do not necessarily state or reflect those of the United States Government or any agency thereof.

ORNL/TM-2014/310

Materials Science and Technology Division

FY14 Status Report: CIRFT Testing Results on High Burnup UNF

Jy-An John Wang, Hong Wang, and Hao Jiang

Program Managers
Bruce Bevard and Rob Howard

Date Published: September 2014

Prepared by
OAK RIDGE NATIONAL LABORATORY
Oak Ridge, Tennessee 37831-6283
managed by
UT-BATTELLE, LLC
for the
US DEPARTMENT OF ENERGY
under contract DE-AC05-00OR22725

This page intentionally left blank.

CONTENTS

FIGURES

This page intentionally left blank.

TABLES

This page intentionally left blank.

ABBREVIATIONS

CIRFT	Cyclic Integrated Reversible-Bending Fatigue Tester
DOE	Department of Energy
FCRD	Fuel Cycle Research & Development
FEA	finite element analysis
FY	fiscal year
GWd/MTU	gigawatt-days per megaton of uranium
HBR	H. B. Robinson
HBU	high burn-up
LVDT	linear variable differential transformer
MOX	mixed oxide
NA	North Anna
NCT	normal conditions of transport
NRC	US Nuclear Regulatory Commission
NUREG	NRC Regulatory Guide
NUREG/CR	NRC Regulatory Guide Contractor Prepared
ORNL	Oak Ridge National Laboratory
PCI	peripheral component interconnect
PIE	post-irradiation examination
PNNL	Pacific Northwest National Laboratory
PPI	pellet-to-pellet interface
SNF	spent nuclear fuel
SS	stainless steel
SSAP	stainless steel alumina pellets
TDD	telecommunications devices for the deaf
UFDC	Used Fuel Disposition Campaign
UNF	used nuclear fuel

This page intentionally left blank.

SUMMARY

The objective of this project is to perform a systematic study of used nuclear fuel (UNF, also known as “spent nuclear fuel” [SNF]) integrity under simulated transportation environments using the Cyclic Integrated Reversible-Bending Fatigue Tester (CIRFT) hot-cell testing technology developed at Oak Ridge National Laboratory (ORNL) in August 2013. Under Nuclear Regulatory Commission (NRC) sponsorship, ORNL completed four benchmark tests, four static tests, and twelve dynamic or cycle tests on H. B. Robinson (HBR) high burn-up (HBU) fuel. The clad of the HBR fuels was made of Zircaloy-4. Testing was continued in fiscal year (FY) 2014 using Department of Energy (DOE) funds. The additional CIRFT was conducted on three HBR rods (R3, R4, and R5) in which two specimens failed and one specimen was tested to over 2.23×10^{7} cycles without failing. The data analysis on all the HBR UNF rods demonstrated that it is necessary to characterize the fatigue life of the UNF rods in terms of (1) the curvature amplitude and (2) the maximum absolute of curvature extremes. The maximum extremes are significant because they signify the maximum of tensile stress for the outer fiber of the bending rod. CIRFT testing has also addressed a large variation in hydrogen content on the HBR rods. While the load amplitude is the dominant factor that controls the fatigue life of bending rods, the hydrogen content also has an important effect on the lifetime attained at each load range tested.

A preliminary post-irradiation examination (PIE) was conducted on some selected rod segment specimens. This provided data on fracture systems within pellets, pellet-to-pellet interaction (PPI) conditions, and hydride effects on the failure of the test specimens.

A new vise mold was designed and fabricated to support CIRFT testing of both North Anna M5^{TM} (NA) and mixed oxide (MOX) M5^{TM} fuel/cladding. Epoxy casting in the hot cell demonstrated that the second vise mold works just as effectively as the one used for HBR fuel. Therefore, the ORNL hot cell is equipped with two vise molds, enabling rod specimen preparation for various diameters of UNF rods.

The static tests on NA and MOX UNF were carried out under a displacement control: relative maximum displacement of 24.00 mm (12.00 mm at each motor), with a loading rate of 0.1 mm/s, followed by an unloading rate of 0.2 mm/s at each loading point of the U-frame. Both fuel rods survived the static loading for two to four cycles. The moment-curvature curves reflected that a significant nonlinear deformation occurred after 30 N·m; a maximum moment of 47 N·m was attained during the initial loading cycle. A deflection point appeared at approximately 8 N·m in the initial loading cycle. The maximum curvature under relative displacement of 24.00 mm was 3.85–4.10 m^{-1}. The maximum equivalent stress and strain were 520–522 MPa and 1.8–2.0%, respectively.

Seven dynamic tests at 5 Hz were conducted in the hot cell: on three NA M5 ^{TM} specimens and four MOX specimens. The moment amplitudes tested were 5.08–12.70 N·m, and the curvature amplitudes were 0.200–0.55 m^{-1}. The equivalent stress amplitudes were 59.12–142.37 MPa, and equivalent strain amplitudes were 0.10–0.27 %. During these tests, the fatigue life of the rods decreased from 2.15×10^{6} to 1.57×10^{4} cycles. Furthermore, the dynamic test also reveals the accelerated aging induced by the potential handling drop or transient shocks of normal conditions of transport (NCT) that occur in addition to the normal vibration.

Out-of-cell testing continues to support the ongoing ORNL hot-cell testing. A number of important issues have been identified that come from both the test system and the rod fuel itself. Research in a hot cell of some of these issues is prohibitive due to high cost and limited access. Therefore, the out-of-cell CIRFT system is being used for these studies.

This report provides discussions and theories concerning the impact of the interface bonding efficiency on UNF vibration integrity based on a series of finite element analysis (FEA) simulations on M5^{TM} clad. This

includes the distribution of moment-carrying capacity between pellets and clad and the impact of the interface material on the flexural rigidity of the M5^{TM} fuel rod system. The detailed FEA results of characterizing the interface bonding efficiency on a UNF rod system are summarized in the table below.

The flexural rigidity comparison between the different bonding and debonding cases

Interface bonding conditions	**Flexural rigidity *EI* (N·m^2)**	**Reduction from perfect bond (%)**	**Reduction from only pellet-pellet debond to further pellet-clad debond (%)**	**Increase from with gaps to without gaps (%)**
Perfect bond	44			
Pellet-pellet interface with gap debond, pellet-clad interface bonded	32	27		
Pellet-pellet interface without gap debond, pellet-clad interface bonded	40	9		20
Pellet-pellet interface with gap debond, pellet-clad interface debonded	16.5	62.5	48	
Pellet-pellet interface without gap debond, pellet-clad interface debonded	26.5	40	34	38

As the Young’s modulus of the interface material increases, the fuel rod system stiffness increases accordingly. As debonding of the pellet-clad interface advances, the impact of the interface material property change is limited. The immediate consequences of interface debonding are (1) a shift in load-carrying capacity from the fuel pellets to the clad and (2) a reduction in composite rod system flexural rigidity. Therefore, the flexural rigidity of the fuel rod and the bending moment resistance capacity between the clad and fuel pellets are highly dependent on the interface bonding efficiency at the pellet-pellet and pellet-clad interfaces.

USED FUEL DISPOSITION CAMPAIGN

FY14 STATUS REPORT: CIRFT TESTING RESULTS ON HIGH BURNUP UNF

1 BACKGROUND

The objective of this project is to perform a systematic study of used nuclear fuel (UNF) integrity under simulated transportation environments (normal conditions of transport [NCT]) using hot-cell testing technology developed at the Oak Ridge National Laboratory (ORNL)—the Cyclic Integrated Reversible-Bending Fatigue Tester (CIRFT) [1–9]. Currently, the CIRFT testing on UNF is conducted at an ORNL hot-cell testing facility.

Under Nuclear Regulatory Commission (NRC) sponsorship, ORNL completed four benchmark tests, four static tests, and twelve dynamic or cycle tests on H. B. Robinson (HBR) high burn-up (HBU) fuel. The clad of the HBR fuel was made of Zircalloy-4. The related testing results will be documented in an NRC regulatory guide contractor-prepared (NUREG/CR) report. With support from the US Department of Energy (DOE), the CIRFT work has continued on remaining HBR rods. The CIRFT testing on North Anna (NA) M5 $^{\text{TM}}$and mixed oxide (MOX) M5$^{\text{TM}}$ UNF were also initiated in the reporting period. At the same time, ORNL conducted post-irradiation examination (PIE) of selected HBR rod segment/tested specimens, along with fractography on tested NA M5$^{\text{TM}}$ and MOX fuels.

While the use of CIRFT on HBR UNF rods generated a lot of interesting data, a number of important issues remain to be addressed. Because direct examination of some of these issues in a hot cell is prohibitive due to high cost and limited access, out-of-cell study has been demonstrated to be cost effective and much more feasible. A testing system with the same configuration as that of CIRFT used in a hot cell has been developed to study the issues that emerged from hot-cell testing and also to investigate the fatigue and failure mechanisms of UNF rods that cannot be identified directly in hot-cell testing.

The development of hardware and software, CIRFT test results on HBR fuel rods, NA M5$^{\text{TM}}$ fuel rods, and MOX fuel rods will be discussed in this report.

2 DEVELOPMENT OF HARDWARE AND SOFTWARE

2.1 Progress on the Second CIRFT

As an efficient, economical means to understand the failure mechanisms of UNF undergoing NCT, a second CIRFT machine was manufactured. The second machine has the same configuration as the first, except the regular linear variable differential transformers (LVDTs) used for the Bose machine control were replaced with rad-hardened LVDTs. After several cycles of qualification and acceptance testing, the second CIRFT was assembled in December 2013 [10].

The system consists of a dual LM2 Bose test bench and U-frame testing setup. It is equipped with three LVDTs to measure deflections and record curvature measurement. Two 3000 N load cells and two 12.5-mm LVDTs are used in the Bose machine for control and measurement. The U-frame has a 101.60-mm loading arm and three curvature LVDTs with ±5-mm measurement range. The overall setup, power module, peripheral component interconnect (PCI)-82 controller, three curvature LVDT amplifiers, and power supports are shown in Figs. 1–3.

Testing using surrogate rods demonstrated that the system runs quite stably.

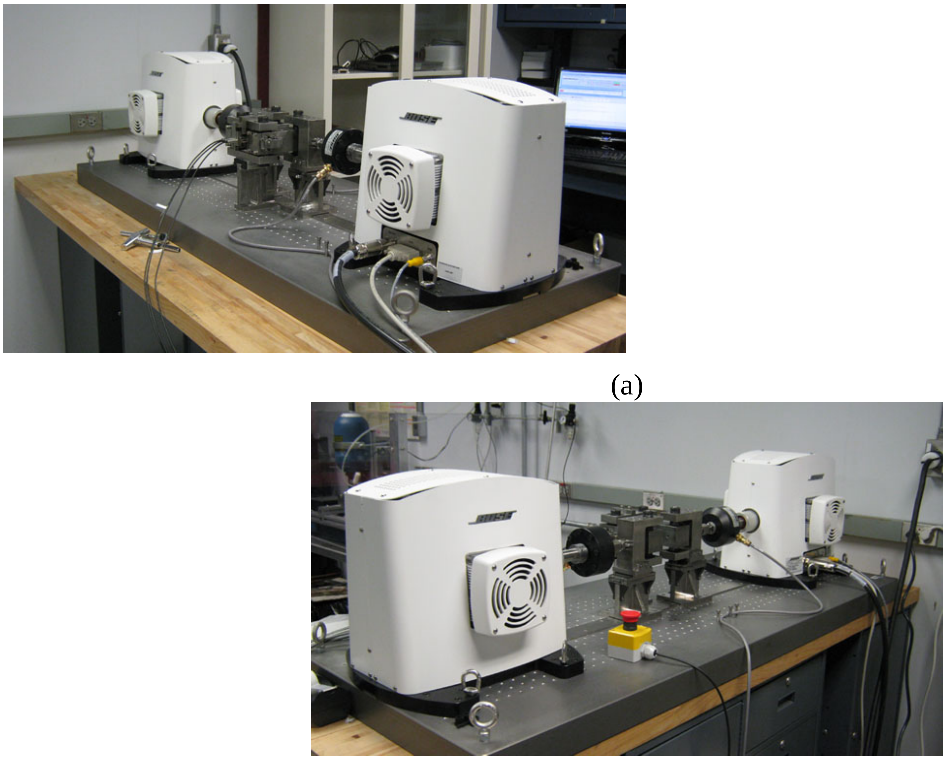

(a)

(b)

Fig. 1. (a) Front and (b) back views of assembled U-frame attached to Bose dual LM2 test bench.

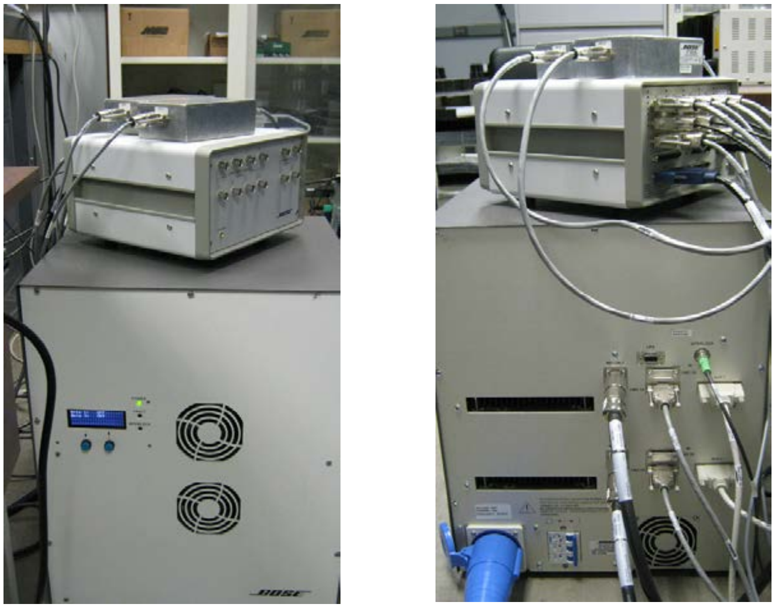

(a) (b)

Fig. 2 (a) Front and (b) back views of the power module, PCI-82 controller, and LM2 LVDT amplifiers.

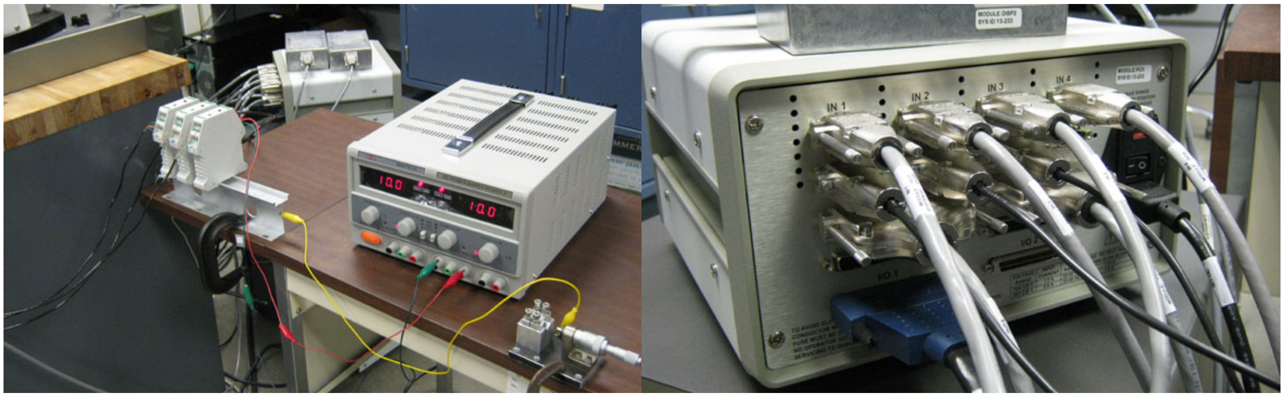
(a) (b)

Fig. 3. (a) Amplifier, power supply, and calibration setup of three curvature LVDTs, and (b) the integrated channels of LM2 load cells, LM2 LVDTs, and three curvature LVDTs integrated into the Bose PCI controller.

2.2 Data Processing

Measurement data and online monitoring data were converted into applied moment and curvature based on the load channel output (load 1 and load 2), the loading arm (101.60 mm), and LVDT channels (LVDT 1, 2, and 3) output. The moment (*M*) was estimated by:

$$M = F \times L \tag{1}$$

where *F* is the averaged value of applied loads (load 1 and load 2) from Bose dual motors, and *L* is the loading arm, 101.60 mm. The curvature (κ) was estimated using Eq. (2).

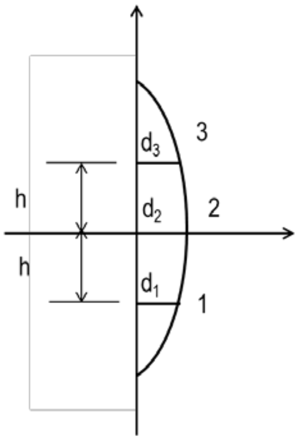

The curvature κ can be defined by the radius of circle as follows

$$\kappa = 1/R \tag{2}$$

The parameters of circle equation can be estimated based on the deflections measured by three LVDTs, d$_1$, d$_2$, d$_3$:

$$R = \sqrt{(x_0 - d_2)^2 + y_0^2}$$

$$x_0 = \frac{-2m_a m_b h - m_a(d_2 + d_3) + m_b(d_1 + d_2)}{2(m_b - m_a)}$$

$$y_0 = -\frac{1}{m_a}\left(x_0 - \frac{d_1 + d_2}{2}\right) - \frac{h}{2}$$

where

$$m_a = \frac{h}{d_2 - d_1} \qquad m_b = \frac{h}{d_3 - d_2}$$

The equivalent strain-stress curves were obtained under the assumption that the UNF rod can be idealized as a linear elastic homogeneous material without the consideration of the effects induced by any pellet-cladding interaction. The equivalent stress was calculated by:

$$\sigma = M \times y_{max}/I \tag{3}$$

where I is the moment of inertia, $I = I_c + I_p$, and I_c and I_p are moments of inertia of the cladding and pellet, respectively, and y_{max} is the maximum distance to the neutral axis of the test rod of the section measured by the radius of the cladding. The calculation of stress disregards the difference of elastic moduli between the cladding and the pellets.

The equivalent strain was calculated by:

$$\varepsilon = \kappa \times y_{max}. \tag{4}$$

2.3 Effect of Probe Contact on Large Curvature Measurements

The effect of the LVDT probe contact with the test specimen when taking curvature measurements may be an important test attribute when the curvature becomes large and bending is reversed.

An experimental study was performed using two surrogate rods made of the comprising materials and same configuration (stainless steel [SS] tube and ten alumina pellets [AP], or SSAP), and the same flat probe contact was used as seen in Fig. 4.


(a) (b) (c)

Fig. 4. (a) Three curvature LVDTs being held against the rod; (b) LVDT clamp open to show (b) flat probe and (c) chisel probe.

In order to study the effect of reverse bending on curvature measurement, the rod was subjected to both positive (concave) and negative (convex) bending of the three LVDTs. In the case of convex bending, the rod was bent toward the three LVDTs. Three RDP brand D5/200AG-337 LVDTs with a stroke of ±5 mm were used in the testing.

As shown in Fig. 5, under a similar level of applied moment, the maximum curvature obtained is significantly larger when a rod is bending concavely with respect to the LVDTs than when a rod is bending convexly. The discrepancy can be corrected by adjusting sensor spacing h, as illustrated in Fig. 6. The moment-curvature curves in both cases converge if a sensor spacing adjustment Δh of 2.5 mm is used (21% of sensor spacing h and a little less than the contact radius of 3.0 mm). Of course, the actual sensor spacing adjustment can be calibrated, while the study demonstrated that the curvature based on flat-probe contact can be corrected if necessary.

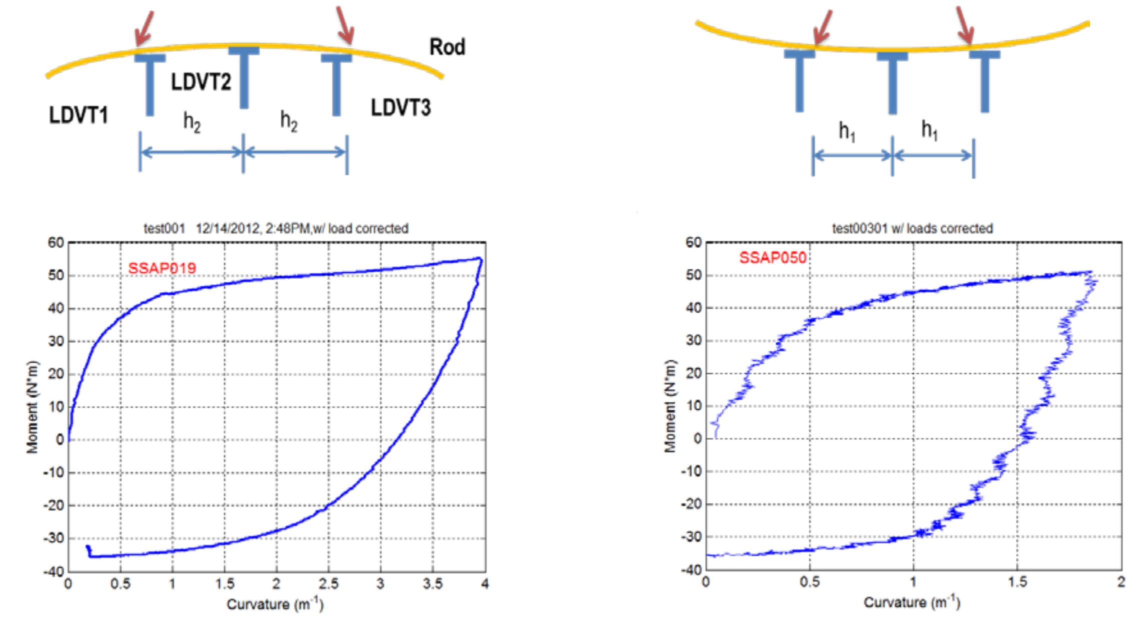

(a) (b)

Fig. 5. Moment-curvature curves based on SSAP rod testing when the rod is bending with respect to three LVDTs (a) concave and (b) convex.

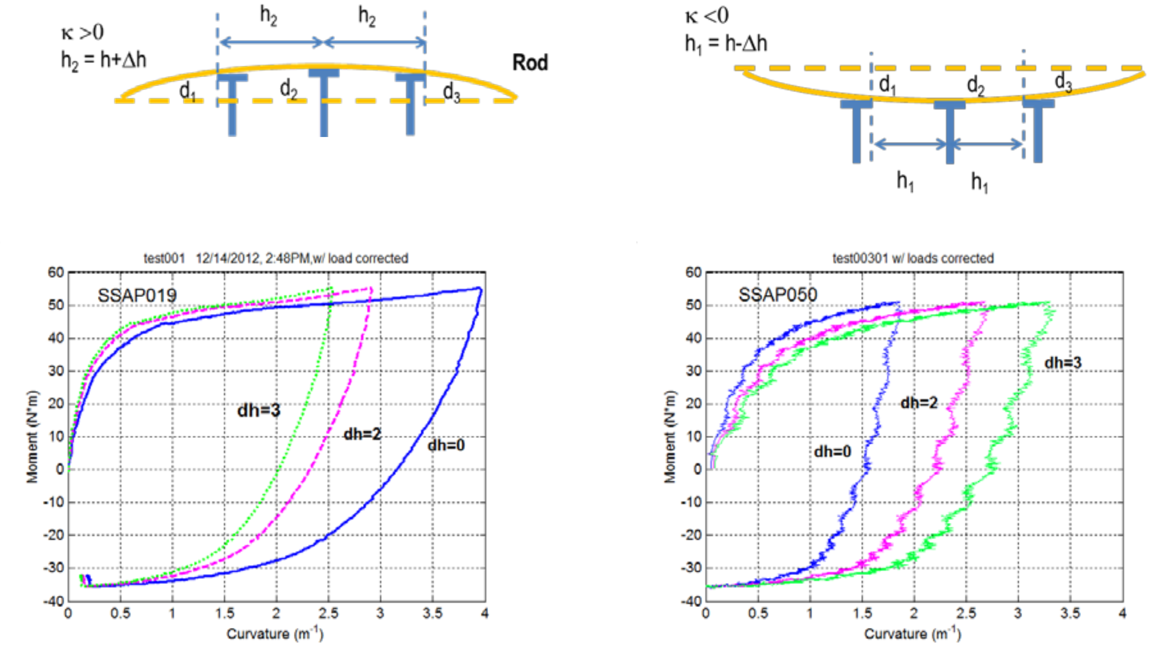

(a) (b)

Fig. 6. Moment-curvature curves as a function of sensor spacing adjustment when a rod is bending with respect to three LVDTs (a) concavely and (b) convexly.

3 CIRFT TESTING RESULTS OF H. B. ROBINSON USED FUEL

3.1 Dynamic Testing Results

Under DOE sponsorship, ORNL conducted the CIRFT tests on rod specimens R3, R4 and R5 and conducted limited PIE. Brief descriptions of these tests and the PIE are given below. For detailed information on the testing system, the data processing method, and test results on other rod specimens based on HBR UNF, refer to the NUREG/CR report [11] scheduled for publication in the fall of 2014.

3.1.1 D13/R3/606B3E under ±13.72 N·m 5 Hz

The cycle test on sample D13/R3 (606B3E, 66.5 gigawatt-days per megaton of uranium (GWd/MTU) burnup, 100–110 µm oxide layer, 750 ppm hydrogen content) was conducted under ±13.72 N·m at 5 Hz. Rod specimen R3 failed at approximately 1.29 × 10^5 cycles within the gauge section.

Online monitoring showed that rigidity increased prior to the final rigidity drop at failure as shown in Fig. 7. The peak and valley of curvature data reflect the decreased curvature range as seen by the drop in the peak value shown in Fig. 7d.

The possible causes of the single-side change in curvature waveform during the cyclic test are unknown, but decreased rigidity was seen in the measurement shown in Fig. 8.

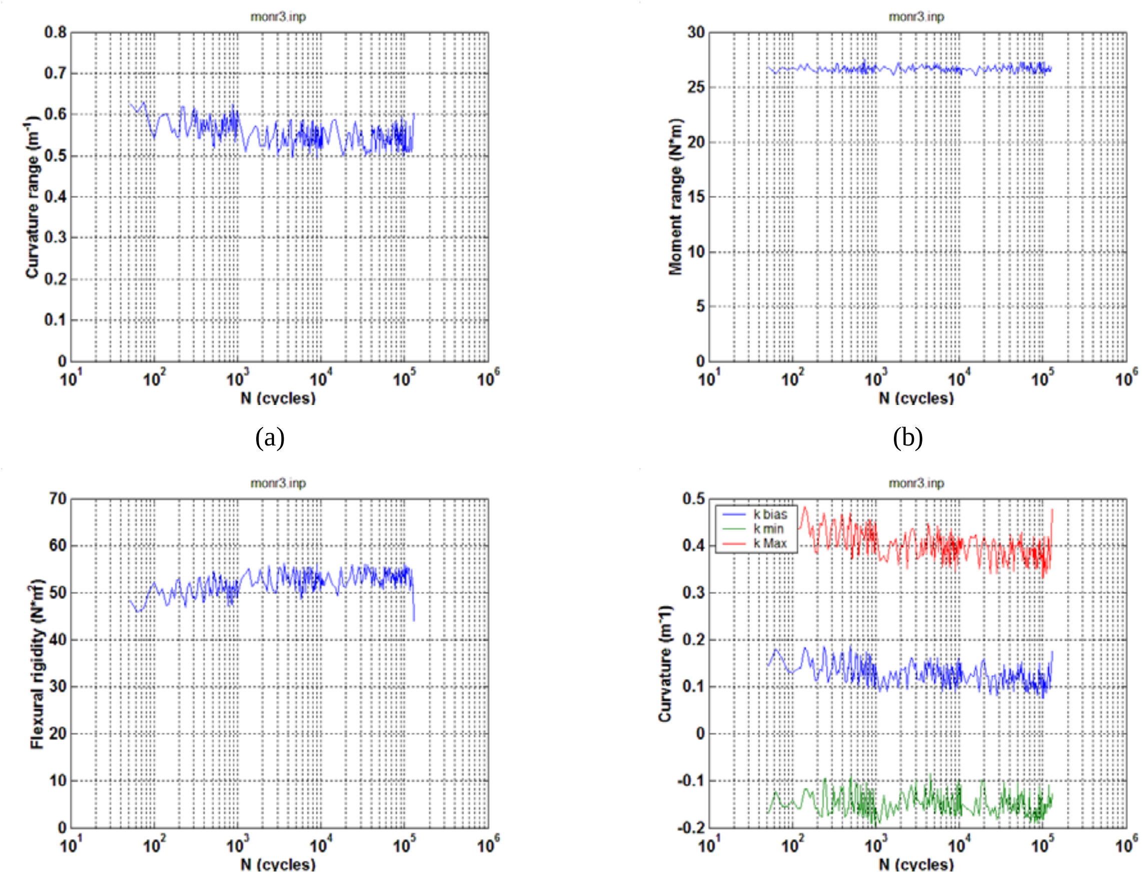

(a) (b)

(c) (d)

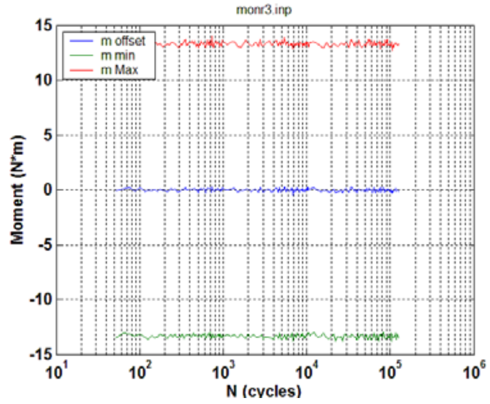

(e)

Fig. 7. Variations of (a) curvature range, (b) applied moment range, (c) flexural rigidity, (d) maximum and minimum values of curvature, and (e) maximum and minimum values of moment as a function of number of cycles for D13/R3 (606B3E); $N_f = 1.29 \times 10^5$ cycles under ±13.72 N·m 5 Hz.

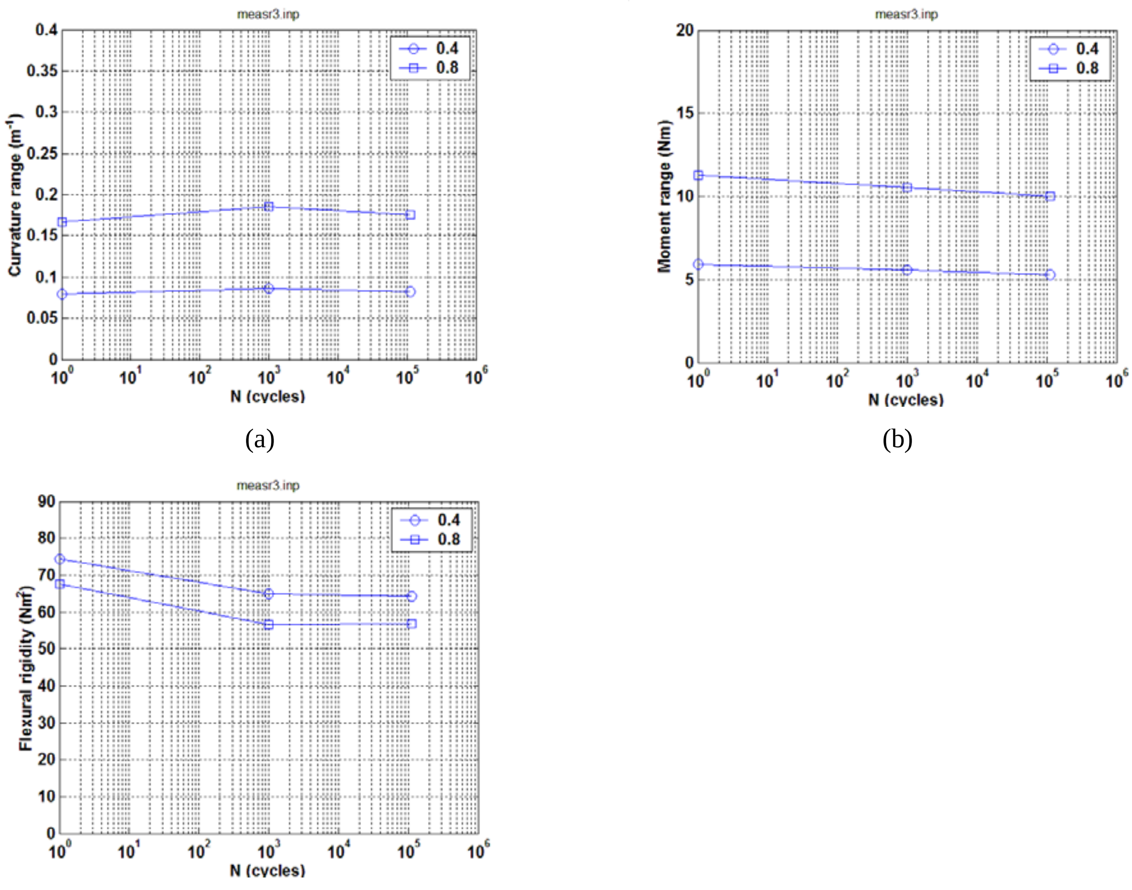

(a) (b)

(c)

Fig. 8. Variations of (a) curvature range, (b) applied moment range, and (c) flexural rigidity as a function of number of cycles for D13/R3 (606B3E); $N_f = 1.29\times10^5$ cycles under ±13.72 N·m 5 Hz.

3.1.2 D14/R4/606B3D under ±8.89 N·m 5 Hz

The cycle test on sample D14/R4 (606B3D, 66.5 GWd/MTU burnup, 100–110 μm oxide layer, 750 ppm hydrogen content) was conducted under ±8.89 N·m at 5 Hz. This test condition was the same as that of sample DM3. The test on rod specimen R4 was used to generate an additional observation with the same testing conditions as used on sample DM3. Rod specimen R4 exhibited a relatively short fatigue life with 2.7 × 10^5 cycles to failure. The short fatigue life may be due to a different preexisting specimen condition; it had a higher estimated hydrogen content. The hydrogen content of rod specimen R4 was approximately 750 ppm; the estimated hydrogen content of DM3 was approximately 550 ppm.

Online monitoring demonstrated a flat rigidity response with a slight rigidity drop prior to failure (Fig. 9). The measurement showed that rigidity increased slightly (Fig. 10).

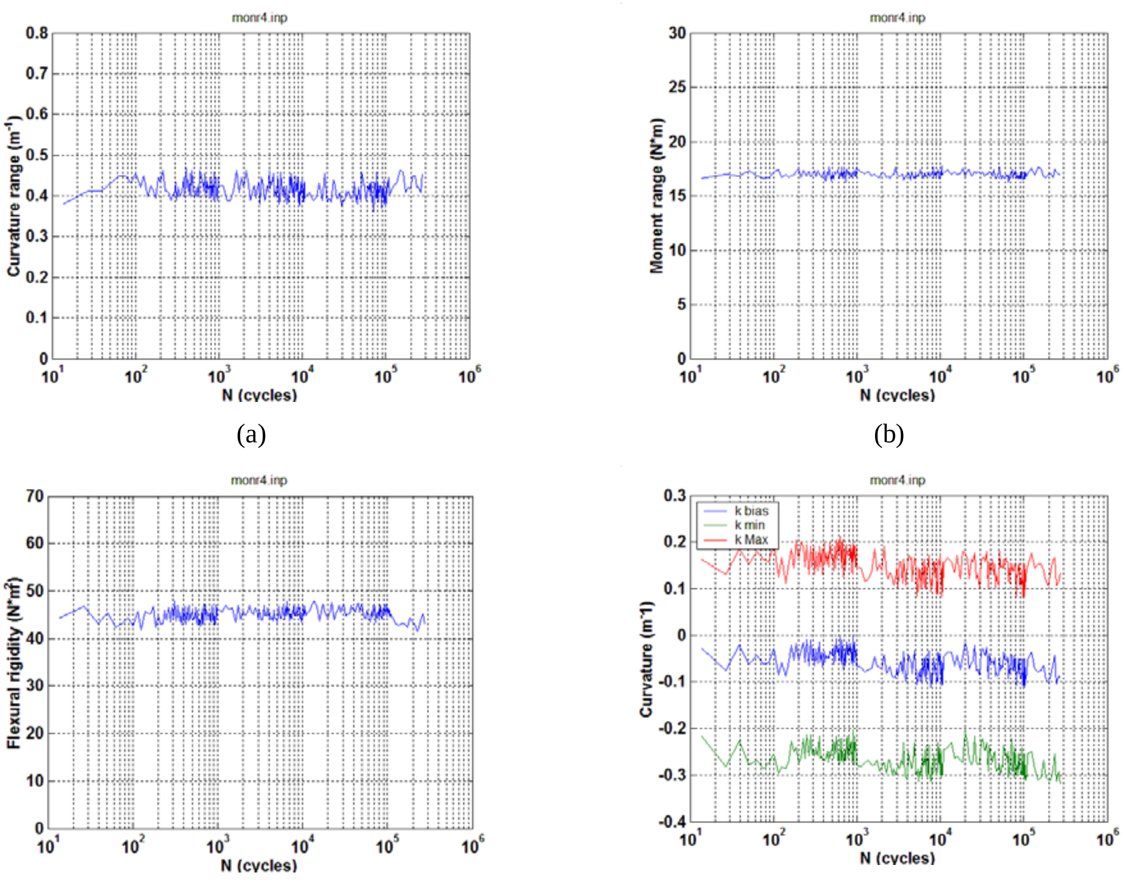

(a) (b)

(c) (d)

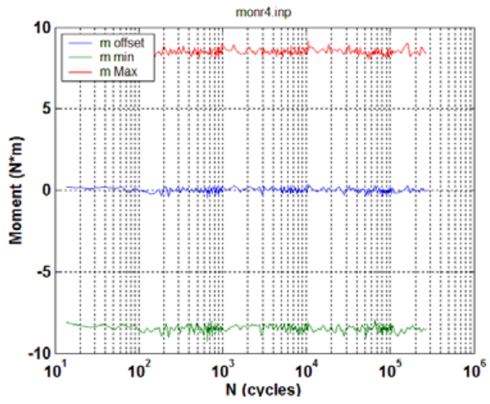

(e)

Fig. 9. Variations of (a) curvature range, (b) applied moment range, (c) flexural rigidity, (d) maximum and minimum values of curvature, and (e) maximum and minimum values of moment as a function of number of cycles for R4 (606B3D); $N_f = 2.7 \times 10^5$ cycles under ±8.89 N·m 5 Hz.

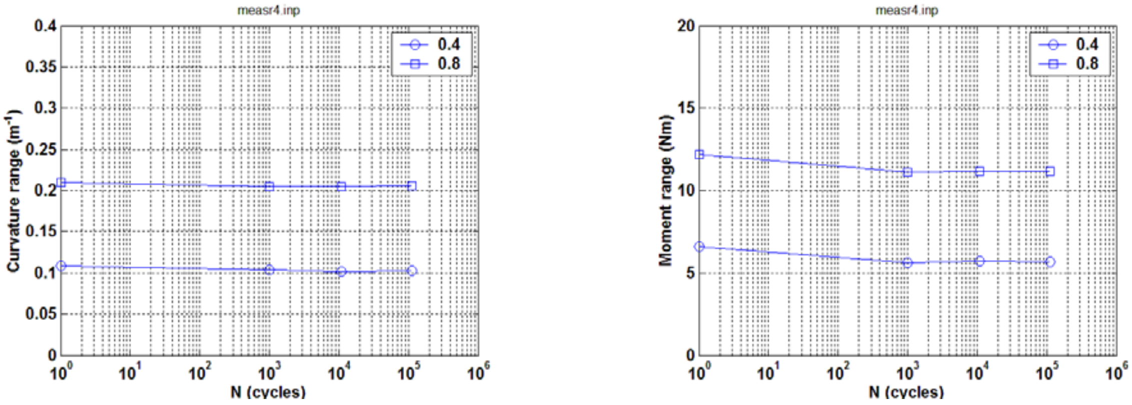

(a) (b)

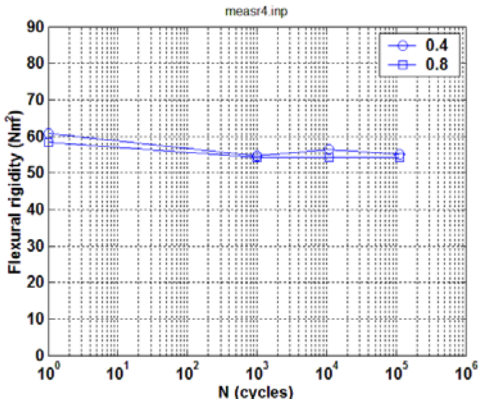

(c)

Fig. 10. Variations of (a) curvature range, (b) applied moment range, and (c) flexural rigidity as a function of number of cycles for R4 (606B3D); $N_f = 2.7 \times 10^5$ cycles under ±8.89 N·m 5 Hz.

3.1.3 D15/R5/606B3C under ±7.62 N·m 5 Hz

The cycle test on sample R5 (606B3C, 66.5 GWd/MTU burnup, 100–110 µm oxide layer, 750 ppm hydrogen content) was conducted under ±7.62 N·m 5 Hz. The moment range used for rod specimen R5 is the same as that used in DM1. The test on sample R5 provides the opportunity to examine the variation of fatigue response between different rods. The test on sample R5 was stopped after 2.23 × 10^7 cycles had been accumulated because no sign of failure could be seen.

Analysis based on the monitoring data indicated that the flexural rigidity was fairly stable and limited within a range of 40 to 50 Nm^2. A drop in flexural rigidity was observed after the rod was taken off and remounted to the testing machine. The reason is for this change is not clear; however, the rod appeared to be quite stable in the subsequent cycling process.

The online monitoring and measurement data are given in Fig. 11 and Fig. 12, respectively.

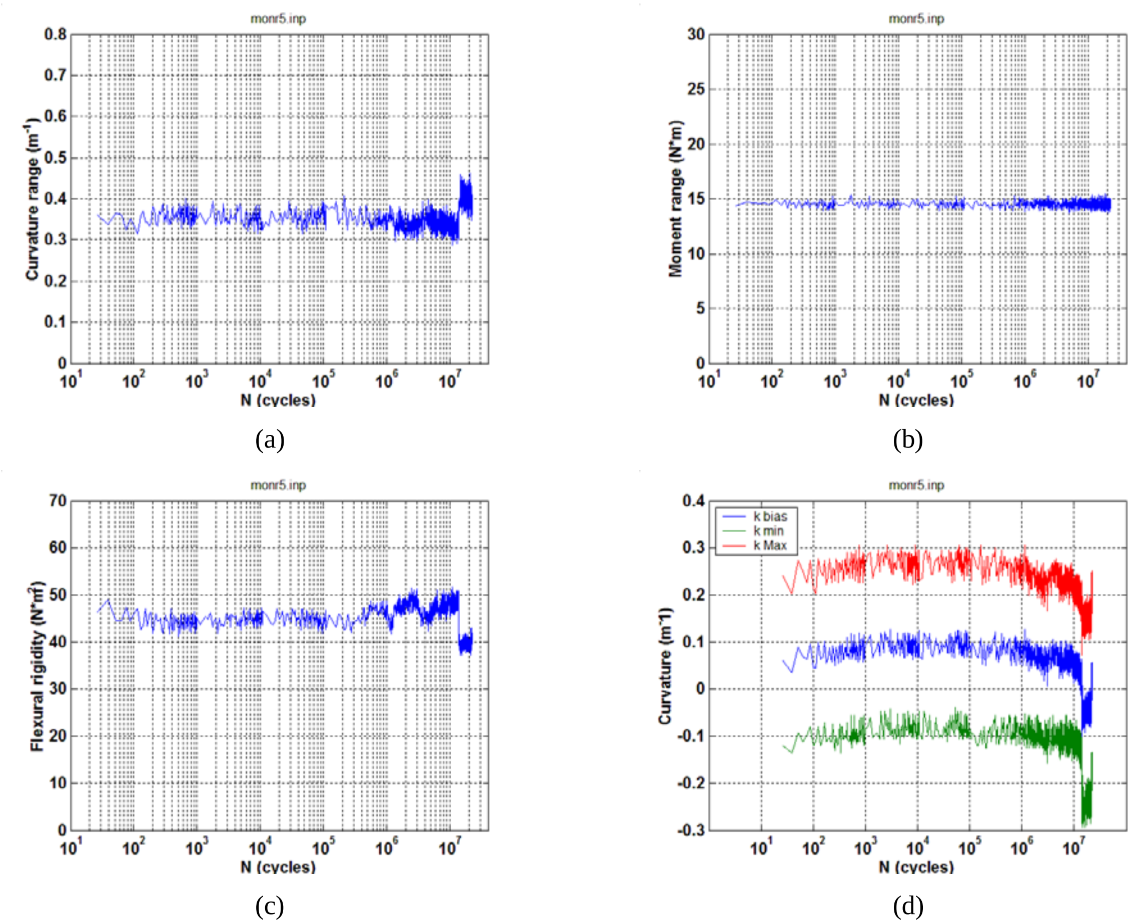

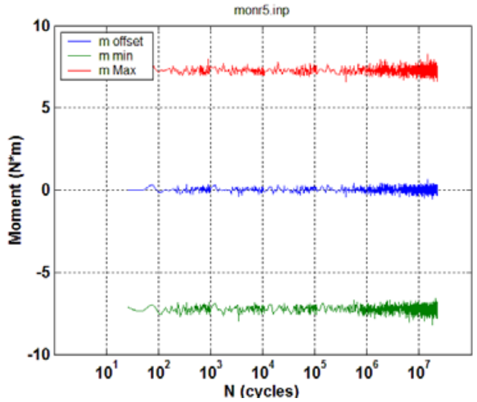

(e)

Fig. 11. Variations of (a) curvature range, (b) applied moment range, (c) flexural rigidity, (d) maximum and minimum values of curvature, and (e) maximum and minimum values of moment as a function of number of cycles for R5 (606B3C); N = 2.23 × 10^7 cycles under ±7.62 N·m 5 Hz.

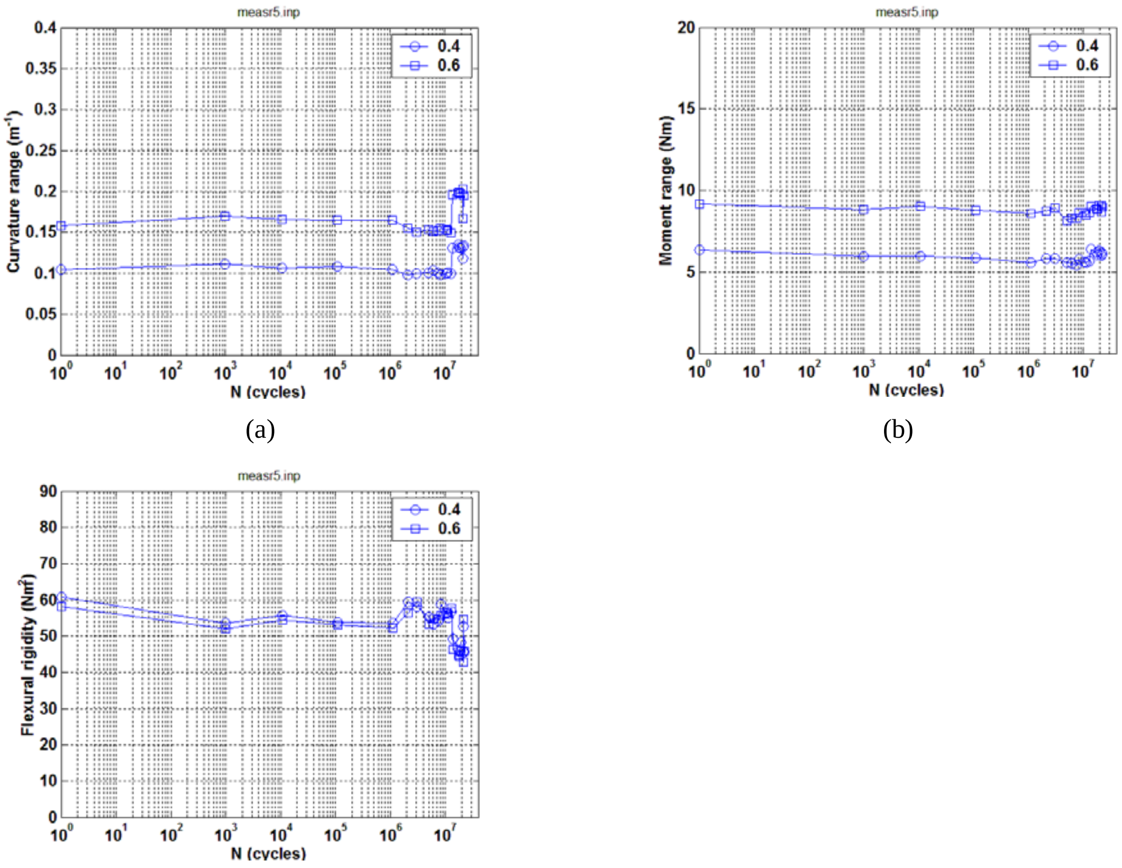

(a) (b)

(c)

Fig. 12. Variations of (a) curvature range, (b) applied moment range, and (c) flexural rigidity as a function of number of cycles for R5 (606B3C); N = 2.23 × 10^7 cycles under ±7.62 N·m 5 Hz.

3.2 Mean Curvature and Maximum of Absolute Curvature Extremes

Under a load-controlling mode, the offset of the M-κ loop with respect to the κ axis can be described by the mean value of curvatures, κ_m:

$$\kappa_m = 0.5 \times (\kappa_{max} + \kappa_{min}). \tag{5}$$

In load-controlled cycle tests, the curvature range $\Delta\kappa = (\kappa_{max} - \kappa_{min})$ exhibited a flat response prior to failure. As a result, the rigidity was stable over most of the monitored period, followed by a slight drop prior to failure. However, using curvature range/amplitude to characterize fatigue in UNF can be risky. This is because the response of rods is generally not symmetric with respect to the curvature origin, as seen in Sects. 3.1.1–3.1.3. The sign and magnitude of the mean curvature depends on the as-received condition of a rod and on loading conditions. These observations raised a concern because the use of curvature range/amplitude did not reflect the real maximum stress level of the outer fiber in a bending rod.

An alternate approach is based on the maximum of absolute curvature extremes, $|\kappa|_{max}$, as defined by the following:

$$|k|_{max} = \max(|k_{max}|, |k_{min}|). \tag{6}$$

For a given specimen, the $|\kappa|_{max}$ given by Eq. (5) corresponds to the curvature that causes the maximum stress levels.

Curvature as a function of the number of cycles is shown in Fig. 13 in terms of both curvature amplitude and maximum of absolute curvature extremes. The results indicate that the curve of curvature versus the number of cycles could be raised to a certain degree if the maxima were used instead of amplitude. The factor of the power function was increased by 23%.

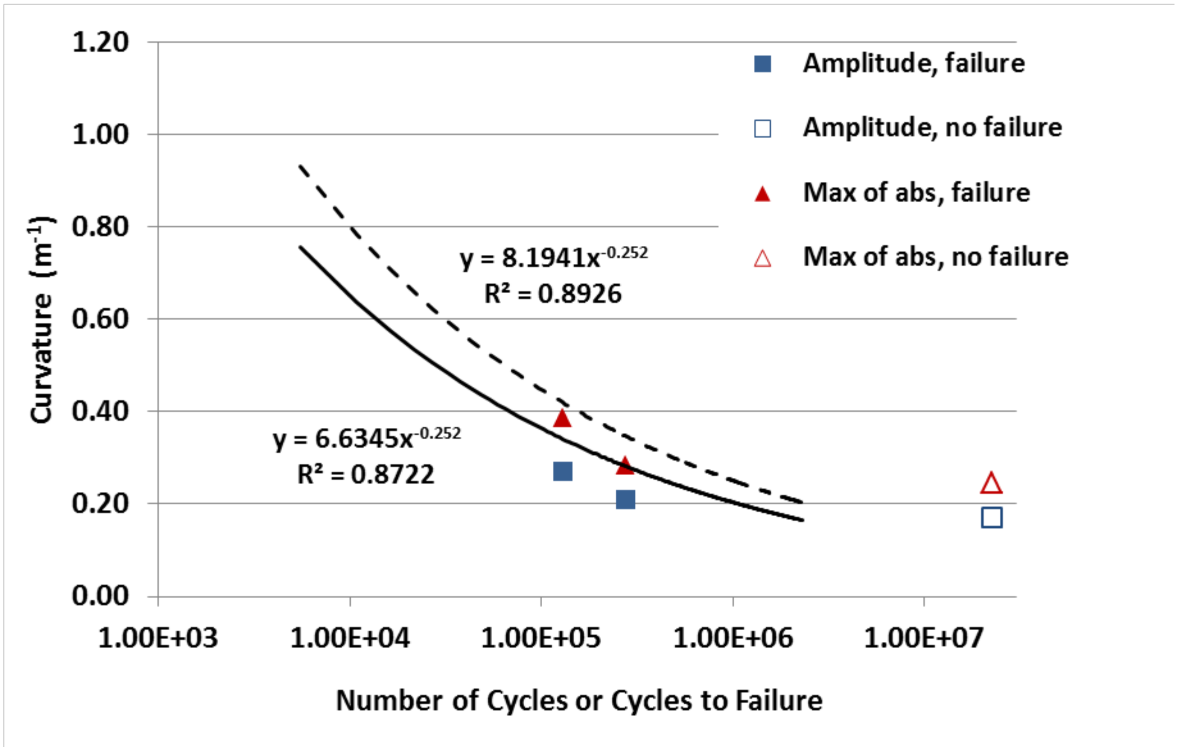

Fig. 13. Maxima of absolute (abs) curvature extremes and curvature amplitudes as a function of number of cycles. Solid markers represent tests with specimen failures; open markers indicate tests without failures. The power function was obtained from curve fitting based on the HBR data set [11]; solid line corresponds to amplitudes, and dash line corresponds to maxima of absolute.

3.3 κ-N Curve and Effect of Hydrogen Contents

There was no specific hydrogen content data available for the tested HBR rod segments. However, the ranges of hydrogen content on the parent fuel rods were available, and the hydrogen contents of the tested rod segments can be estimated based on where they were taken. The estimated hydrogen contents of the HBR rods ranged from 360 to 750 ppm. An assembly of cycle tests is presented in Fig. 14, with focus on the tests in which specimens failed. It can be clearly seen that the curve of curvature range vs. the number of cycles was shifted down and to the left when hydrogen content was equal to or greater than 700 ppm. Under the same curvature range, the fatigue life of the specimens with higher hydrogen content is shorter than the fatigue life of specimens with lower hydrogen content.

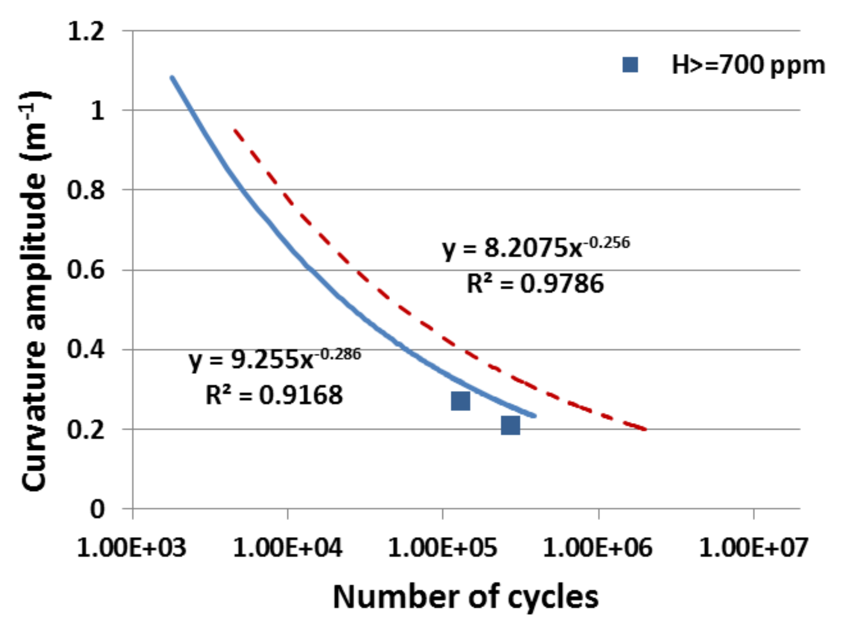

Fig. 14. Curvature amplitudes as a function of number of cycles or κ-N curve for HBR used fuel with various levels of hydrogen content. The power function was obtained from curve fitting based on the HBR data set; the solid line corresponds to H >= 700ppm, and the dashed line corresponds to H < 700pm [11].

4 CIRFT TESTING OF NORTH ANNA M5^{TM} AND MOX M5^{TM} UNF

4.1 Vise Mold

Both NA and MOX UNF have outside diameters of 9.450 to 9.683 mm; these are smaller than the diameter of HBR fuel (10.772 mm). The hole size of the vise mold must match the outside diameter of the fuel rod, or uncertainty will be introduced into the system by the relative position of the rod to the grips.

A surrogate rod was made of SS304 tube for use in calibrating the epoxy casting for NA M5$^{\mathrm{TM}}$ and MOX fuel. The trial resulted in an optimized amount (6.2 g) of fresh epoxy in the casting process. The second vise mold (illustrated in Fig. 15) was delivered to the ORNL hot-cell building in the reporting period.

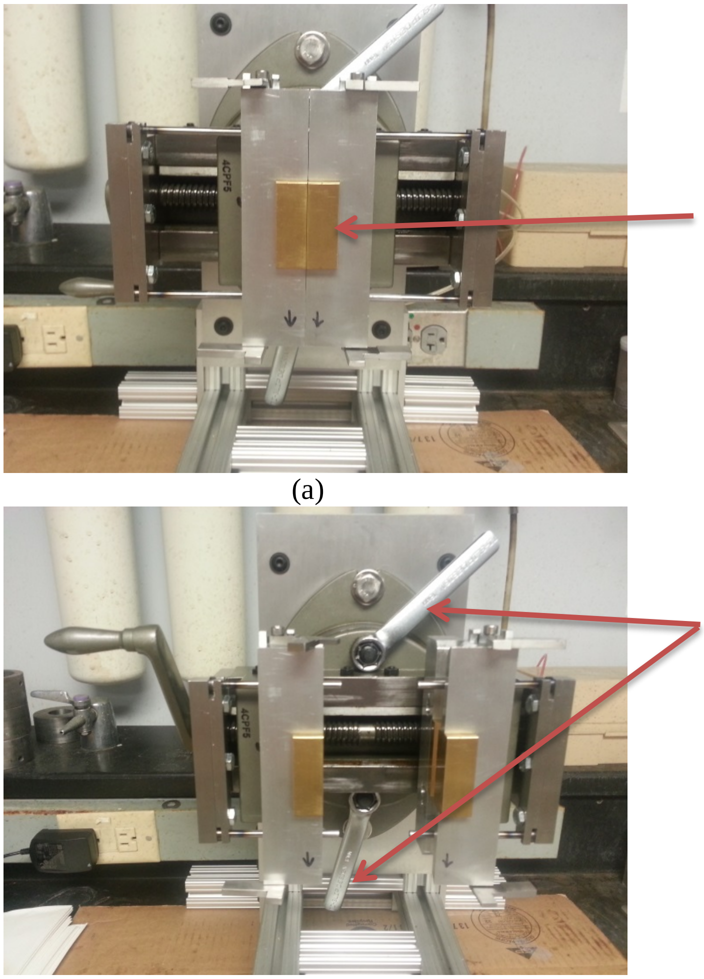

Inserts are provided for matching the outside diameter of NA and MOX fuels.

(a)

Handles are made for ease of use in a hot cell.

(b)

Fig. 15. The second fabricated vise mold is dedicated to preparing specimens of NA and MOX M5$^{\mathrm{TM}}$ fuels. The mold is closed in (a) and open in (b).

4.2 End Cap Preparation

Labels were applied on the end caps for NA and MOX UNF using laser engraving to ensure test sample identification. The label systems for NA and MOX fuel specimens are given in Table 1 and Table 2, respectively. The hot-cell-ready end caps for NA M5$^{\mathrm{TM}}$ UNF are shown in Fig. 16.

Table 1. Specimen labels used for NA M5^{TM} UNF

Fuel segment ID	CIRFT label	End-cap A	End-cap B
651B2	NA1	NA-1A	NA-1B
651C5	NA2	NA-2A	NA-2B
651D3	NA3	NA-3A	NA-3B
652B1B	NA4	NA-4A	NA-4B
652B2	NA5	NA-5A	NA-5B
652D1	NA6	NA-6A	NA-6B
652D2	NA7	NA-7A	NA-7B

Table 2. Specimen labels used for MOX UNF

Segment ID	CIRFT label	End-cap A	End-cap B
MOX-A-11	MOX1	MOX-1A	MOX-1B
MOX-A-12	MOX2	MOX-2A	MOX-2B
MOX-A-13	MOX3	MOX-3A	MOX-3B
MOX-B-05	MOX4	MOX-4A	MOX-4B
MOX-B-06	MOX5	MOX-5A	MOX-5B
MOX-B-07	MOX6	MOX-6A	MOX-6B
MOX-C-06	MOX7	MOX-7A	MOX-7B
MOX-C-07	MOX8	MOX-8A	MOX-8B
MOX-C-08	MOX9	MOX-9A	MOX-9B
MOX-K-09	MOX10	MOX-10A	MOX-10B
MOX-K-10	MOX11	MOX-11A	MOX-11B
MOX-K-11	MOX12	MOX-12A	MOX-12B
	MOX13	MOX-13A	MOX-13B
	MOX14	MOX-14A	MOX-14B
	MOX15	MOX-15A	MOX-15B

Fig. 16. NA end-caps after laser engraving and spot welding.

4.3 Metrology of NA M5^{TM} UNF

An inventory was made of the NA M5^{TM} UNF, and the outside diameters of the fuel segments were measured. The results are given in Table 3 [12-13].

Table 3. Outside diameters of NA M5^{TM} UNF segments (in.)* [3]

Fuel Segment	A			B			Mean
	1	2	3	1	2	3	
651B2	0.37942	0.37872	0.37732	0.37998	0.37918	0.37798	0.3788
651C5	0.37710	0.37660	0.37632	0.37774	0.37720	0.37682	0.3770
651D3	0.38032	0.37934	0.38020	0.38198	0.38220	0.38300	0.3812
652B1B	0.37964	0.37890	0.37767	0.37954	0.37860	0.37784	0.3787
652B2	0.38012	0.37990	0.37924	0.37860	0.37796	0.37714	0.3788
652D1	0.37966	0.37894	0.37802	0.37904	0.37888	0.37760	0.3787
652D2	0.37998	0.38008	0.38020	0.37924	0.37994	0.38022	0.3799

* The measurements were made at the top (A, 0^o) and the side (B, 90^o) at three locations (1, 2, 3) in the middle of the rod segment. These measurement points were 0.5 inches apart.

4.4 Tuning of Testing Machine

The testing machine was tuned with specimen MOX1 under displacement control, ±1.5 mm, 5 Hz. The tuning parameters are listed in Table 4.

Table 4. Tuning parameters for MOX1

Axial 1		Axial 2	
TuneIQ1	2.0645	TuneIQ1	1.5448
TuneIQ2	0.0158	TuneIQ2	0.0122
TuneIQ3	-11.8255	TuneIQ3	-9.7299

4.5 Static Testing of North Anna M5^{TM} UNF

The in-cell rod specimen preparation demonstrated that the second vise mold works as designed. The amount of fresh epoxy was adjusted to 6.4 g after the first trial.

4.5.1 NA3/651D3

The first static test was conducted on the specimen with the CIRFT label NA3 (fuel segment 651D3) under a displacement control mode using the following test procedure:

1. Ramp up to 12.00 mm at 0.1 mm/s rate at each loading point or each Bose motor.
2. Return to 0.0 mm at 0.2 mm/s.
3. If the rod specimen does not fail, repeat steps 1 and 2 four times.

Specimen NA3 survived four loading cycles without any sign of failure. The moment-curvature curves and equivalent stress-strain curves are shown in Fig. 17. In the estimates of equivalent stress and strain, the inside and outside diameters of 8.293 and 9.683 mm were used, respectively. There was a significant nonlinear deformation after 30 N·m; the maximum moment of 47 N·m was attained during the initial loading cycle. A deflection point appeared at approximately 8 N·m in the initial loading cycle. Subsequent loading cycles did not produce additional deformation, but they did introduce a closed hysteresis loop. The maximum curvature under a relative displacement of 24.00 mm at the loading points of the U-frame (i.e., 12.00 mm at each motor) was 4.1 m^{-1}. The maximum equivalent stress and strain obtained were 522 MPa and 2%, respectively. The rod appeared to be bent with significant plastic deformation after the static tests as shown in Fig. 18.

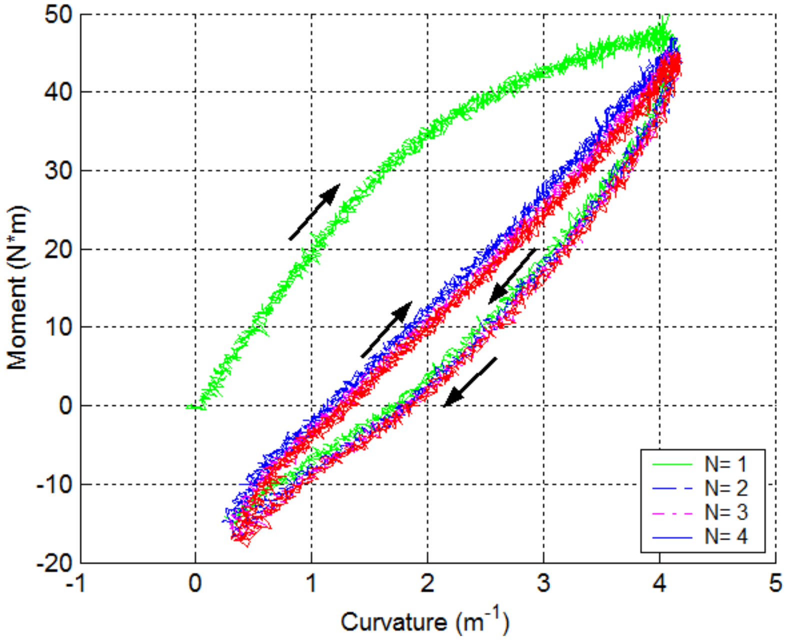

(a)

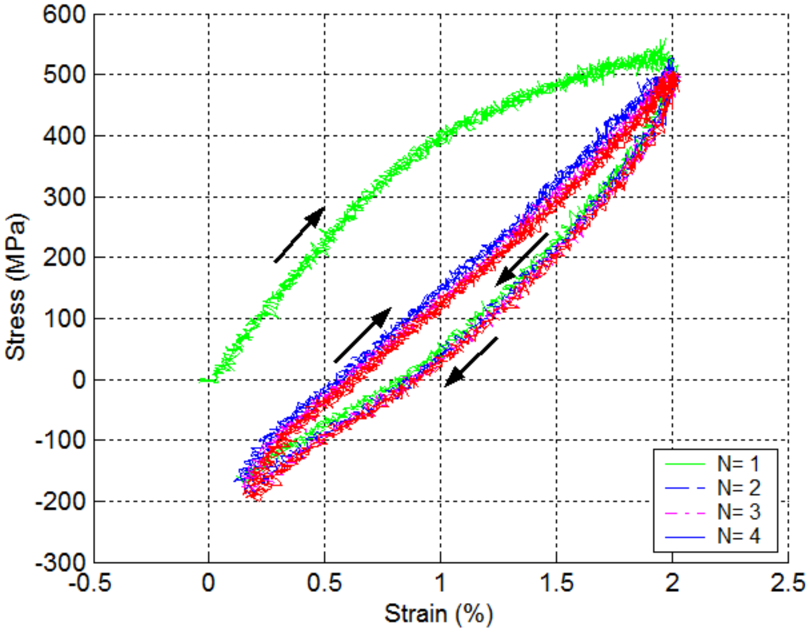

(b)

Fig. 17. (a) Moment-curvature curves and (b) equivalent stress-strain curves based on the first four loading cycles for specimen NA3 (651D3).

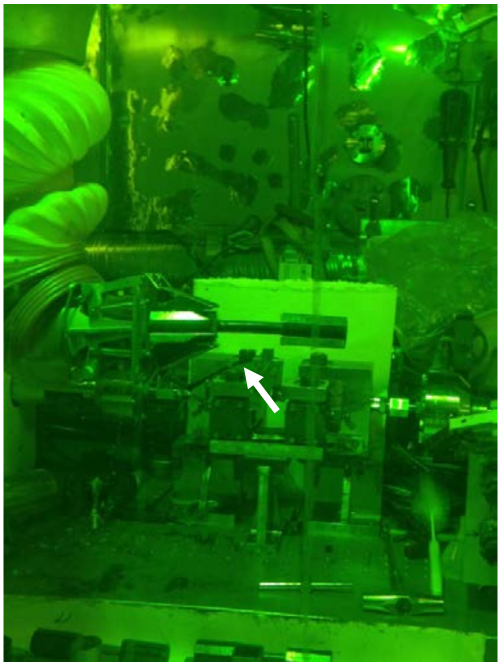

Fig. 18. Image of specimen NA3 (651D3) after testing; the rod sustained four cycles of loading to 24.00-mm relative displacement; the maximum moment with a level of 47 N·m was reached during the initial loading cycle.

4.6 Static Testing of MOX UNF

4.6.1 MOX1/ MOX-A-11

The first static test was conducted on MOX1 UNF (specimen MOX-A-11) under a displacement control mode using the following test procedure:

1. Ramp up to 12.00 mm at 0.1 mm/s rate at each loading point or each Bose motor.
2. Return to 0.0 mm at 0.2 mm/s.
3. If the rod specimen does not fail, repeat steps 1 and 2 four times.

No hot-cell measurement data are available on the MOX UNF segment. The inside and outside diameters of the NA fuel rod segment (8.293 and 9.683 mm, respectively) are used as a reference in the analysis below. The MOX1 specimen survived two loading cycles without any sign of failure. The moment-curvature curves and equivalent stress-strain curves are shown in Fig. 19. There was a significant nonlinear deformation after 30 N·m; the maximum moment of 47 N·m was reached during the initial loading cycle. A deflection point appeared at approximately 8 N·m in the initial loading cycle. Subsequent loading cycles did not produce additional deformation, but loadings generated a closed hysteresis loop. The maximum curvature under a relative displacement of 24.00 mm at the loading points of the U-frame (i.e., 12.00 mm at each motor) was 3.85 m^{-1}. The maximum equivalent stress and strain were 520 MPa and 1.8%, respectively.

A dynamic test was carried out under ±15.24 N·m, 5 Hz to observe the failure mode of the rod. The fatigue life of the rod $N_f = 4.0 \times 10^3$ cycles. The rod finally failed in the gauge section as shown in Fig. 20.

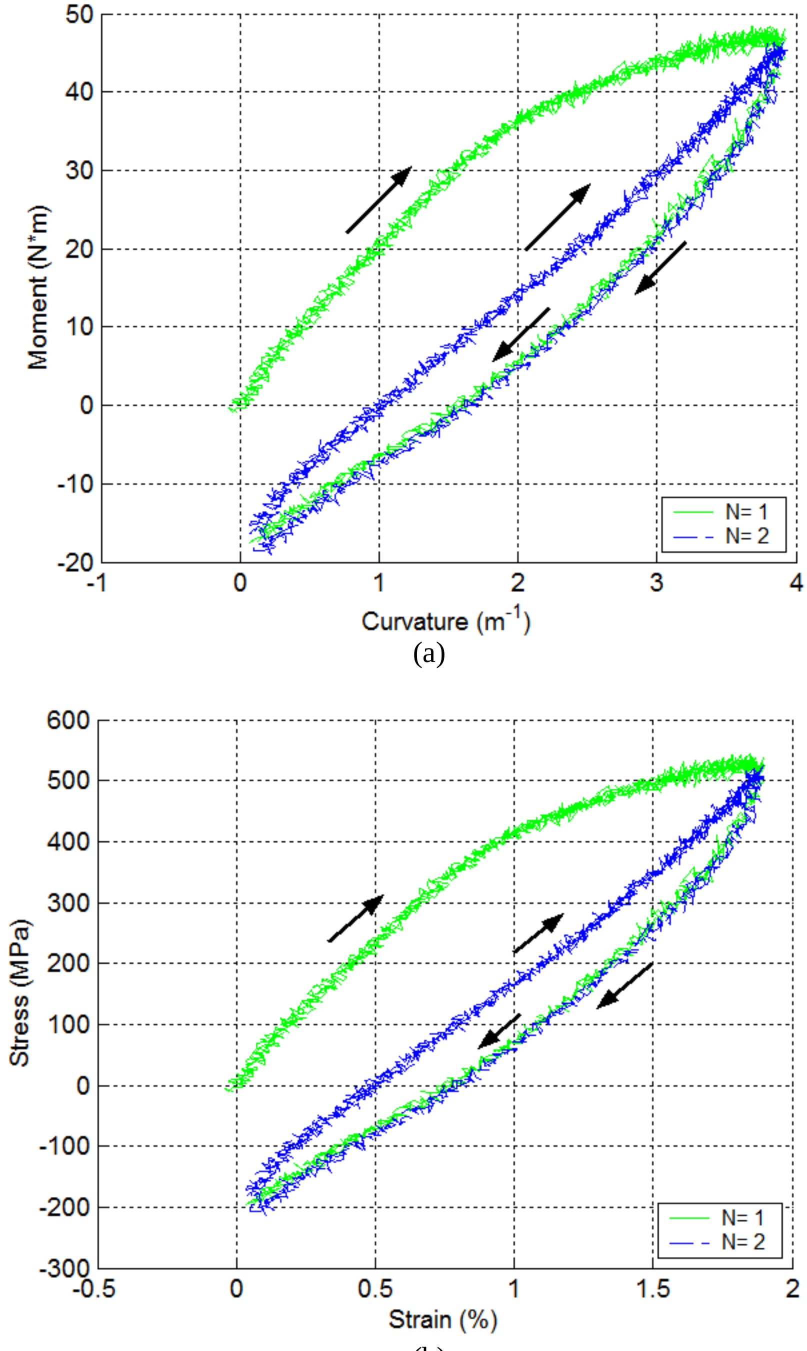

(a)

(b)

Fig. 19. (a) Moment-curvature curves and (b) equivalent stress-strain curves based on the first four loading cycles for MOX1 (specimen MOX-A-11).

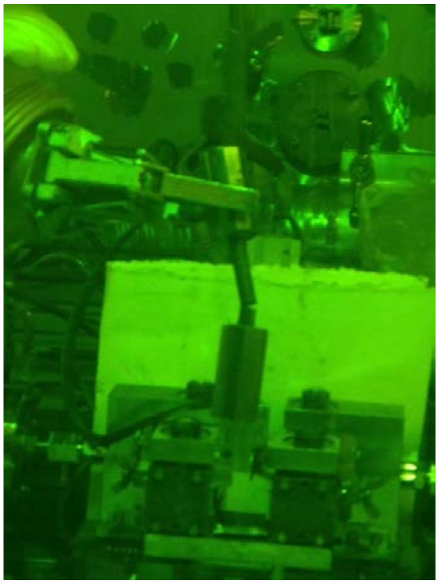

Fig. 20. Fracture segments for MOX1 (specimen MOX-A-11); the rod survived two cycles of loading to relative displacement 24.00 mm with the maximum moment of 47 N·m in the initial cycle. A follow-up dynamic test was carried out under ±15.24 N·m, 5 Hz; $N_f = 4.0 \times 10^3$ cycles.

4.6.2 MOX3/ MOX-A-13

The MOX3 (specimen MOX-A-13) was tested using the same procedure as that of MOX1, but only the first two steps were executed.

The moment-curvature curves and equivalent stress-strain curves are shown in Fig. 21. The second stage as seen in MOX1 and other HBR fuel specimens is hard to identify because the moment-curvature curve turned out to be nonlinear starting at approximately 9 N·m. The maximum moment was 45 N·m. The maximum curvature under a relative displacement of 24.00 mm at the loading points of the U-frame (i.e., 12.00 mm at each motor) was 3.53 m^{-1}. The maximum equivalent stress and strain were 510 MPa and 1.7%, respectively.

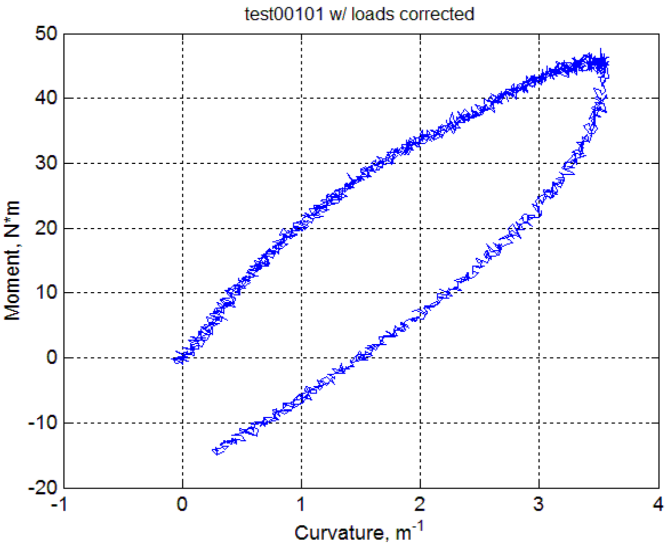

(a)

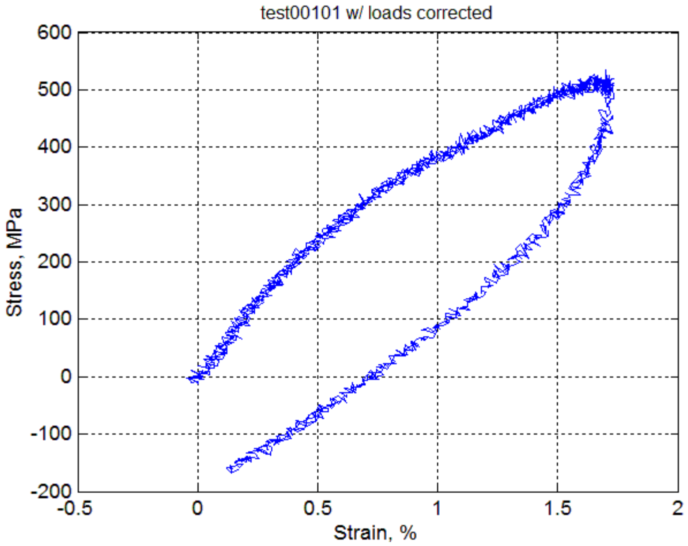

(b)

Fig. 21. (a). Moment-curvature curves and (b) equivalent stress-strain curves based on the first four loading cycles for MOX3 (MOX-A-13).

4.7 Dynamic Testing of North Anna M5^{TM} UNF

Three dynamic tests were conducted in the hot cell. Applied moment amplitudes varied from ±7.62 to ±12.70 N·m. The fatigue life ranged from 1.57×10^4 to 6.1×10^4 cycles. The results are described briefly in this section.

4.7.1 NA1/651C5 under 12.70 N·m 5Hz

The test on specimen NA1/651C5/ was conducted under ±12.70 N·m, 5 Hz. A fatigue life of 1.57×10^4 cycles was obtained. Periodic quasistatic measurements of rod deformation were conducted using three relative displacement levels—1.0, 2.0, and 3.0 mm—at the selected target number of cycles as described in Wang and Wang [11]. Time history of moment and curvature and curvature-moment loops obtained at the first cycle and 11,000 cycles are shown in Fig. 22. The curvature-moment loops are quite twisted, without the regular elliptical shape seen before in HBR rods [11]. The twisted loops may have been associated with the lowered sampling rate used in the curvature measurement. Nevertheless, the curvature ranges were still captured.

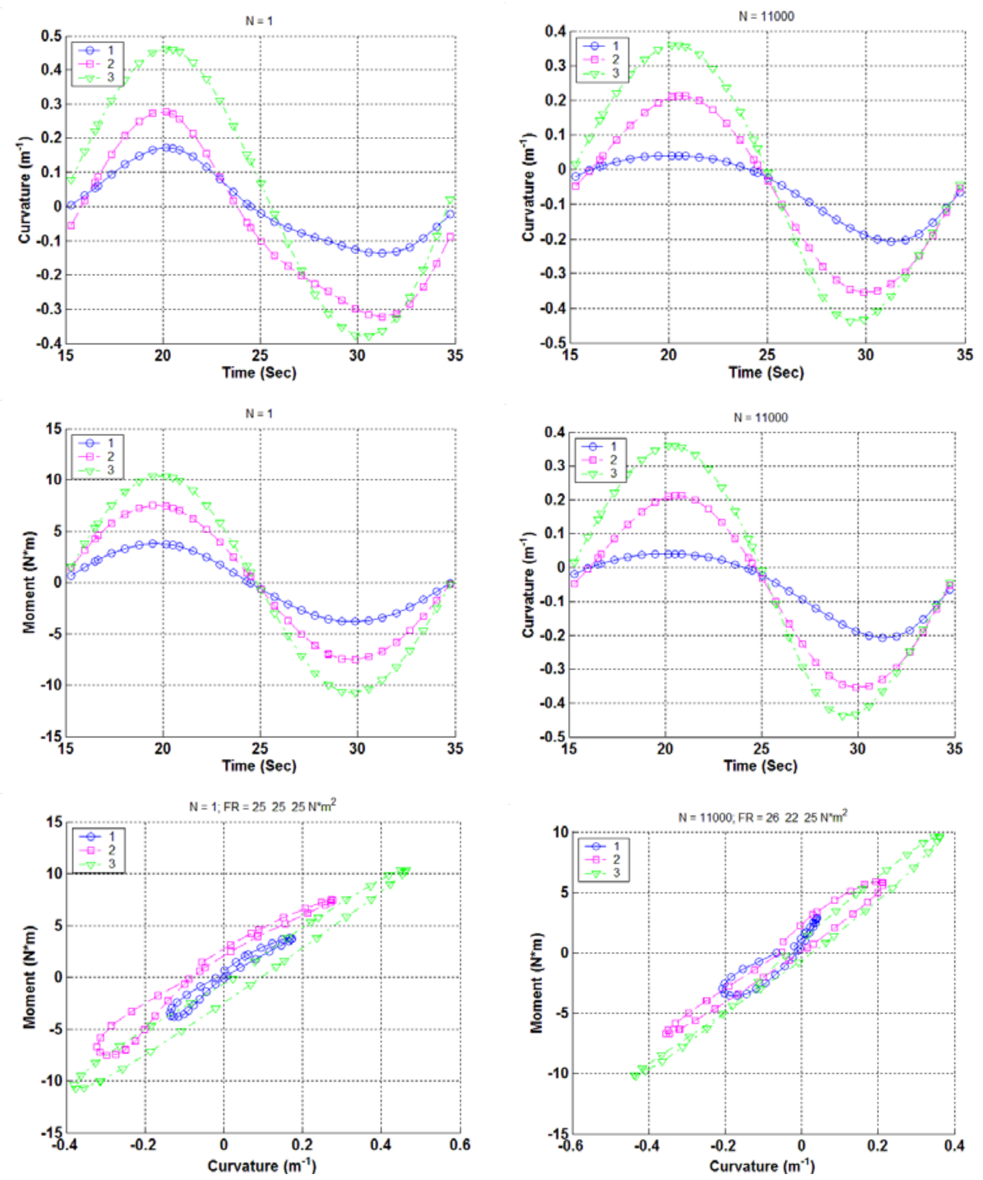

(a) (b)

Fig. 22. Moment and curvature as a function of time and moment-curvature loops based on measurements when (a) N=1 and (b) N = 111,000 cycles for NA1 (651B2). Measurements were made with 1.0, 2.0, and 3.0 mm relative displacements; $N_f = 1.57\times10^4$ cycles under ±12.70 N·m, 5 Hz.

The curvature range-moment range and flexural rigidity are illustrated in Fig. 23. The variations of these quantities as a function of the number of cycles are given in Fig. 24. The rigidity of the measurements at three displacements started with 25 Nm^2 and then dropped. The curvature, moment, and flexural rigidity based on online monitoring data are presented in Fig. 25. Online monitoring showed a flexural rigidity of about 24 Nm^2, a little lower than the value observed in measurements. This discrepancy is because different loading conditions were used in measurement and cycling. Overall, a quite stable rod response was exhibited before the final failure. Moment and curvature time history and moment-curvature loops based on online monitoring at early and late stages of dynamic testing are shown in Fig. 26. The moment-curvature loops based on online monitoring were well defined. Except for a little drifting toward the left, no significant change can be observed between loops measured in two points of the cycle process. The failure was observed in the gauge section, as seen in Fig. 27. The fracture surface is not quite clearly visible at this level of resolution.

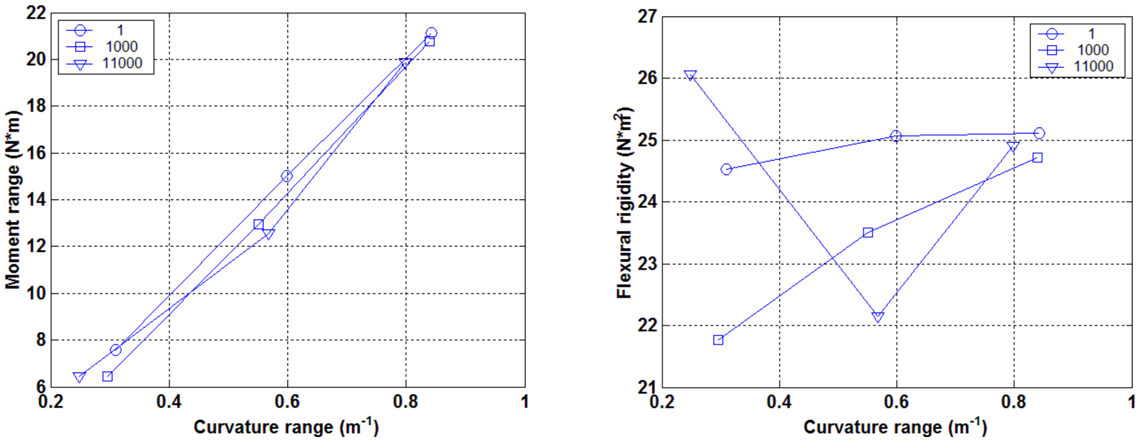

(a) (b)

Fig. 23. (a) Moment-curvature relation and (b) moment-flexural rigidity relation at various numbers of cycles for NA1 (651B2). Measurements were made with 1.0, 2.0, and 3.0 mm relative displacements; Nf = 1.57 × 104 cycles under ±12.70 N·m, 5 Hz.

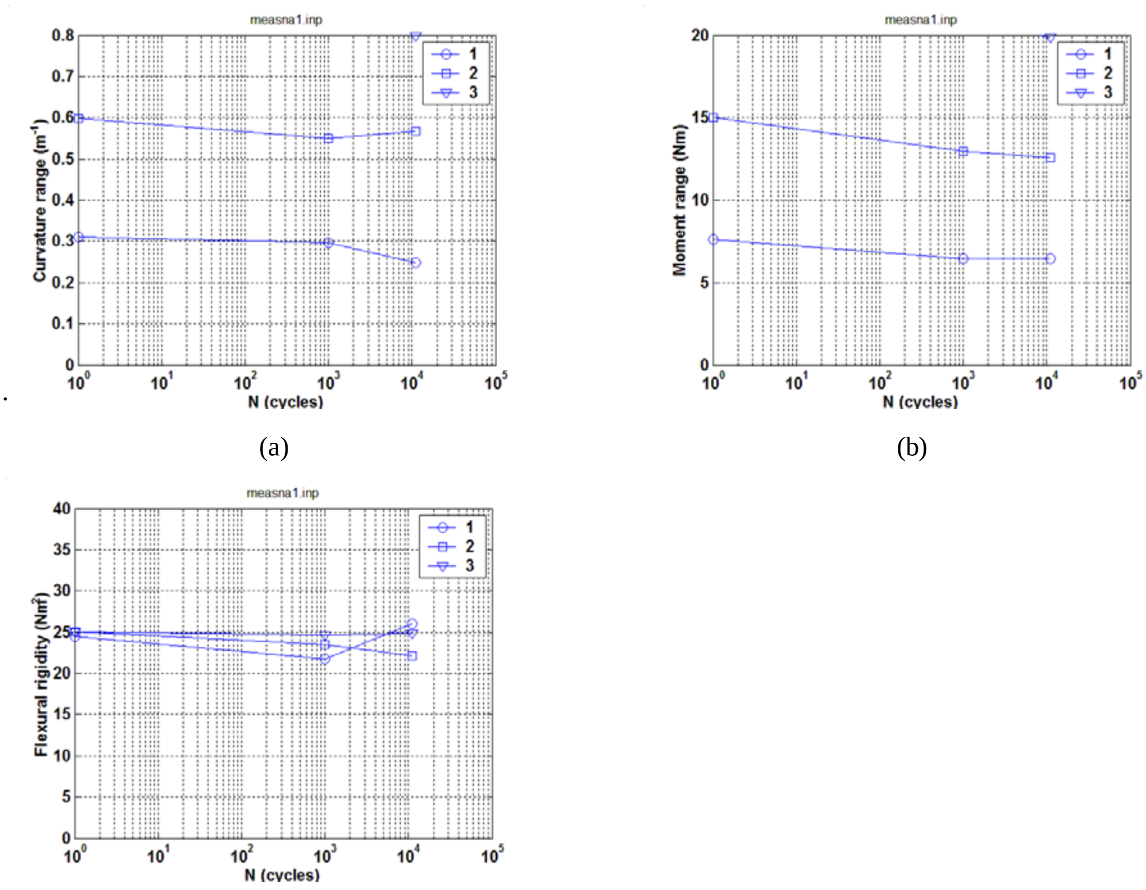

(a)

(b)

(c)

Fig. 24. Variations of (a) curvature range, (b) moment range, and (c) flexural rigidity as a function of number of cycles for NA1 (651B2). Measurements were made with 1.0, 2.0, and 3.0 mm relative displacements; $N_f = 1.57 \times 10^4$ cycles under ±12.70 N·m, 5 Hz.

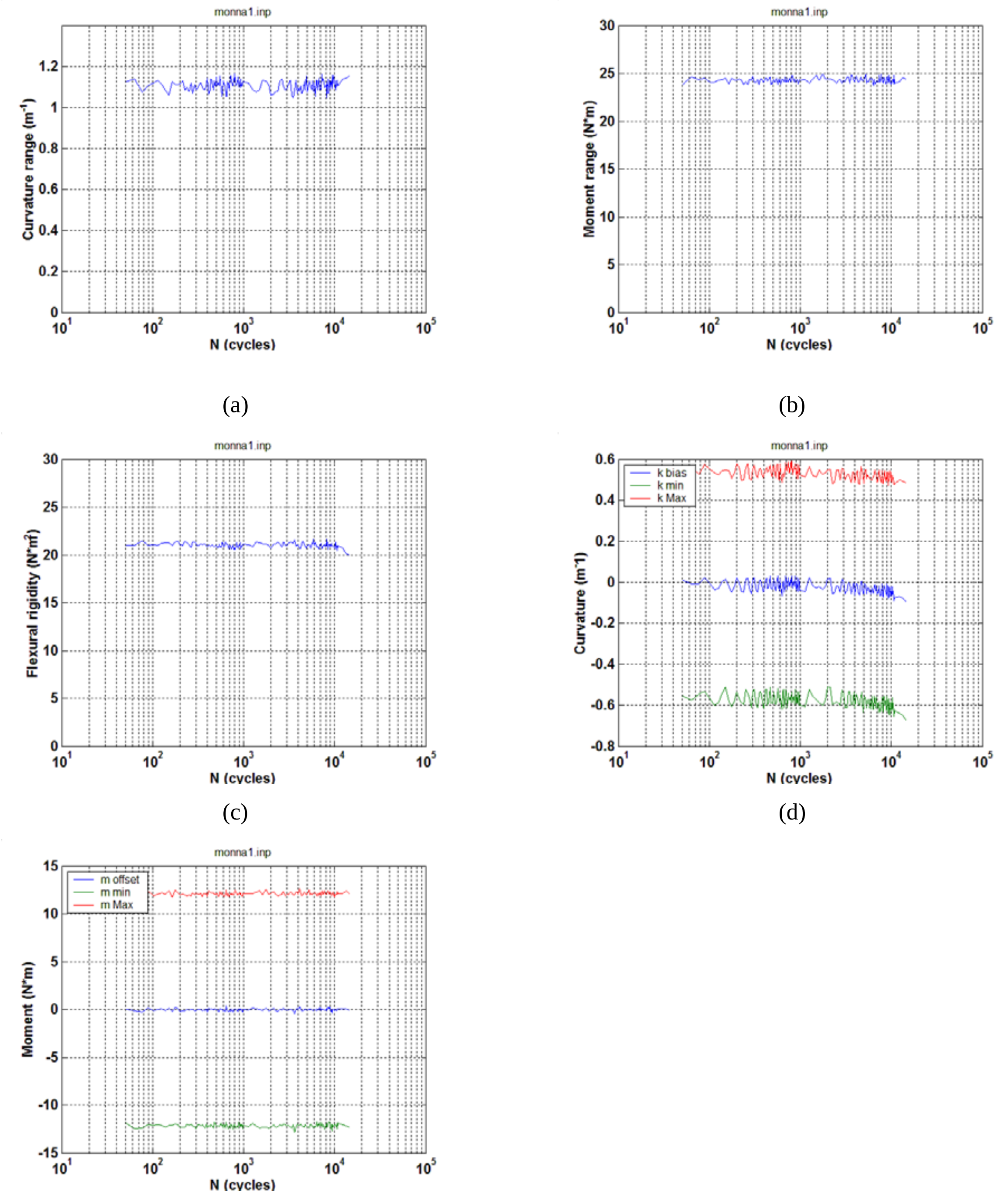

(a) (b) (c) (d) (e)

Fig. 25. Variations of (a) curvature range, (b) applied moment range, (c) flexural rigidity, (d) maximum and minimum values of curvature, and (e) maximum and minimum values of moment as a function of number of cycles for NA1 (651B2); $N_f = 1.57 \times 10^4$ cycles under ±12.70 N·m, 5 Hz.

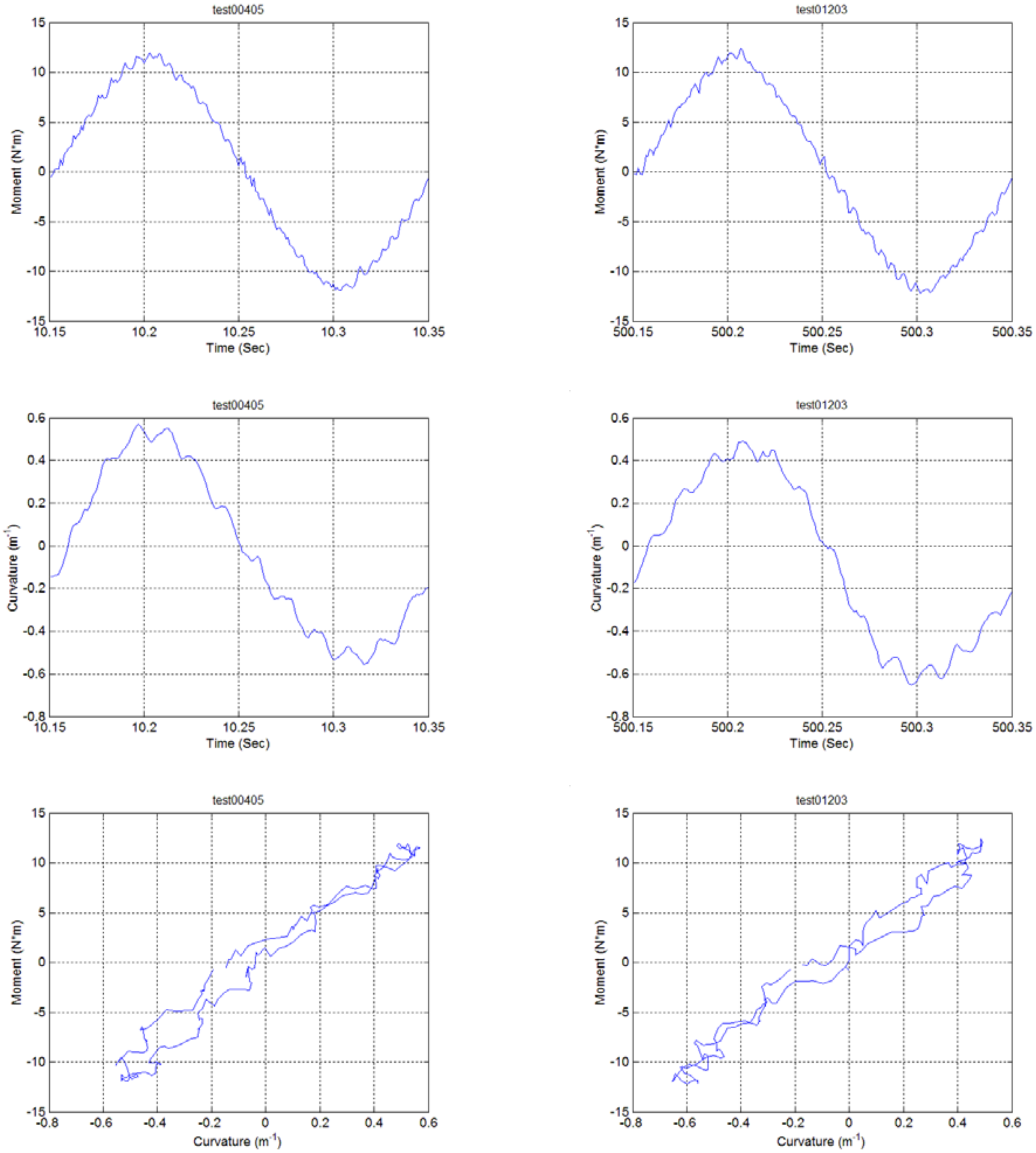

(a)

(b)

Fig. 26. Moment and curvature as a function of time and moment-curvature loops at (a) 50 cycles and (b) 1.35 × 10^4 cycles; results are based on online monitoring of NA1 (651B2).

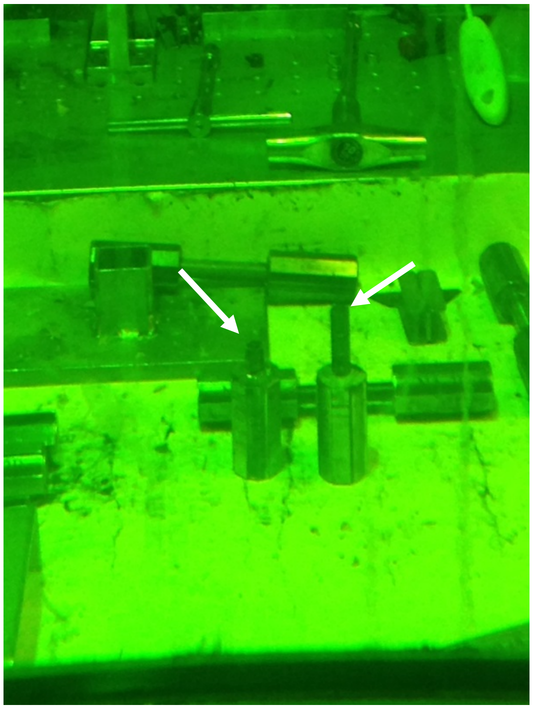

Fig. 27. Fracture segments for NA1 (651B2); $N_f = 1.57 \times 10^4$ cycles under ±12.70 N·m, 5 Hz.

4.7.2 NA2/651C5 under 10.16 N·m 5Hz

The test on NA2 (651C5) was conducted under ±10.16 N·m, 5 Hz. A fatigue life of 2.2×10^4 cycles was obtained.

Periodic quasistatic measurements of rod deformation were conducted using two relative displacement levels—1.0 and 2.0 mm—at the target intervals as described in Wang and Wang [11]. Variations of the curvature, moment, and flexural rigidity as a function of number of cycles are given in Fig. 28. The flexural rigidity of the rod stayed between 22 and 25 Nm^2 during most of the cycle testing period. This value of rigidity is a little lower than but still close to that of NA2. The results from online monitoring are given in Fig. 29, and the image showing the failure location of the rod specimen is given in Fig. 30.

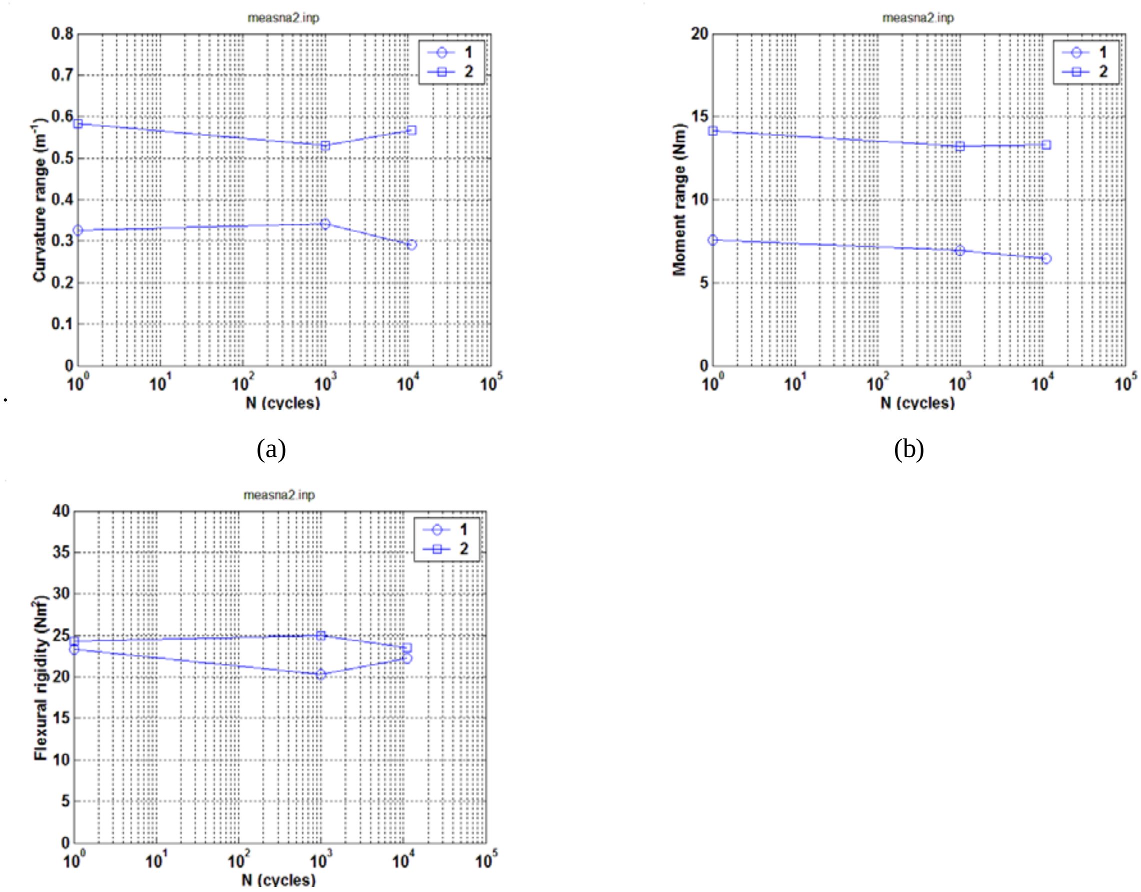

(a) (b)

(c)

Fig. 28. Variations of (a) curvature range, (b) moment range, and (c) flexural rigidity as a function of number of cycles for NA2 (651C5). Measurements were made with 1.0 and 2.0 mm relative displacements; $N_f = 2.2 \times 10^4$ cycles under ±10.16 N·m, 5 Hz.

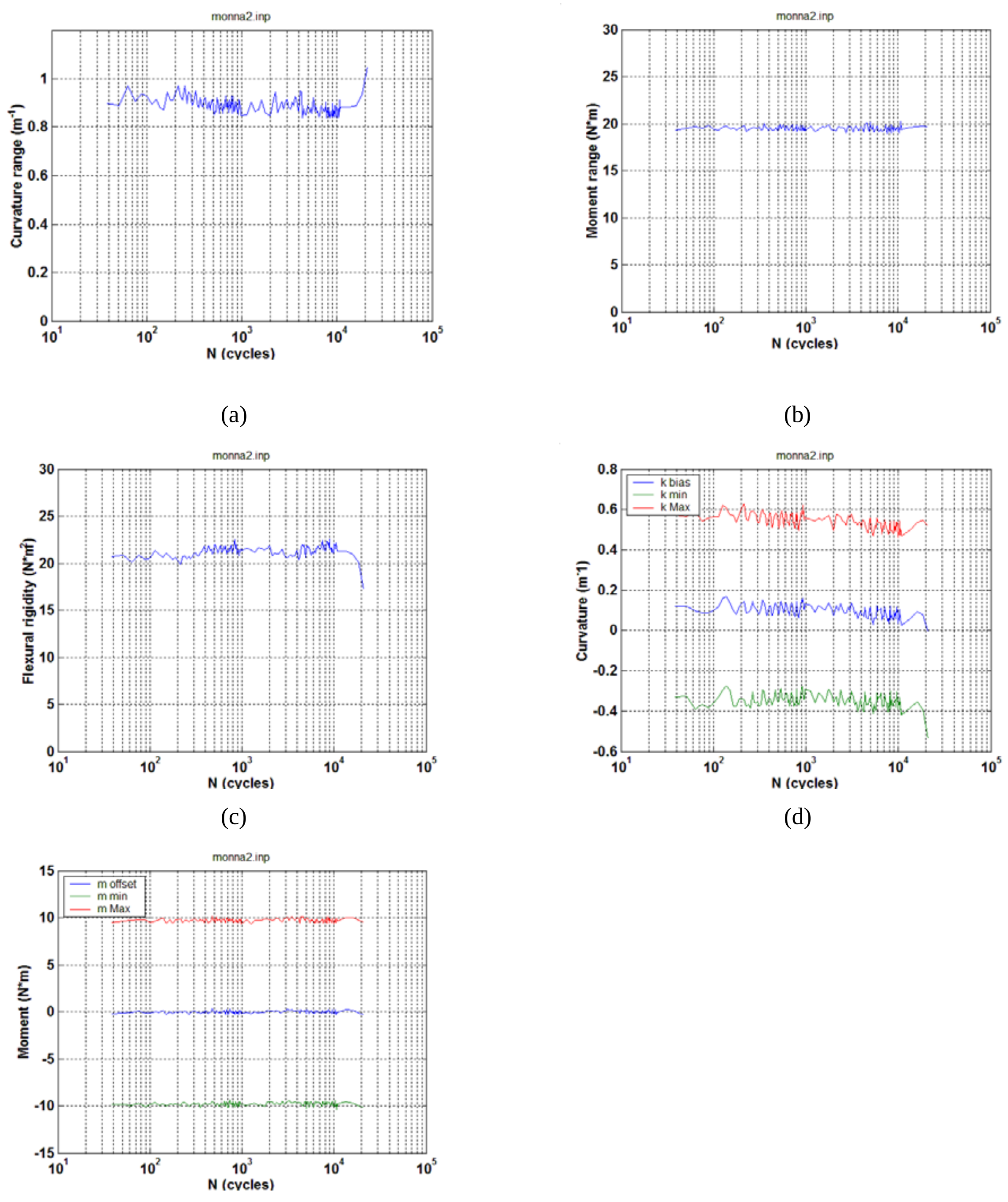

(a)

(b)

(c)

(d)

(e)

Fig. 29. Variations of (a) curvature range, (b) applied moment range, (c) flexural rigidity, (d) maximum and minimum values of curvature, and (e) maximum and minimum values of moment as a function of number of cycles for NA2 (651C5); $N_f = 2.2 \times 10^4$ cycles under ±10.16 N·m, 5 Hz.

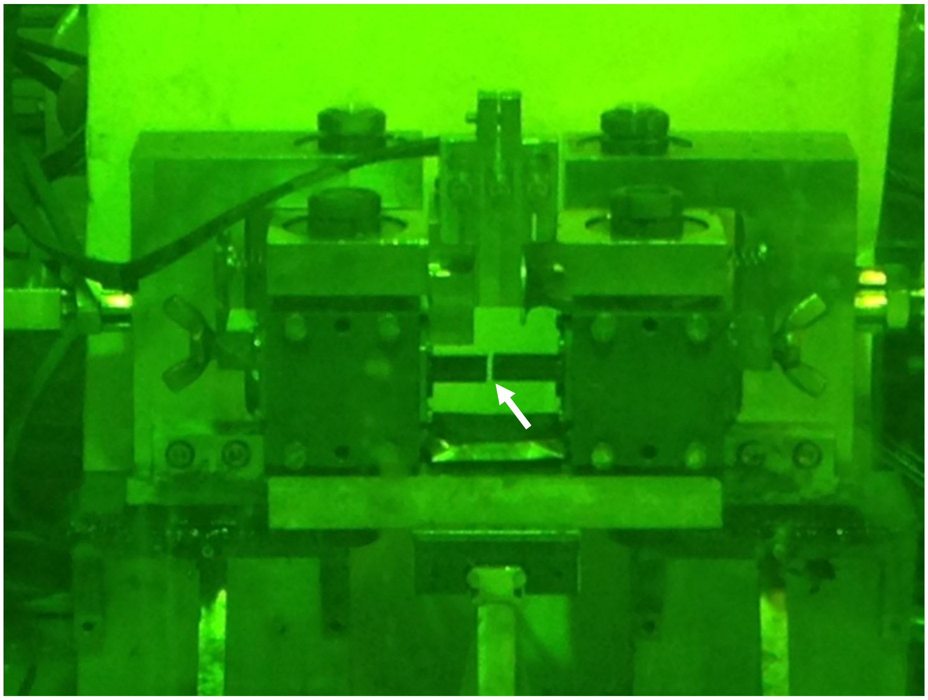

Fig. 30. Fracture location of NA2 (651C5), $N_f = 2.2 \times 10^4$ cycles under ±10.16 N·m, 5 Hz.

4.7.3 NA4/652B1B under 7.62 N·m 5Hz

The test on NA4 (652B1B) was conducted under ±7.62 N·m, 5 Hz. A fatigue life of 6.1 × 10^4 cycles was obtained.

Again, periodic quasistatic measurements of rod deformation were conducted using two relative displacement levels—0.8 and 1.6 mm—at the target intervals. Variations of the curvature, moment, and flexural rigidity as a function of number of cycles are given in Fig. 31. The initial values of flexural rigidity ranged between 24.5 and 28 Nm^2. The level of rigidity is apparently close to the values that were observed for NA1 and NA2. The flexural rigidity of NA4 exhibited an increasing trend during the period of the test cycle, especially in the case of the 0.8 mm measurement. This increasing trend was also observed in the variation of flexural rigidity (Fig. 32). At the same time, a positive offset of curvature was found for the rod under reverse bending. The mean value of curvature was around 0.05 m^{-1}.

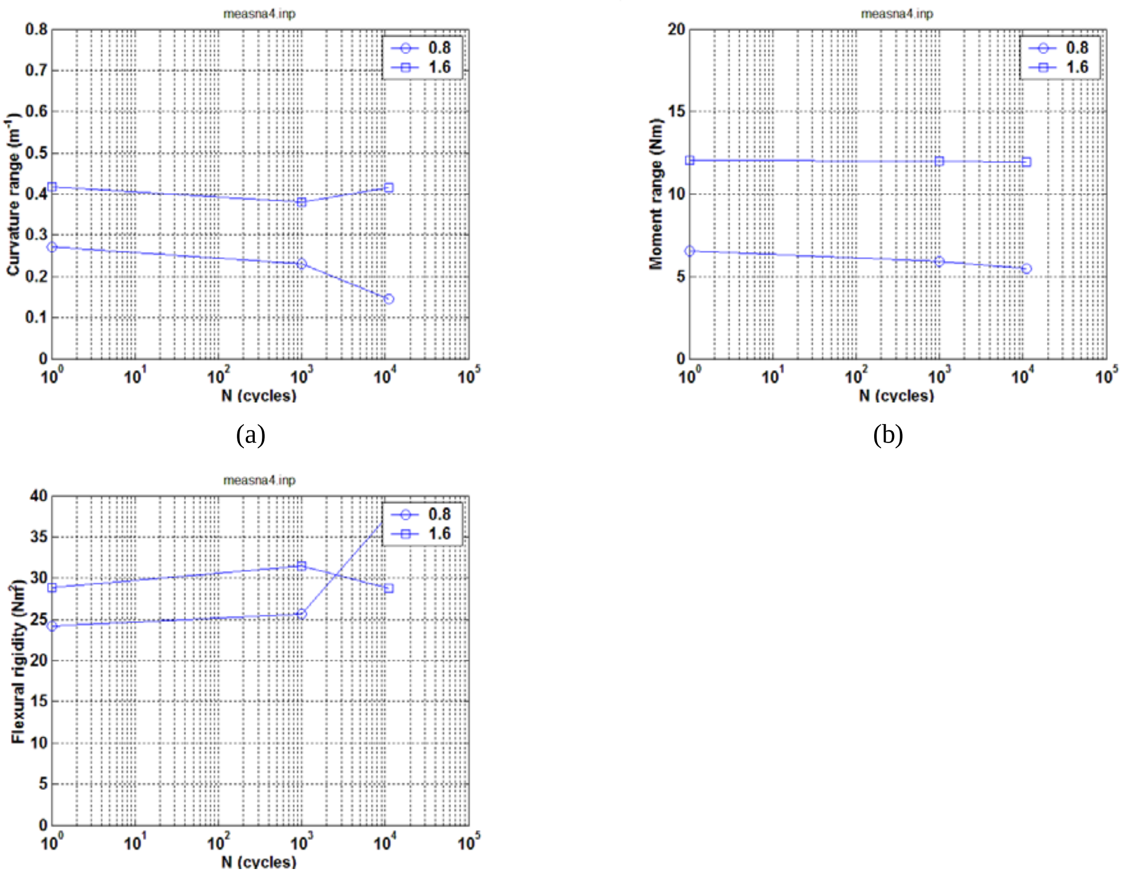

(a)

(b)

(c)

Fig. 31. Variations of (a) curvature range, (b) moment range, and (c) flexural rigidity as a function of number of cycles for NA4 (652B1B). Measurements were made with 1.0 and 2.0 mm relative displacements; N_f = 6.1 × 10^4 cycles under ±7.62 N·m, 5 Hz.

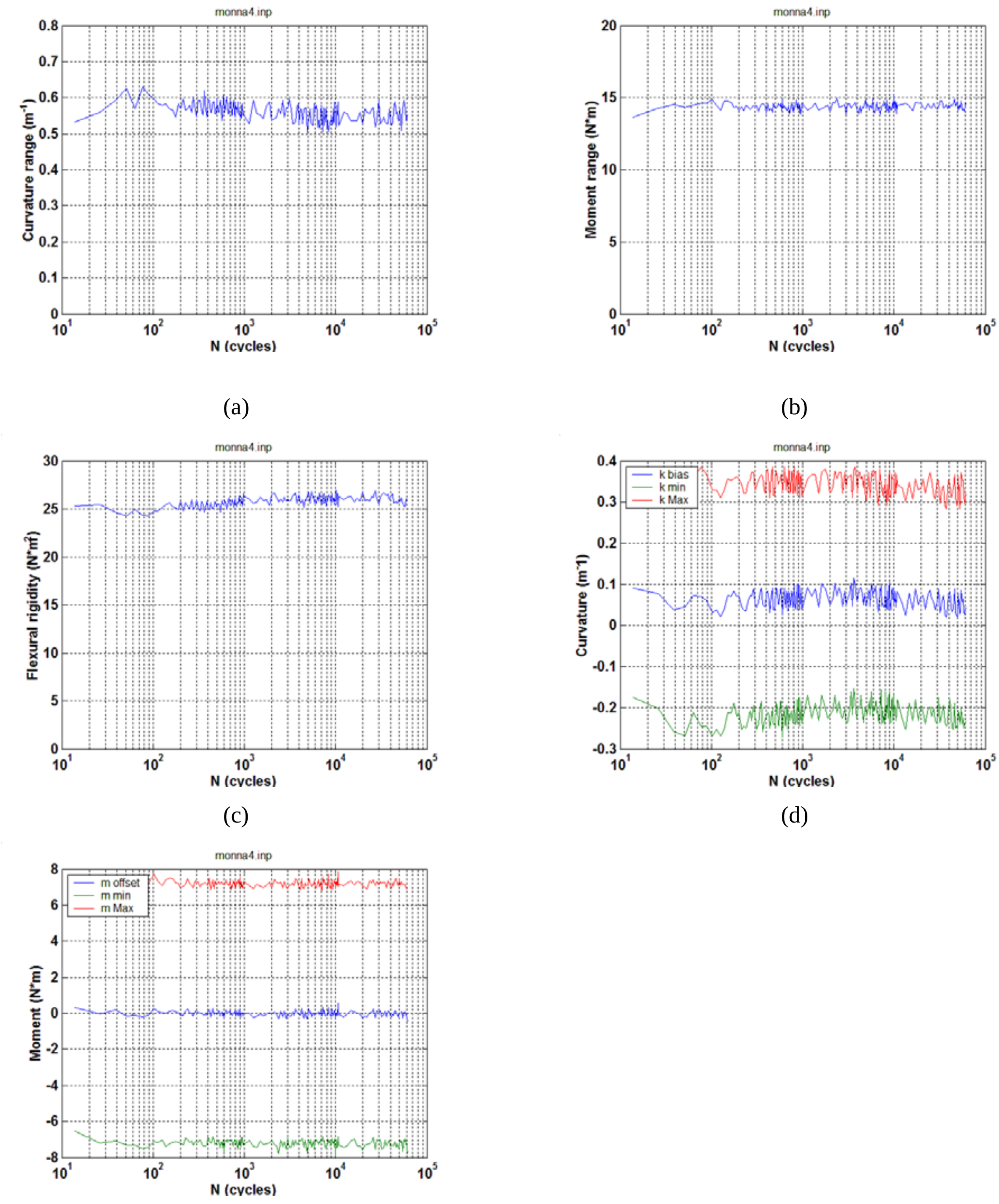

(a) (b)

(c) (d)

(e)

Fig. 32. Variations of (a) curvature range, (b) applied moment range, (c) flexural rigidity, (d) maximum and minimum values of curvature, and (e) maximum and minimum values of moment as a function of number of cycles for NA4 (652B1B); Nf = 6.1 × 104 cycles under ±7.62 N·m, 5 Hz.

4.8 Dynamic Testing of MOX UNF

4.8.1 MOX2/ MOX-A-12 under 10.16N·m 5Hz

The test on MOX2/MOX-A-12 was conducted under ±10.16 N·m, 5 Hz. A fatigue life of 3.70×10^4 cycles was obtained.

Periodic quasistatic measurements of rod deformation were conducted using two relative displacement levels—0.8 and 1.6 mm—at the selected target number of cycles as described above. Investigation into the distorted moment-curvature loop indicated that the distortion may result from a reduced sample rate. Therefore, the sampling rate was adjusted to that used for dynamic tests of HBR fuel. Time history of moment and curvature and curvature-moment loops obtained at the first cycle and 11,000 cycles are shown in Fig. 33. The regular curvature-moment loops were obtained with the modified data acquisition setting.

The curvature range–moment range and flexural rigidity are illustrated in Fig. 34. The variations of these quantities as a function of number of cycles are given in Fig. 35. The rigidity of the measurements showed a clear decreasing trend starting with 24 Nm^2 and then dropping to 20 Nm^2 at 1.1×10^4 cycles.

The curvature range, moment range, and flexural rigidity based on online monitoring data are presented in Fig. 36, along with the maxima and minima. Online monitoring showed that flexural rigidity was essentially stable with a small amount of decrease (19 to 18 Nm^2) prior to the failure. The degree of decrease is lower than the value seen in the measurement. At the same time, the positive offset of curvature with an initial level of 0.1 m^{-1} tended to become smaller during the cycle test. Moment and curvature time history and moment-curvature loops based on online monitoring at early and late stages of dynamic testing are illustrated in Fig. 37. It can be seen that moment-curvature loops based on online monitoring were actually well defined. Except for a little drifting toward the left, no significant change can be observed between loops measured in the two points of the cycle process.

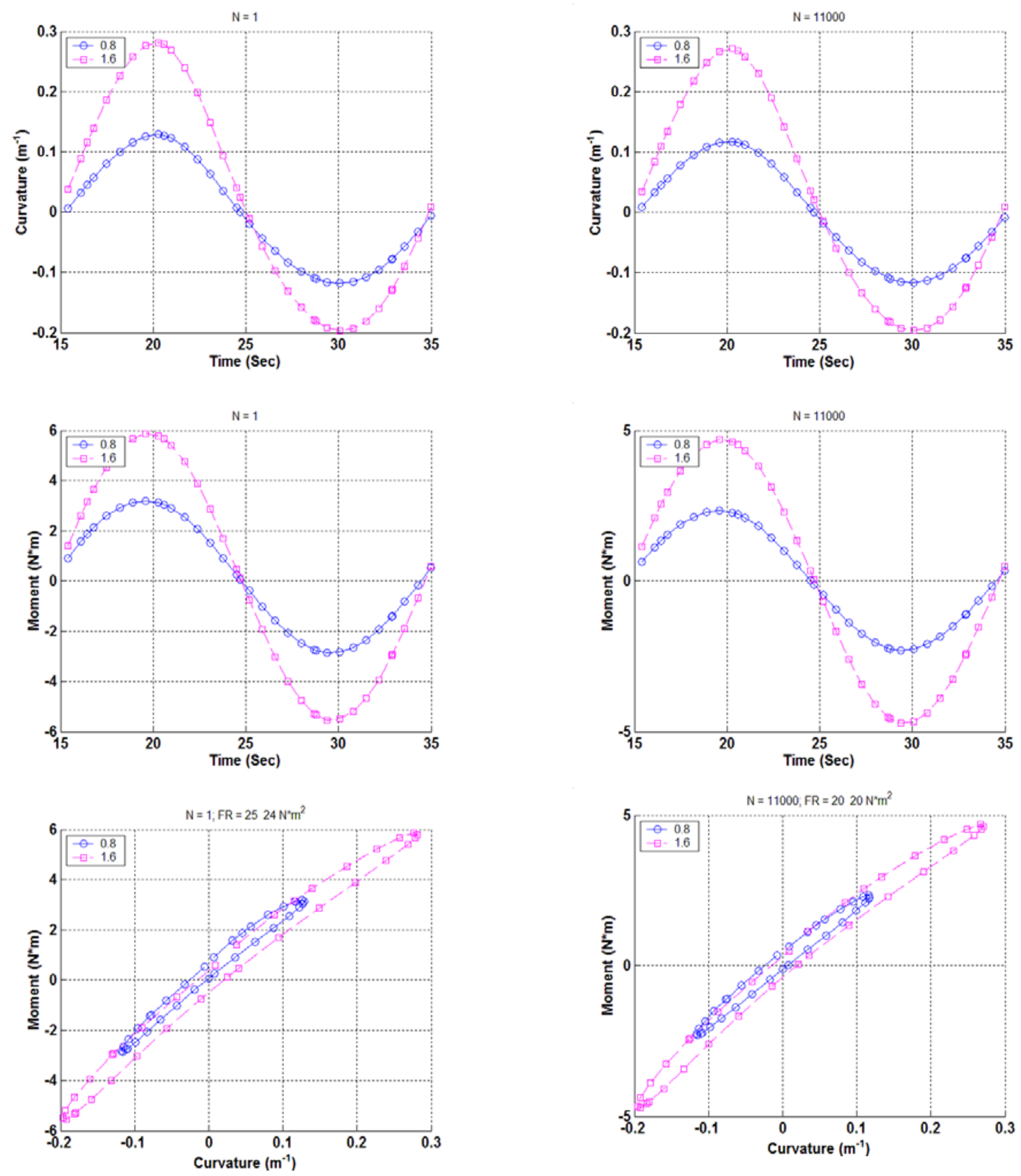

(a) (b)

Fig. 33. Moment and curvature as a function of time and moment-curvature loops based on measurements when (a) N=1 and (b) N = 111,000 cycles for MOX2 (MOX-A-12). Measurements were made with 0.8 and 1.6 mm relative displacements; N_f = 3.7 × 10^4 cycles under ±10.16 N·m, 5 Hz.

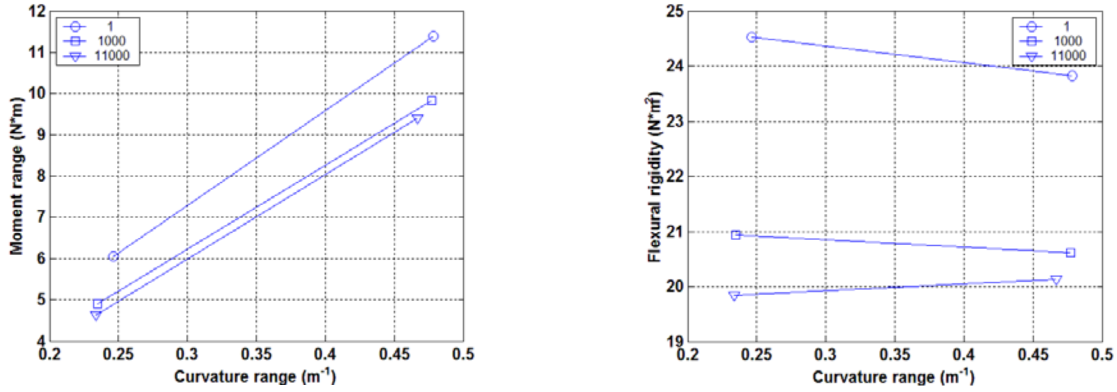

(a) (b)

Fig. 34. (a) Moment-curvature relation and (b) moment-flexural-rigidity relation at various numbers of cycles for MOX (MOX-A-12). Measurements were made with 0.8 and 1.6 mm relative displacements; $N_f = 3.7 \times 10^4$ cycles under ±10.16 N·m, 5 Hz.

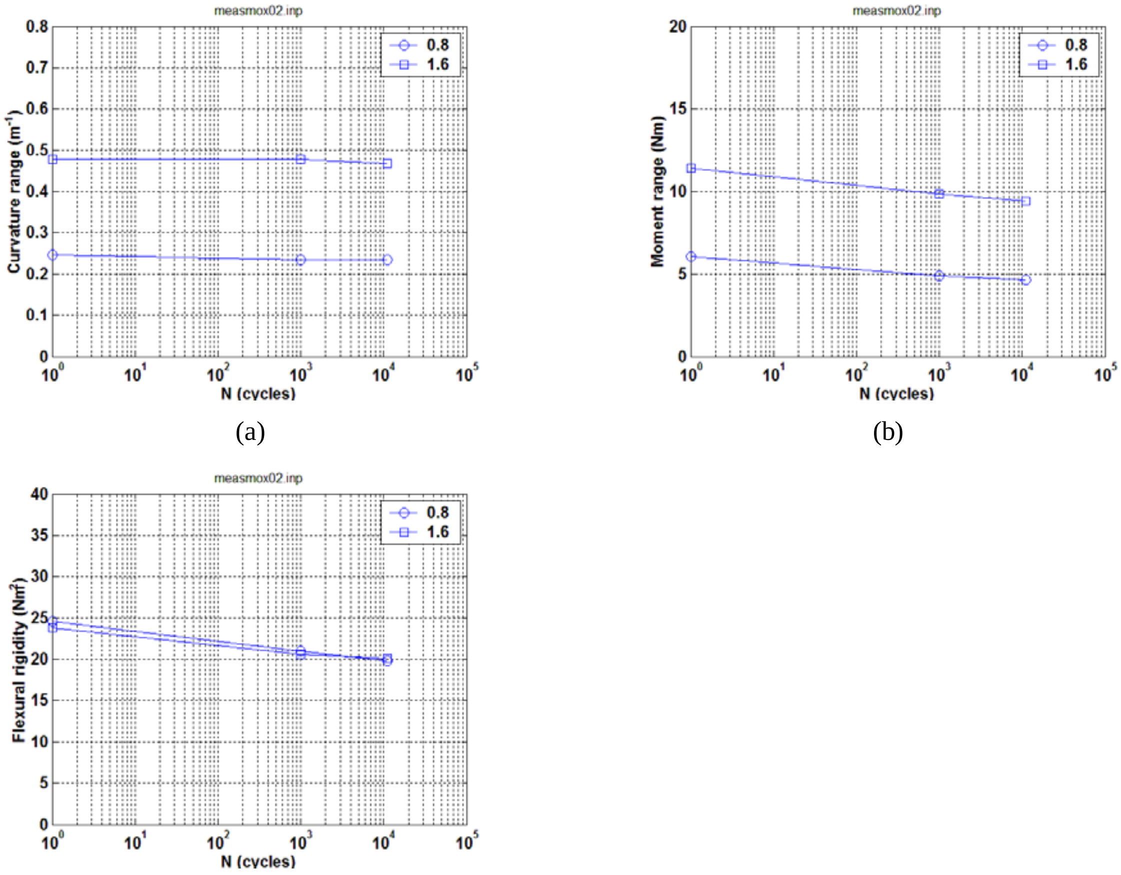

(a) (b)

(c)

Fig. 35. Variations of (a) curvature range, (b) moment range, and (c) flexural rigidity as a function of number of cycles for MOX (MOX-A-12). Measurements were made with 0.8 and 1.6 mm relative displacements; $N_f = 3.7 \times 10^4$ cycles under ±10.16 N·m, 5 Hz.

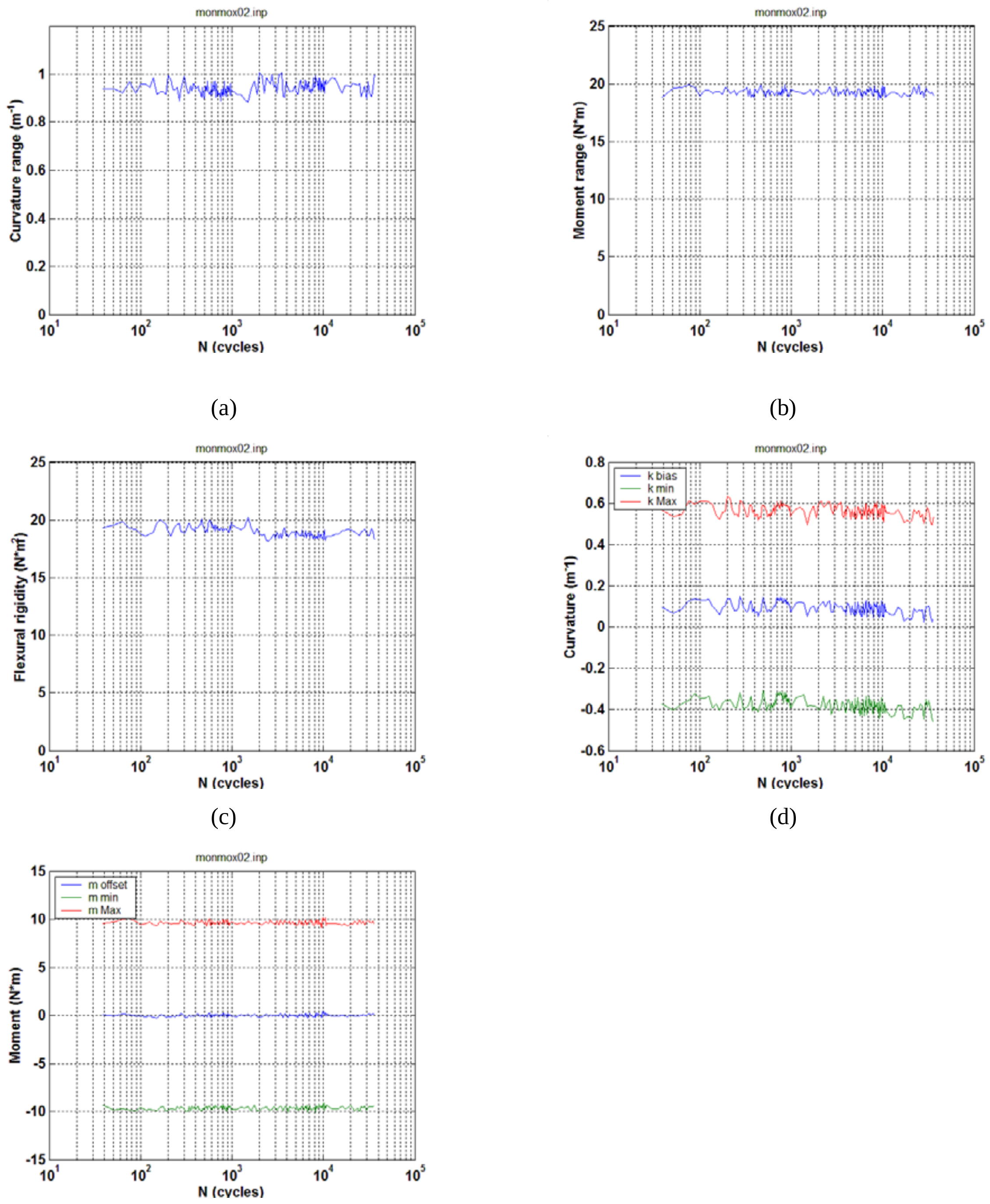

(a) (b)

(c) (d)

(e)

Fig. 36. Variations of (a) curvature range, (b) applied moment range, (c) flexural rigidity, (d) maximum and minimum values of curvature, and (e) maximum and minimum values of moment as a function of number of cycles for MOX2 (MOX-A-12); $N_f = 3.7 \times 10^4$ cycles under ±10.16 N·m, 5 Hz.

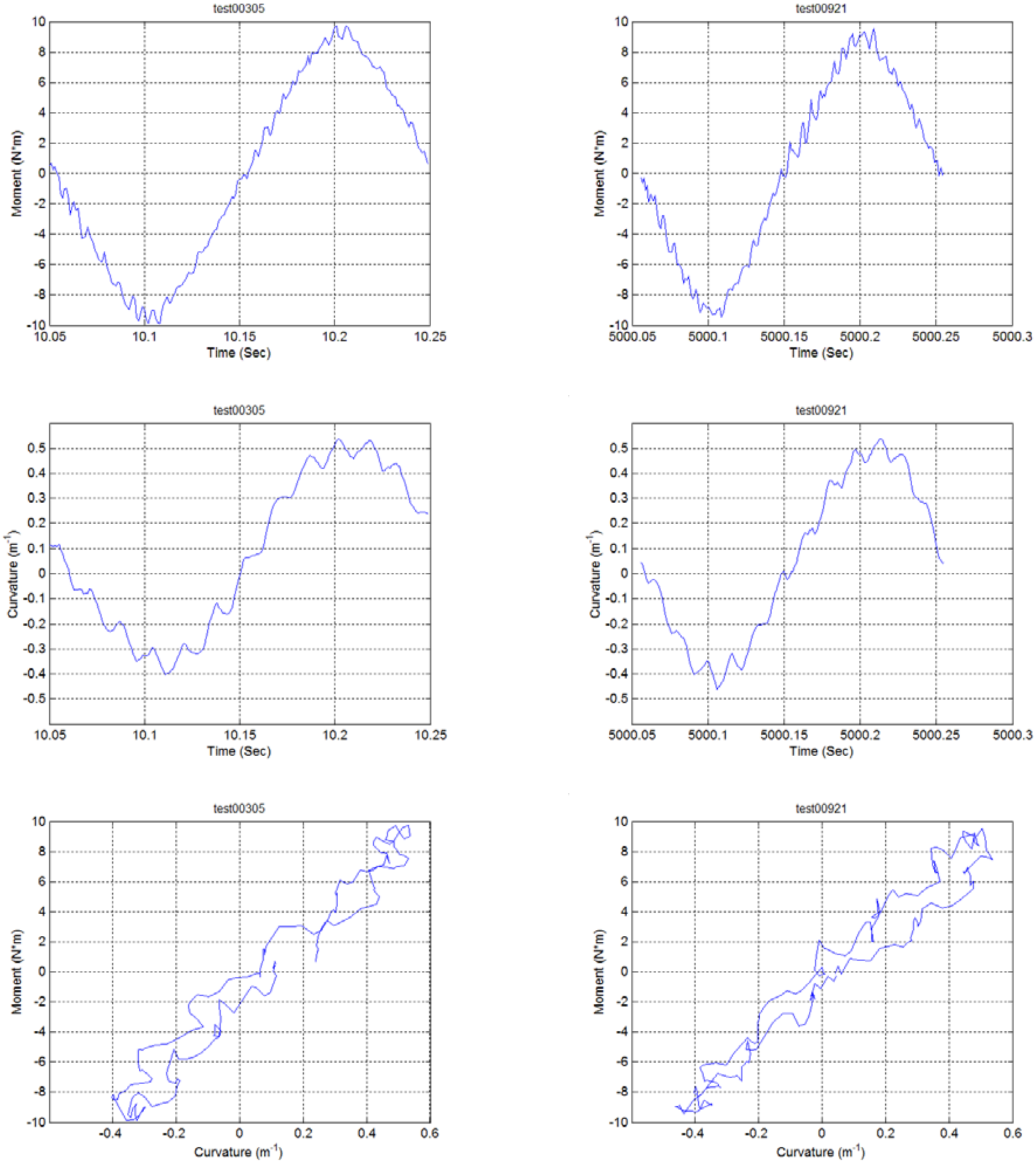

(a)

(b)

Fig. 37. Moment and curvature as a function of time and moment-curvature loops at (a) 50 cycles and (b) 3.6 × 10^4 cycles; results are based on online monitoring of MOX2 (MOX-A-12); N_f = 3.7 × 10^4 cycles under ±10.16 N·m, 5 Hz.

4.8.2 MOX4/ MOX-B-05 under 5.08N·m 5Hz

The test on MOX4/MOX-B-05 was conducted under ±5.08 N·m, 5 Hz. A fatigue life of 2.15×10^6 cycles was obtained.

Periodic quasistatic measurements of rod deformation were conducted using two relative displacement levels—0.4 and 0.7mm—at the selected target number of cycles as described above, and results are given in Fig. 38. The moment range exhibited a defined decreasing trend, and flexural rigidity showed a similar decrease. The effect of measurement displacement on the rigidity response was seen at the beginning, but it became diminished at the later stage of the test. The initial level of rigidity was a little higher than that of MOX2, perhaps due to the smaller displacement used in the measurement of this specimen. The overall decrease in rigidity was about 20%.

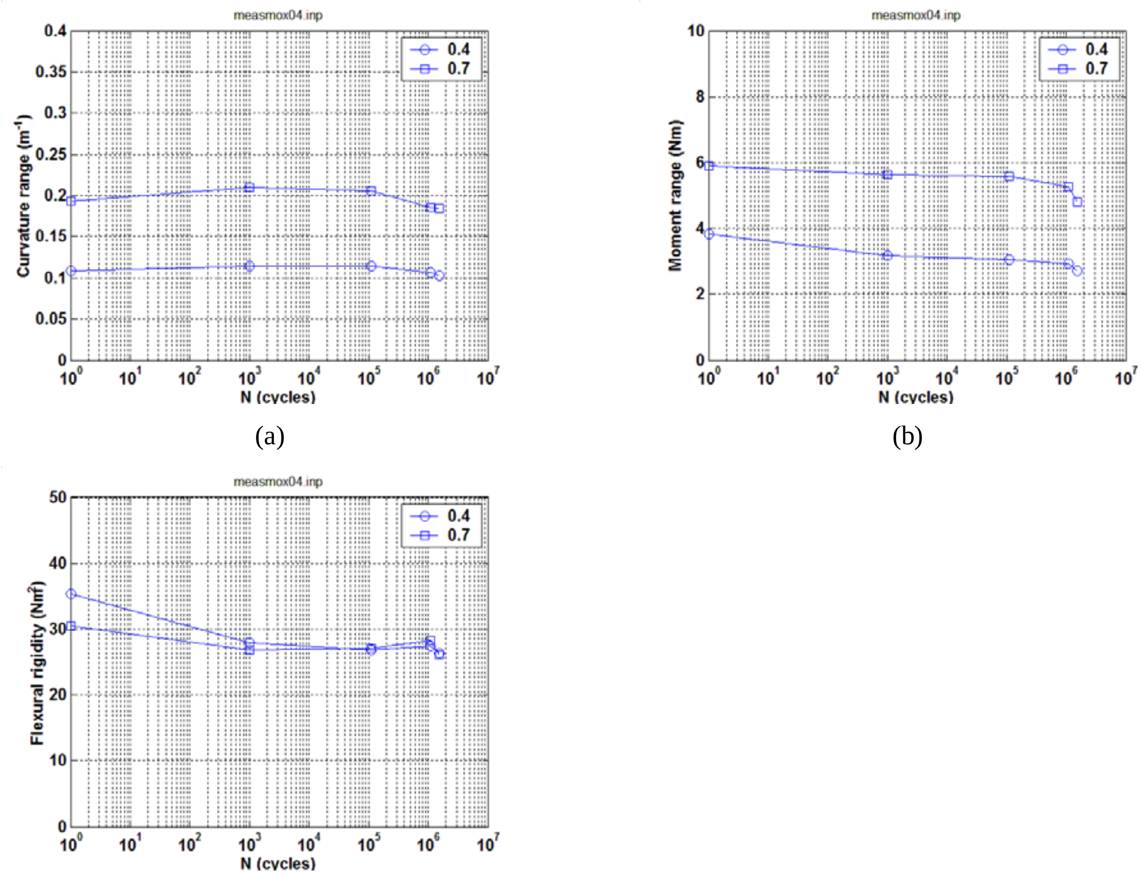

(a) (b)

(c)

Fig. 38. Variations of (a) curvature range, (b) moment range, and (c) flexural rigidity as a function of number of cycles for MOX4 (MOX-B-05). Measurements were made with 0.4 and 0.7 mm relative displacements; $N_f = 2.15 \times 10^6$ cycles under ±5.08 N·m, 5 Hz.

Flexural rigidity from online monitoring exhibited a rise-and-fall trend during the cycle test, as shown in Fig. 39. The rigidity started with 22.5, increased to 24.5, and dropped to 23 Nm^2 prior to the failure. Detailed examination showed that the moment-curvature loop drifted downward along with the accumulated number of cycles, as can be seen from the parallel curvature fatigue curves. The fatigue failure seemed related to the single-side fracture development.

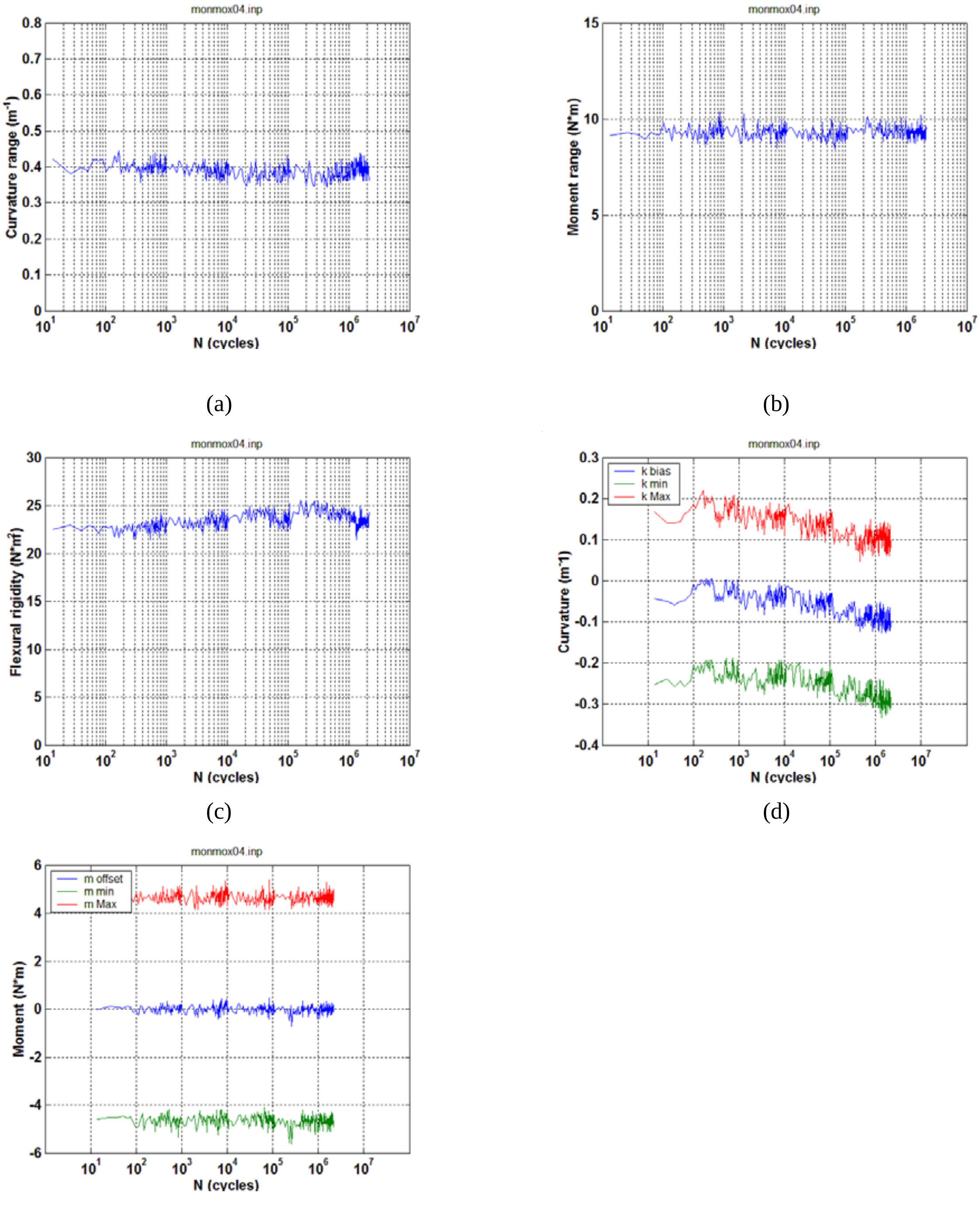

(a) (b)

(c) (d)

(e)

Fig. 39. Variations of (a) curvature range, (b) applied moment range, (c) flexural rigidity, (d) maximum and minimum values of curvature, and (e) maximum and minimum values of moment as a function of number of cycles for MOX4 (MOX-B-05). $N_f = 2.15 \times 10^6$ cycles under ±5.08 N·m, 5 Hz.

4.8.3 MOX5/ MOX-B-06 under 6.10N·m 5Hz

The test on MOX5/MOX-B-06 was conducted under ±6.10 N·m, 5 Hz. The applied moment amplitude was between those of MOX2 and MOX4, and a fatigue life between those was also observed (4.49×10^5).

Periodic quasistatic measurements of rod deformation were conducted using two relative displacement levels: 0.4 and 0.7 mm at the selected target number of cycles as described above and results are given in Fig. 40. The prefatigue rigidity was about 30 Nm^2, and that was a little lower than that of MOX4, even though the measurement displacements were the same. This reflected the difference of mechanical response of various rods under deflection. As can be seen, the flexural rigidity showed a decrease with about 13% drop at the later stage of fatigue.

Online monitoring (Fig. 41) showed a well-defined decreasing trend on flexural rigidity with same level of decrease percentage as seen in measurement. Similar downward drifting to that in MOX4 was seen here along with the accumulated number of cycles. The fatigue failure seemed related to the single-side fracture development.

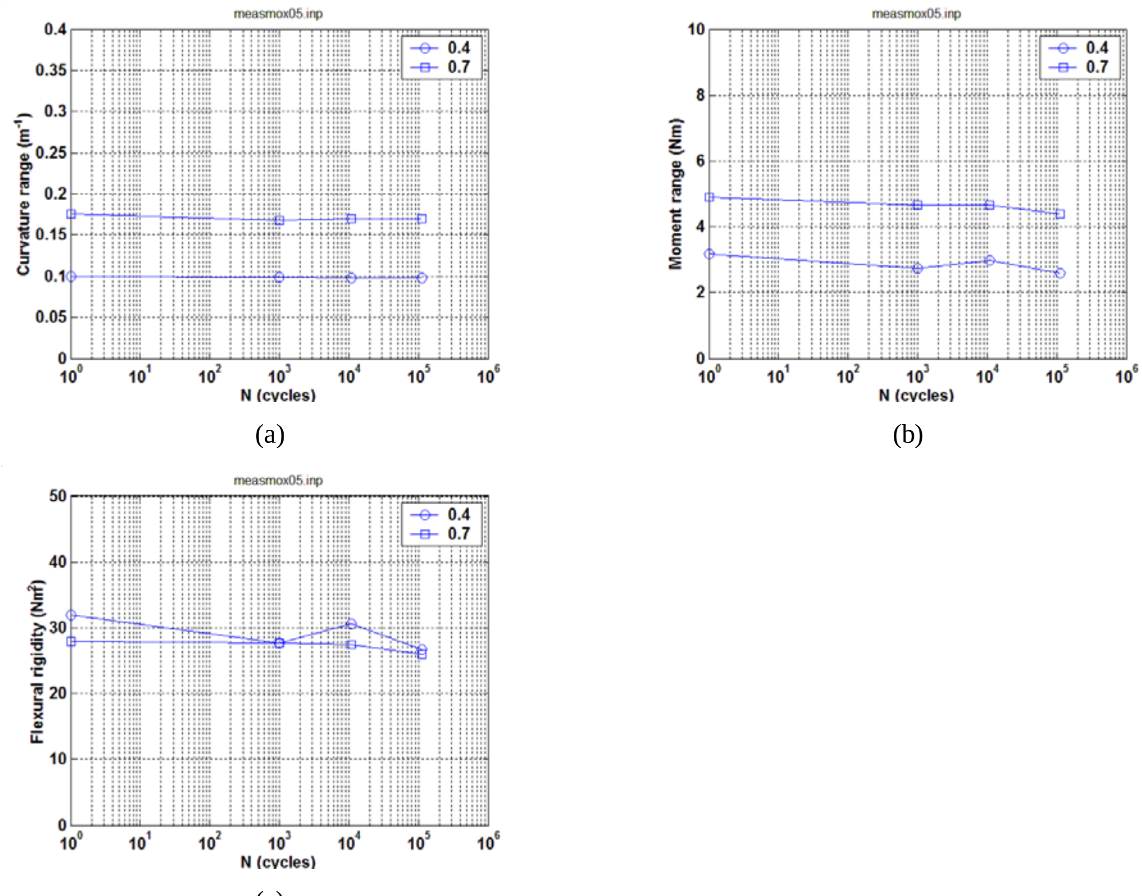

(a)

(b)

(c)

Fig. 40. Variations of (a) curvature range, (b) moment range, and (c) flexural rigidity as a function of number of cycles for MOX5 (MOX-B-06). Measurements were made with 0.4 and 0.7 mm relative displacements; $N_f = 4.49 \times 10^5$ cycles under ±6.10 N·m, 5 Hz.

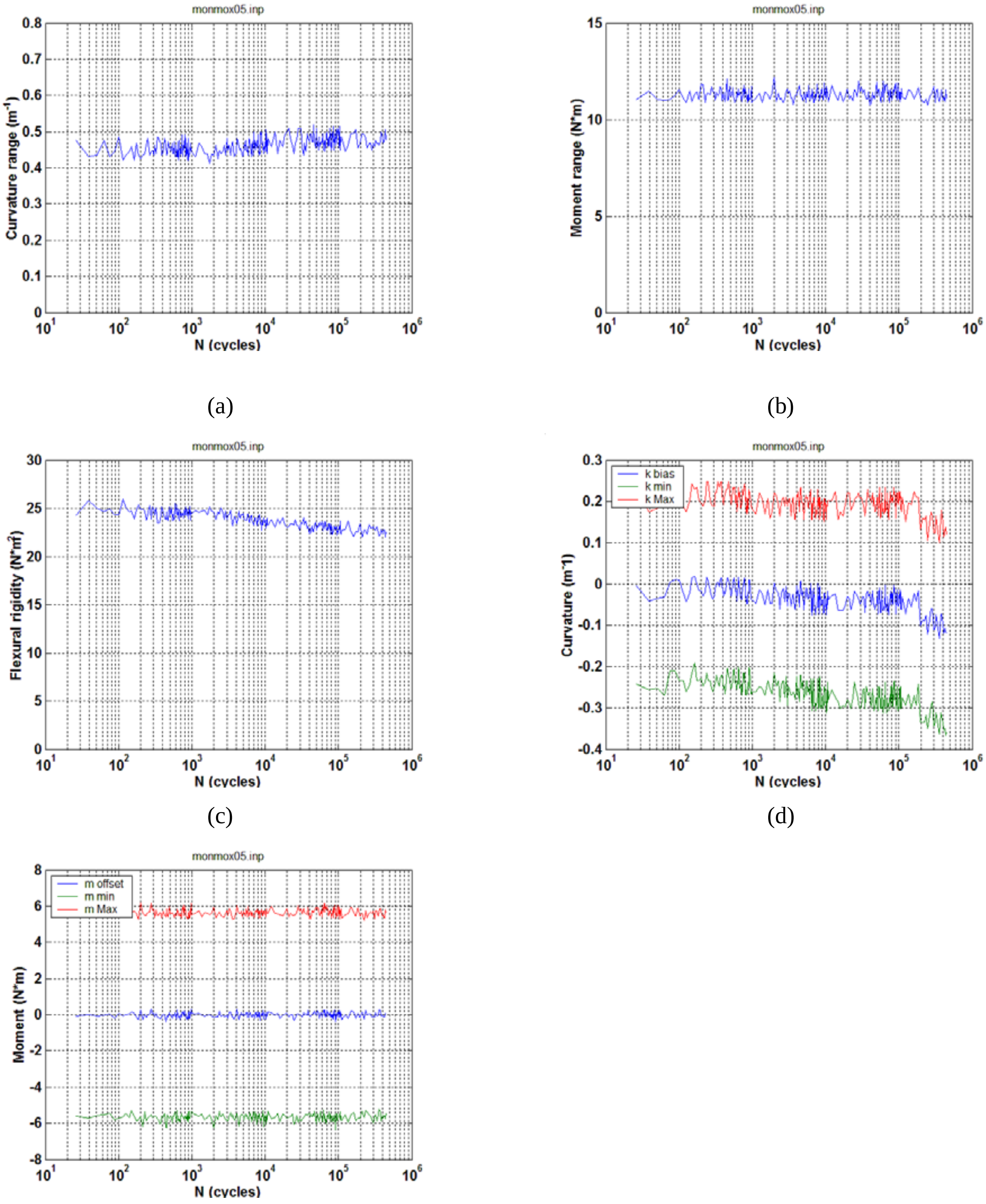

(a)

(b)

(c)

(d)

(e)

Fig. 41. Variations of (a) curvature range, (b) applied moment range, (c) flexural rigidity, (d) maximum and minimum values of curvature, and (e) maximum and minimum values of moment as a function of number of cycles for MOX5 (MOX-B-06). $N_f = 4.49 \times 10^5$ cycles under ±6.10 N·m, 5 Hz.

4.8.4 MOX6/ MOX-B-07 under 5.08N·m 5Hz

The test on MOX6/MOX-B-07 was conducted under ±5.08 N·m, 5 Hz with the same amplitude as that of MOX4. In order to test the impact of a handling drop or transient shock under NCT on the fatigue life of UNF, after the two endcaps were put on, the MOX6 specimen was dropped twice from approximately two feet high in a horizontal orientation. The test was conducted using the same procedure as used in all other dynamic tests [11]. The MOX6 sample failed at 5.42×10^5 cycles, which was much shorter than that of MOX4 (2.15×10^6 cycles).

Under 0.4 and 0.7 mm, the initial rigidity of MOX6 was between 25 and 27 Nm^2. For the same relative displacements, the level of rigidity of MOX6 was obviously lower than those of MOX 4 and 5. This result indicates that the drop from two feet may have induced additional damage to the rod and thus may have reduced the fatigue life observed.

Periodic quasistatic measurements of rod deformation were conducted routinely using two relative displacement levels—0.4 and 0.7 mm—at the selected target number of cycles as described above, and results are given in Fig. 42. As can be seen, the flexural rigidity showed a certain amount of decrease, with the largest drop at about 15% occurring under 0.4 mm measurement.

As with MOX4, online monitoring of MOX6 (Fig. 43) showed a rise-and-fall pattern in the variation of flexural rigidity. However, the overall rigidity of MOX6 (20 Nm^2) was lower than that of MOX4. Therefore, the reduced rigidity was exhibited in both the periodic measurement process and in online monitoring. This is an important indication that dropping or transient shocks of NCT can have accelerated aging effect on the fatigue performance of HBU UNF. The observation and related mechanisms remain to be confirmed and investigated further.

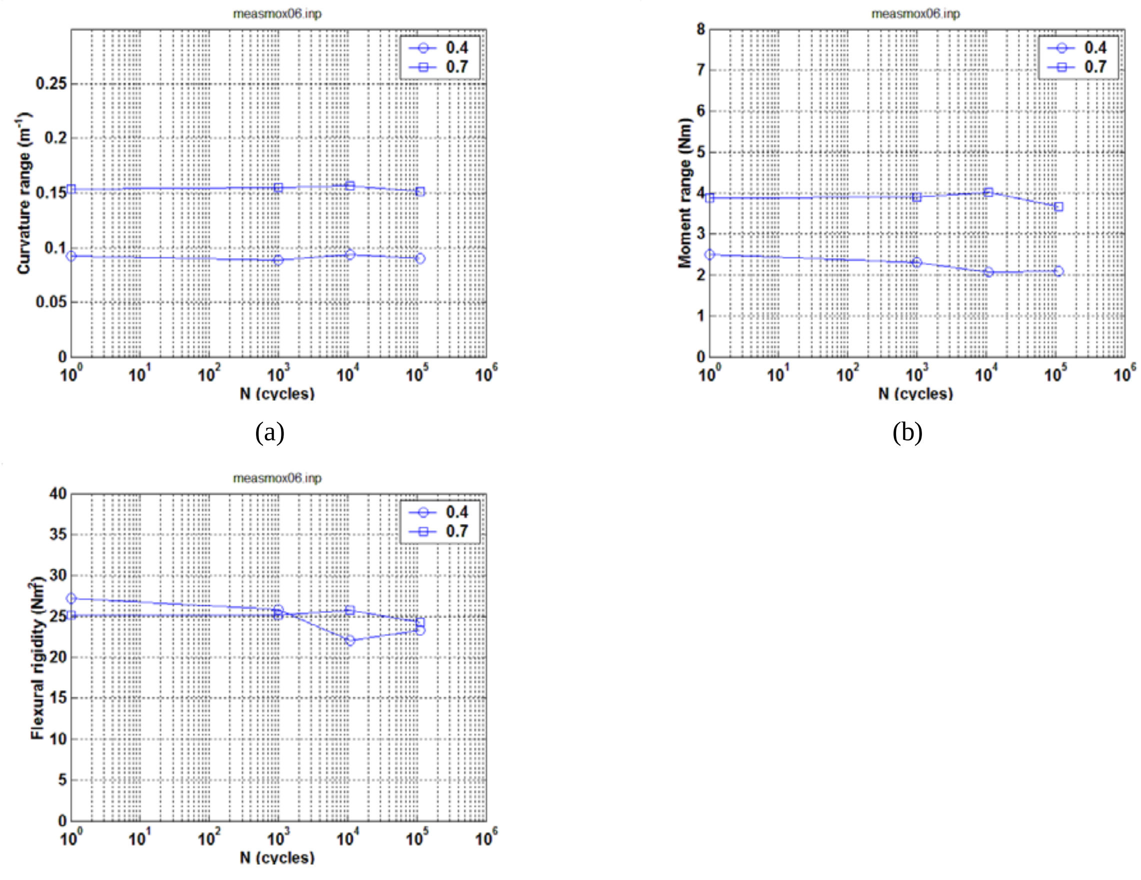

(a)

(b)

(c)

Fig. 42. Variations of (a) curvature range, (b) moment range, and (c) flexural rigidity as a function of number of cycles for MOX6 (MOX-B-07). Measurements were made with 0.4 and 0.7 mm relative displacements. $N_f = 5.42 \times 10^5$ cycles under ±5.08 N·m, 5 Hz.

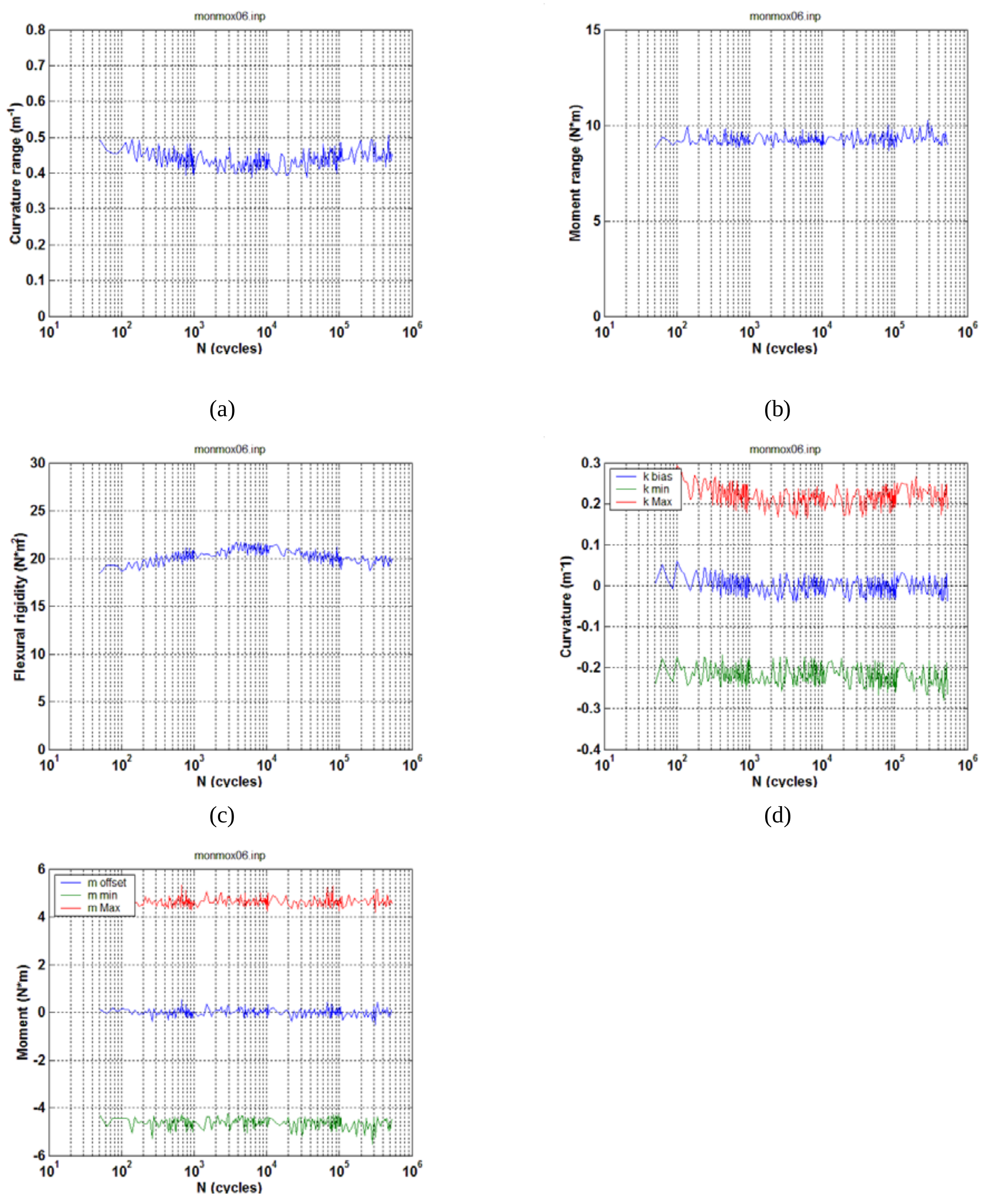

(a)

(b)

(c)

(d)

(e)

Fig. 43. Variations of (a) curvature range, (b) applied moment range, (c) flexural rigidity, (d) maximum and minimum values of curvature, and (e) maximum and minimum values of moment as a function of number of cycles for MOX6 (MOX-B-07). $N_f = 5.42 \times 10^5$ cycles under ±5.08 N·m, 5 Hz.

4.9 Discussion

4.9.1 Static Response of UNF

Figure 44 summarizes the equivalent stress and strain results from static testing on all UNF rods (HBR, NA M5^{TM,} and MOX M5^{TM}). The static responses of NA M5^{TM} and MOX M5^{TM} specimens were quite consistent. The three stages of curve (Fig. 44) can be identified with the first and second deflection points (approximately 90 and 300 MPa, respectively). The curves of NA and MOX fuels were obviously well below those of HBR fuels. The maximum stress of HBR fuels at the same relative displacement (24.00 mm) was between 733 and 748 MPa, while those of NA and MOX were between 510 and 530 MPa. The maximum strains among the three tested fuels were close in value, ranging from 1.67 to 1.98%. The stress level at the first deflection for NA/MOX M5^{TM} fuels was located near 100 MPa, and the second was between 300 and 400 MPa. These stress levels are lower than those of the HBR fuel [11].

A comparison revealed a large discrepancy between the curves of CIRFT static results and the Pacific Northwest National Laboratory (PNNL) data for Zircaloy-4 cladding. A preliminary investigation showed that the reduction of pellet inertia by 50% could actually bring the CIRFT testing curve up enough to close the gap, i.e., $I = I_c + 0.5*I_p$. The same procedure was applied to processing NA and MOX fuel data; the results are given in Fig. 45. The use of reduced inertia of pellet in the calculation of equivalent stress raised the stress as expected. For example, the maximum attained levels are between 700 and 725 MPa. It is emphasized that the concept of reduced pellet inertia of moment and the use of Eqs. (2) and (3) were made to demonstrate the relative stress levels between different UNFs, and more modelling effort is needed to understand the deformation mechanisms and to predict the response of the UNF rod under the corresponding loading condition.

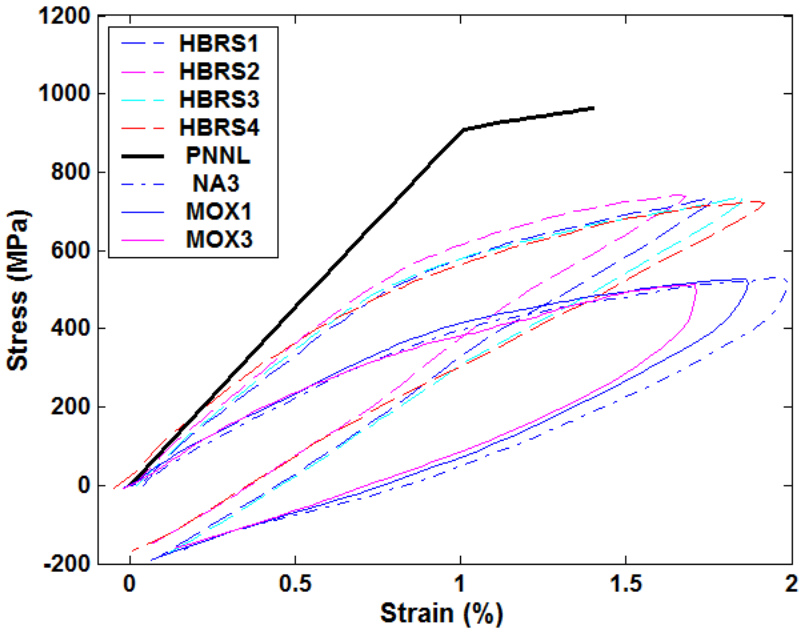

Fig. 44. Stress-strain curves based on static testing results for HBR, NA and MOX UNF. Relative displacement was 24.00 mm; the loading/unloading rate at each point was 0.1/0.2 mm/s.

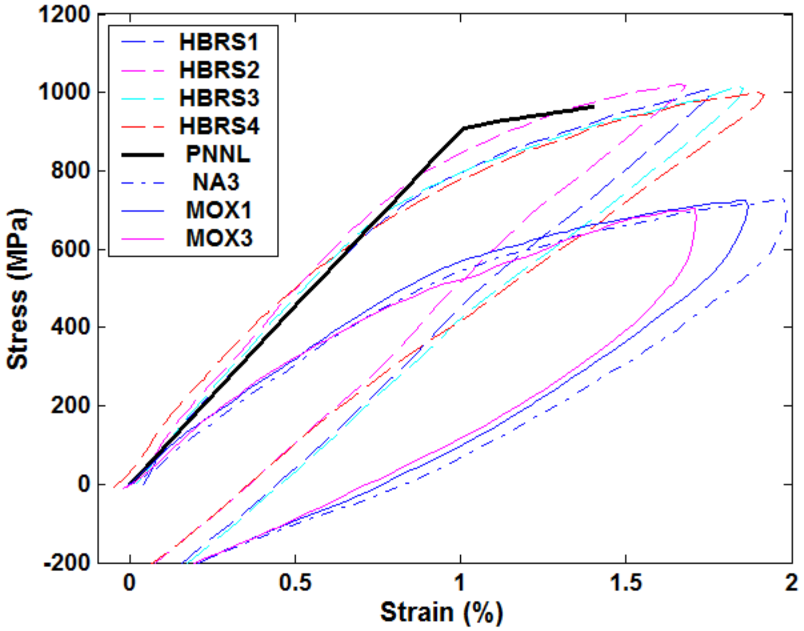

Fig. 45. Stress-strain curves based on static testing results for HBR, NA, and MOX UNF. The equivalent stress is based on Eq. (2) with $I = I_c + 0.5*I_p$.

4.9.2 Fatigue Life of UNF

A summary of dynamic testing results for all of the UNF rods is represented in Fig. 46 in terms of equivalent strain amplitude. Under the same level of amplitudes, the NA and MOX fuels showed a shorter fatigue life than HBR fuel. The difference between NA/MOX and HBR fuel is several tens of thousands of cycles. These data correspond with the earlier yielding of NA/MOX fuels seen in Fig. 45. However, the fatigue mechanism remains to be investigated.

The alternate form is also given in Fig. 47 in terms of maximum of absolute strain extremes.

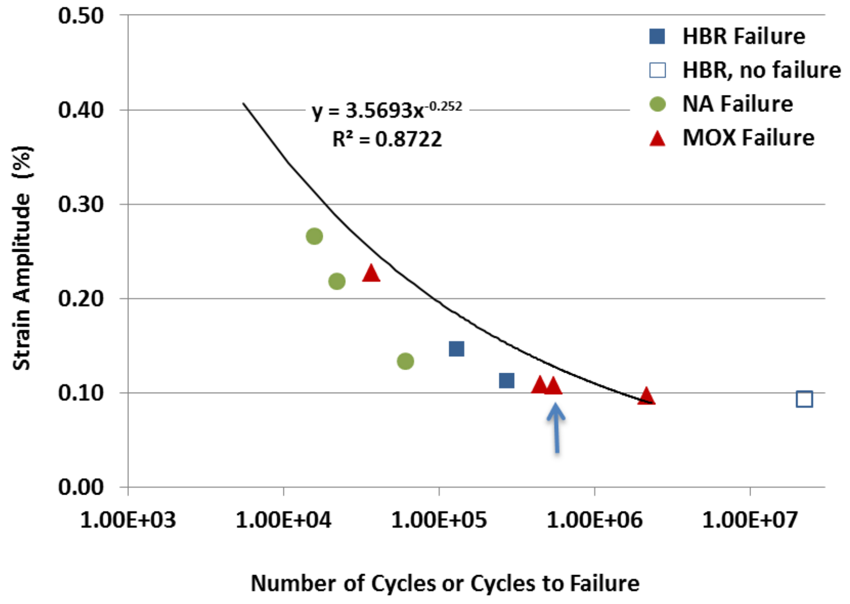

Fig. 46. Strain amplitudes as a function of number of cycles; results are based on CIRFT testing at 5 Hz. The power function was obtained from curve fitting based on the HBR data set [11]. The data point with the arrow represents the two foot drop test of the specimen.

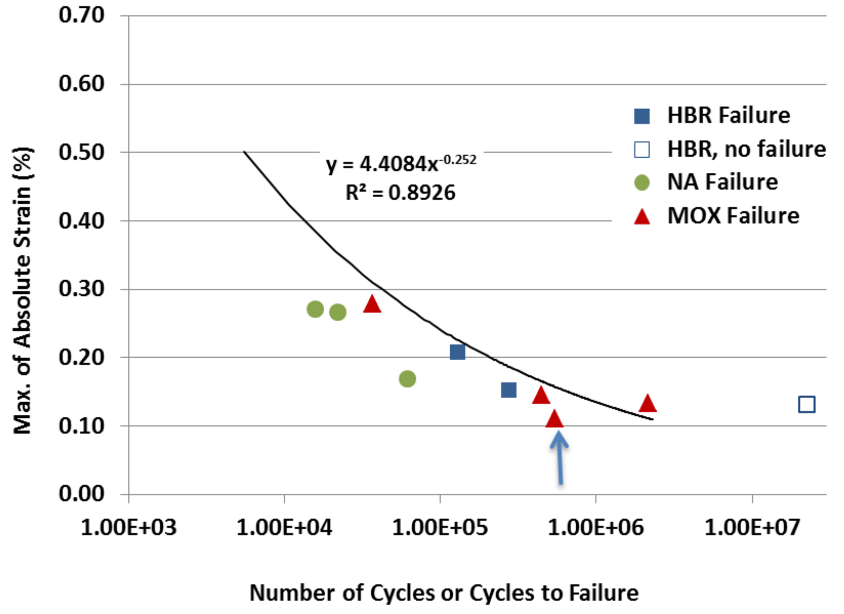

Fig. 47. Maxima of absolute strain extremes as a function of number of cycles; results are based on CIRFT testing at 5 Hz. The power function was obtained from curve fitting based on the HBR data set [11]. The data point with the arrow represents the two foot drop test of the specimen.

5 FINITE ELEMENT ANALYSIS OF M5^{TM} CLAD MATERIAL

5.1 Introduction

The finite element analysis (FEA) model of an M5^{TM} fuel rod system is formed by UO_2 pellets and M5^{TM} cladding. It incorporates appropriate boundary conditions including the bonding layer at clad/pellet interfaces. The model consists of a fuel rod with a 3-dimensional (3D) representation of fuel pellets, clad, and possible combinations of gaps at the pellet-pellet and pellet-clad interfaces. The ABAQUS code was used, and the fuel rod was represented by a beam element with the associated effective stiffness. This approach was used to obtain the effective properties of the beam elements for use as input for further development of the detailed UNF assembly model. The approach is also designed to estimate the damping properties of the beam elements due to frictional resistance between the clad and the embedded pellets. This pellet-clad interaction modeling uses a “contact element” algorithm and can be further implemented into other embedded boundary conditions such as internal pressure and residual stress.

This study provides detailed explanations of the effects of pellet-pellet and pellet-clad interactions—including pellet fracture and pellet-clad bonding efficiency—on the clad performance reliability. The FEA simulation results were also calibrated and benchmarked with fatigue aging data [10] obtained from ORNL reversal bending fatigue testing.

5.2 FEA Models of Fuel Rod with M5^{TM} cladding

Following the method specified in References [14–15], ABAQUS was used for a structural analysis and interfacial bonding evaluation of fuel rods with M5^{TM} cladding. The rods were tested in a hot cell environment in the CIRFT developed by ORNL [6–8]. To validate the simulation results, the fuel rod materials in the hot-cell tests were used in the FEA. The pellet material was UO_2, and the clad material was M5^{TM}. An epoxy layer was used as an interface bonding material to simulate fused areas. Table 5 lists the material properties of the fuel rod.

Table 5. Mechanical properties of the fuel rod

Material	Young’s modulus (psi)	Poisson’s ratio	Yield strength (psi)	Density (lb/in^3)
UO_2[a]	2.92e7	0.32	3.11e5	0.396
M5^{TM}[b]	1.46e7	0.326	9.85e4	0.237
Epoxy[a]	5.076e5	0.37	1.00e4	0.0452

[a] Reference [4]
[b] Reference [16]

5.2.1 Good Interface Bonding and No Fuel Rod System Fracture

Figure 48 shows the geometry of a U-frame bending fatigue testing system with a coplanar configuration for the fuel rod in which the rod specimen is located in the same plane as that of connectors. The two inch gauge section is outlined in black. A finite element model, established to represent the two inch gauge section of the test specimen, is referred to as the “clad-epoxy-pellet section model.” Figure 49 shows the fuel pellet designed by AREVA Front End Business Group for nuclear reactors. The measured outer diameter (OD) of the clad is 0.374 in. The cladding thickness is 0.0225 in., so the inner diameter (ID) is 0.329 in. Figure 49 gives a clear view of the fuel pellet, which is 0.435 in. long, much less than the 0.6 in. length of the surrogate rod in a previous report [14]. The pellet ends dish in to reduce pellet surface clinging (Fig. 49). The pellet OD is 0.3225 in. A fuel pellet was modeled by FEA to represent the real testing sample (Fig. 50). Both ends of the pellet were constructed with a dish diameter of 0.26 in. and a depth of 0.001in. so that the end surfaces would not touch at the dished-in area.

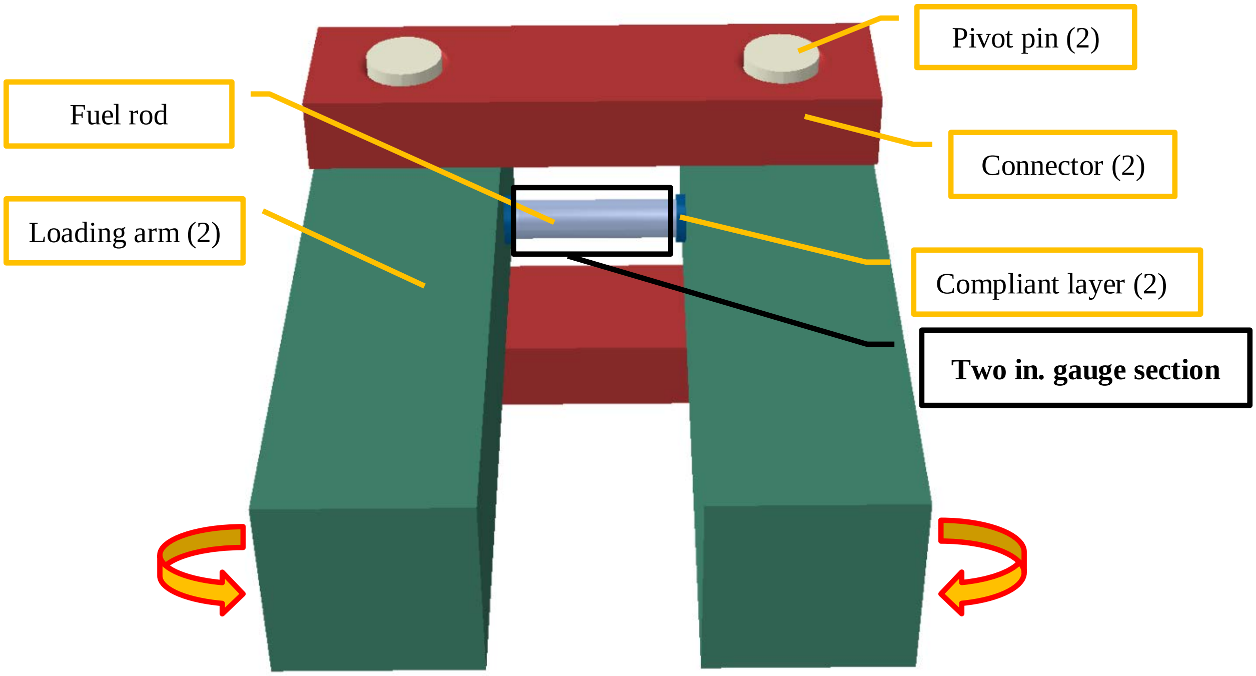

Fig. 48. Geometry of horizontal U-frame bending fatigue testing system with a coplanar rod configuration.

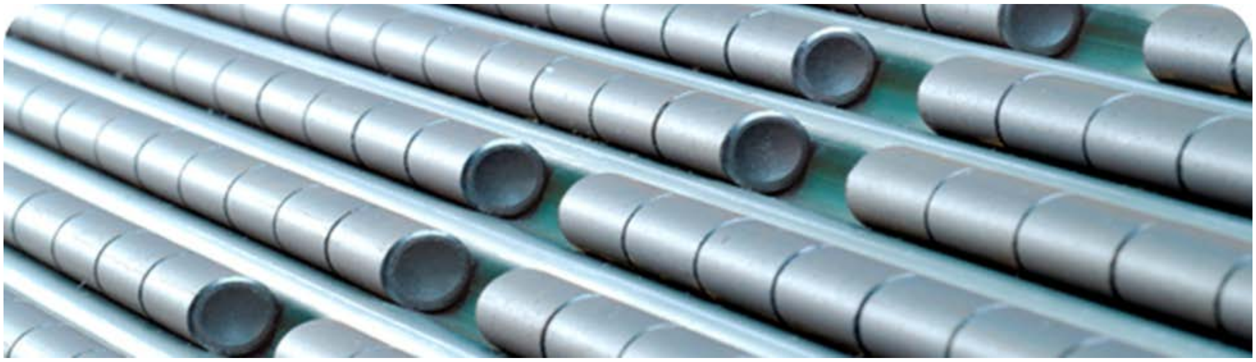

Fig. 49. Fuel pellets for nuclear reactors designed by AREVA Front End Business Group.

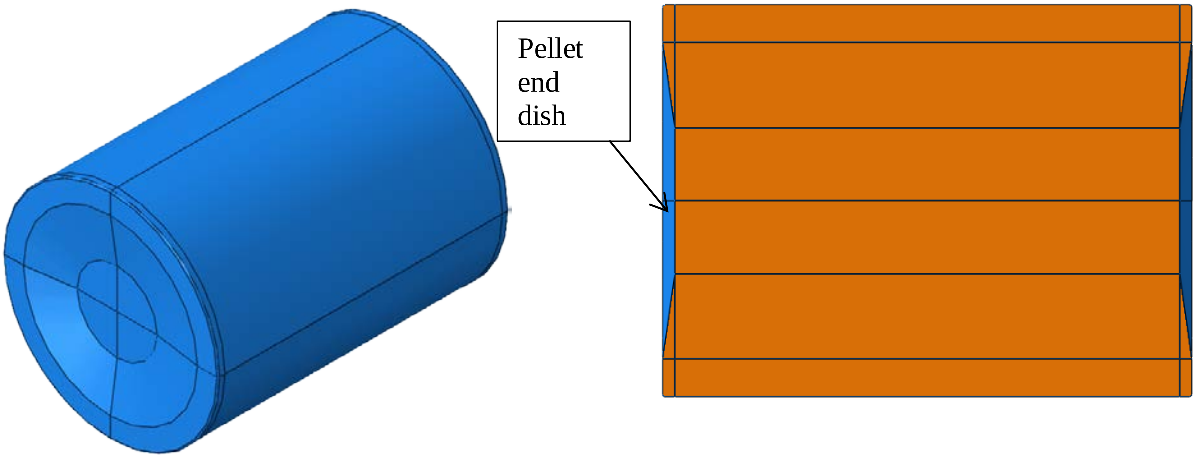

Fig. 50. FEA model of fuel pellet.

Fig. 51 illustrates the clad-epoxy-pellet section model with M5^{TM} cladding. The two in. gauge section consisted of four full-length and two partial-length pellets. The epoxy is 0.005 in. thick. To simulate "good interface bonding" at the pellet-pellet interface and an unfractured rod system, the pellet-pellet and pellet-clad interfaces were all tied. Bending moments were applied on both ends of the fuel rod rotating along the *X* axis as shown in Fig. 51 (b). To validate the FEA simulation against the hot-cell testing data, the bending moment *Mx* was the same as that used in the tests, 7.62 N·m (Sect. 4.7.3). Both loading surfaces of the fuel rod were constrained with rotation along the *Y* and *Z* axes and translation along the *X* direction. In the following finite element models, the global mesh is 0.02 in., and some local meshes are as small as 0.0025 in. The quasistatic procedure from ABAQUS is used in the FEA.

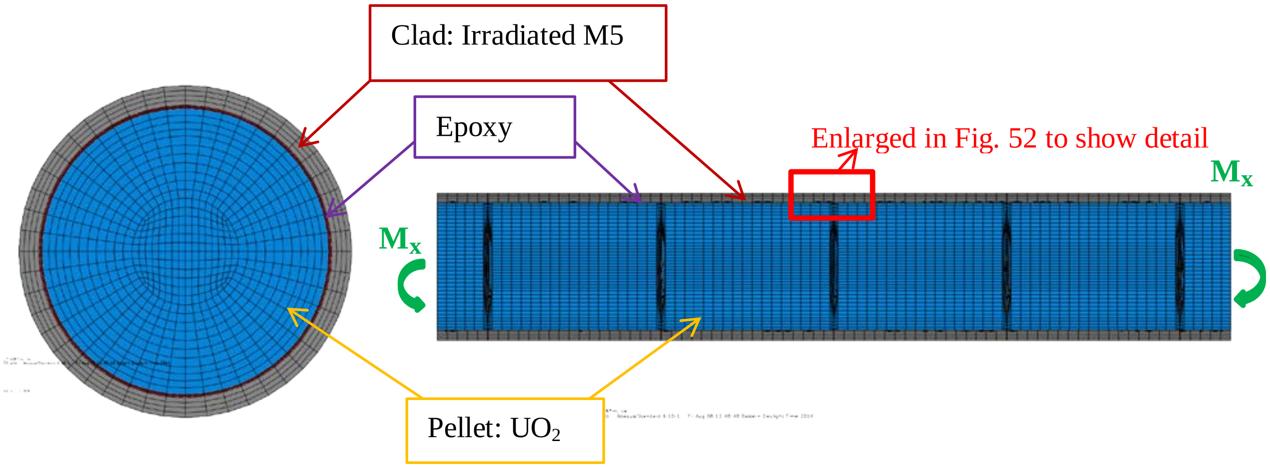

(a) Cross section view (b) Longitudinal section view

Fig. 51. Geometry of clad-epoxy-pellet two in. section model with six pellets and M5^{TM} clad.

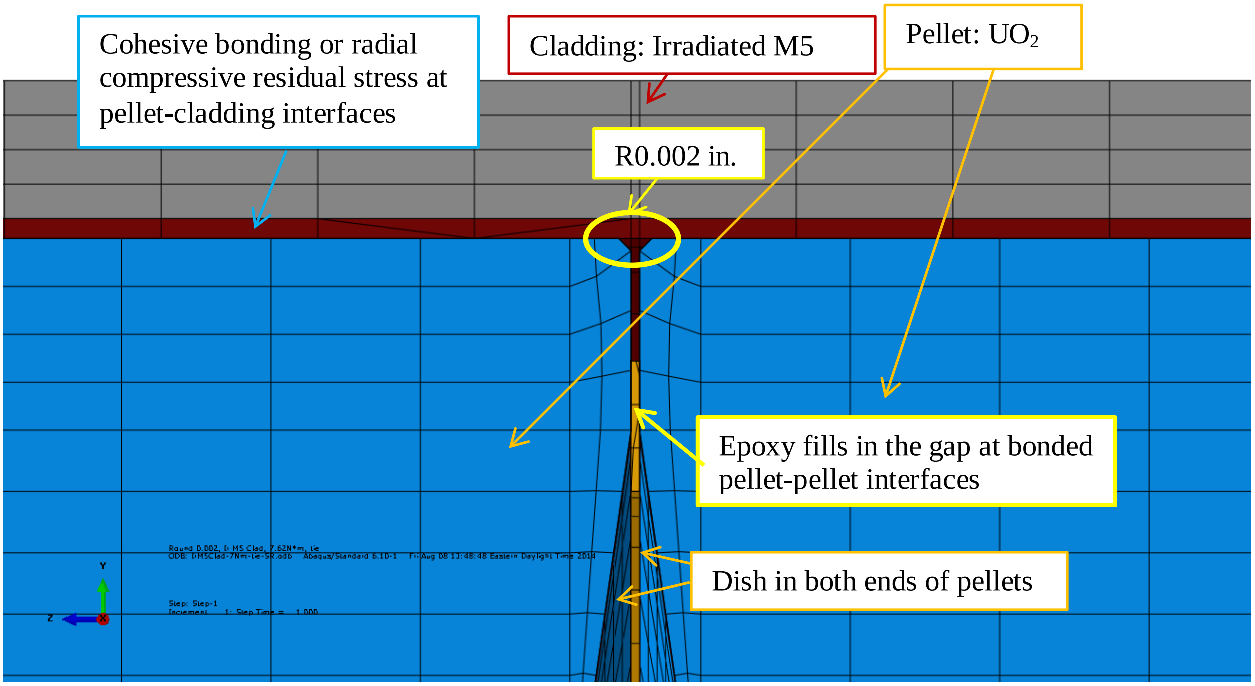

Fig. 52. Detail from Fig. 51 for the perfect bond case.

Fig. 52 shows the configuration of the detail area from Fig. 51. The pellets were modeled with a fillet of 0.002 in. radius on the end surfaces, and the end surfaces were dished at both ends to avoid pellet clinging. The dished areas of the pellet end surfaces do not come into contact during bending. To simulate cohesive bonding or radial compressive residual stress, thin epoxy layers are tied to the surfaces of the pellet-clad interfaces and the pellet-pellet interfaces. The epoxy layers at the pellet-pellet interfaces in the model are 0.0014 in. thick.

The resulting normal stress distribution and curvature under the bending moment 7.62 N·m are shown in Fig. 53. The resultant curvature is 0.173 m^{-1}, which is too small to be noticeable. Based on the stress distribution shown in Fig. 53 (a), the maximum stress occurs at the pellets, which indicates that the perfectly bonded pellets carry a larger portion of the moment resistance than the clad. From the detail view shown in Fig. 53 (b), the maximum stress is observed at the tie area at the pellet-pellet interface. The perfect bond assigned at the interface tie area is carrying most of the bending moment resistance. The stress in the clad is under the yield point of 98.5 ksi. Therefore, the clad has not yielded under the 7.62 N·m bending moment, nor have the pellets. This indicates that the fuel rod with a perfect bonding condition will remain within the linear elastic range under the target loading. The resultant σ_{zz} at the pellet-pellet interface in Fig. 53 (c) shows that the maximum stress is concentrated near the edge of the dish. This occurs because the dips in the ends of the pellets causes the contact surfaces to be confined to a limited area.

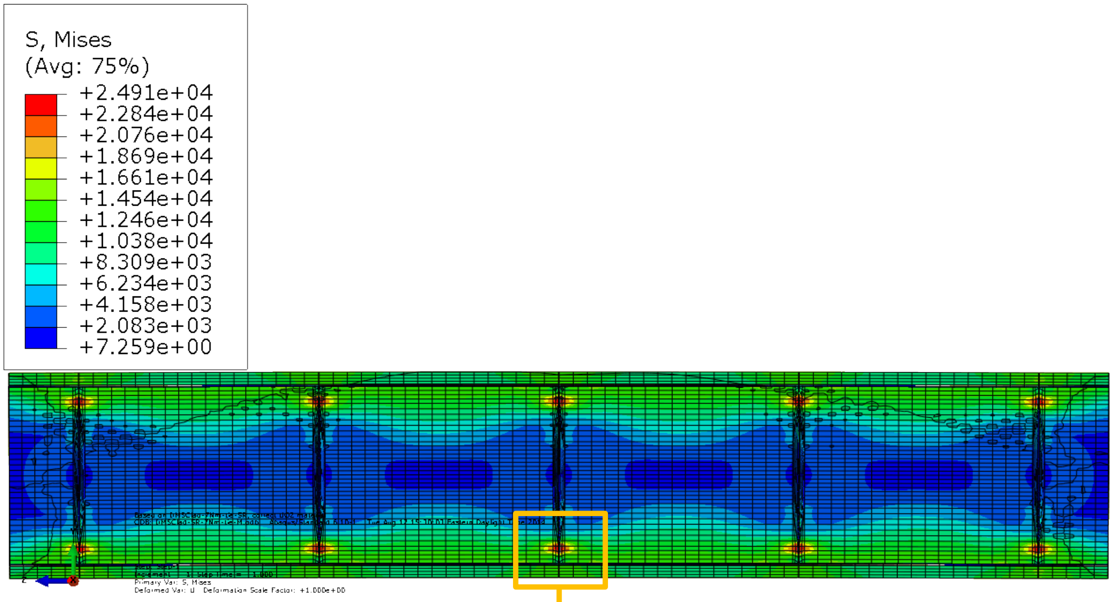

(a) Longitudinal section view of curvature and von Mises stress

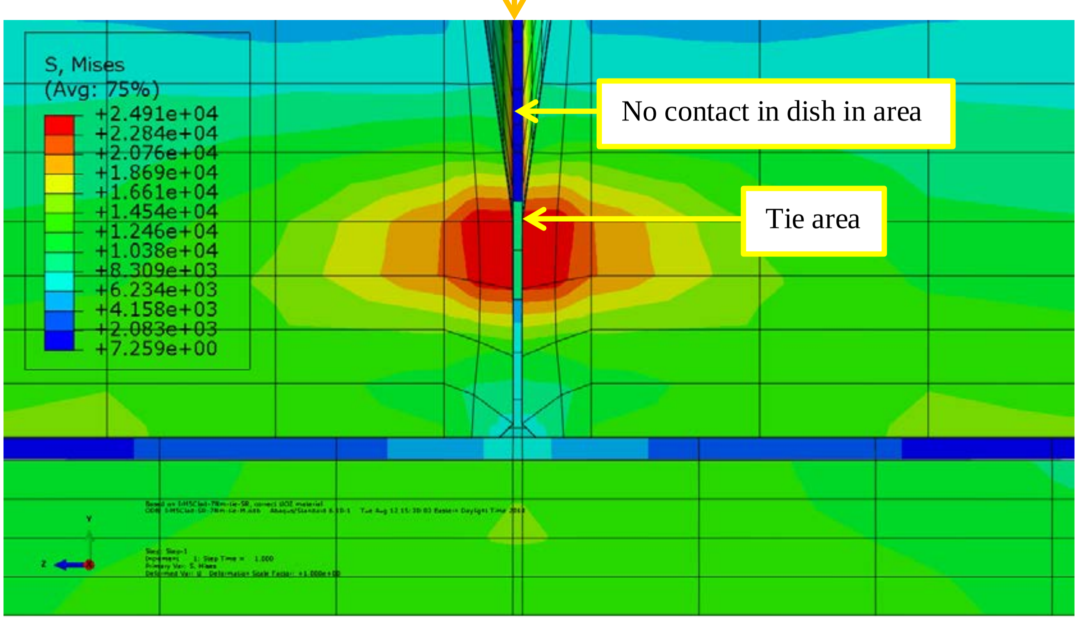

(b) Detail area view

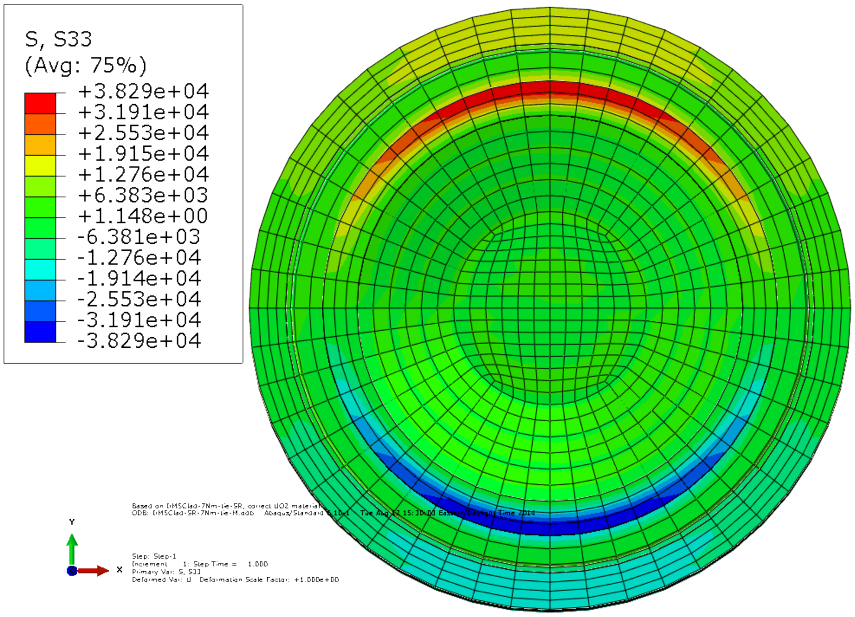

(c) Cross section view of σ_{zz} at a pellet-pellet interface

Fig. 53. Normal stress distribution and curvature results for clad-epoxy-pellet section model of M5^{TM} clad and six UO2 pellets with perfect bonding.

Figure 54 shows the shear stress distribution under the bending moment of 7.62 N·m in the cladding. Shear stresses in the cladding are minimal. As a result of the perfect bonding, the pellets and the cladding work as a whole. There is no significant shear stress concentration inside the gauge section. The stress concentration occurs at the boundary as a result of composite material mismatch under flexural deformation.

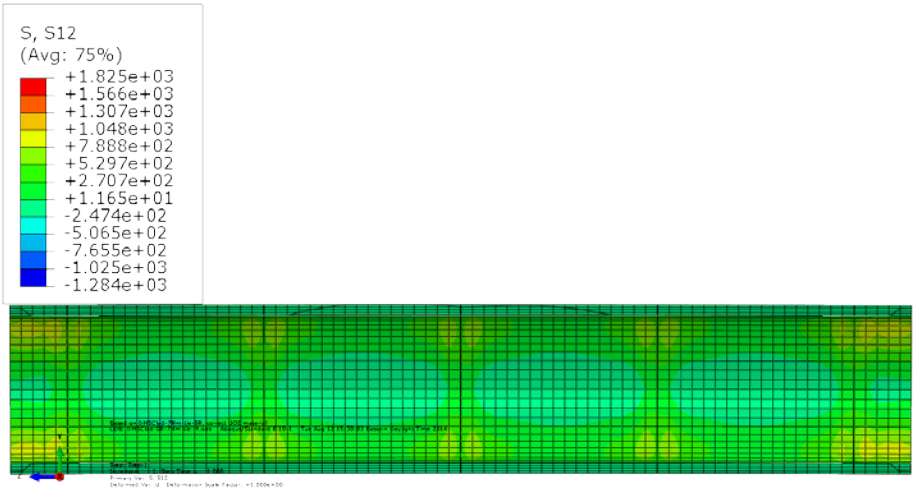

(a) Shear stress σ_{xy}

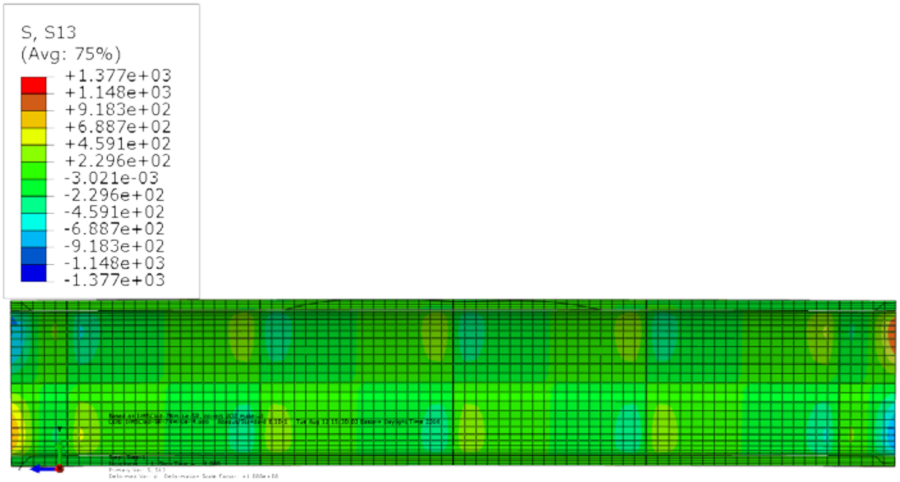

(b) Shear stress σ_{xz}

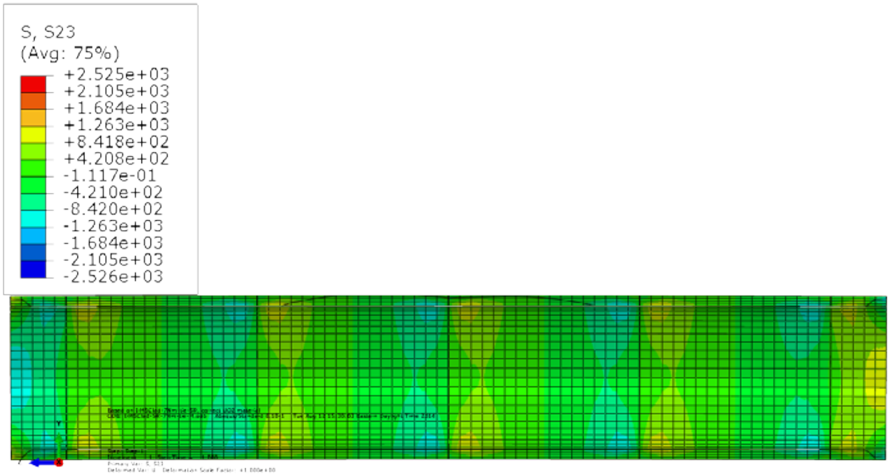

(c) Shear stress σ_{xz}

Fig. 54. Shear stress distribution in the clad for the clad-epoxy-pellet section model of M5^{TM}clad and six UO_2 pellets with perfect bonding.

In this section, the simulation case for the fuel rod of M5^{TM} clad was studied with good interface bonding and without inserted rod fracture. To simulate good cohesive bonding in the FEA, the pellet-clad interfaces were tied together with a thin epoxy layer.

The curvature and flexure rigidity for this case is summarized in Table 6. A load control procedure was used. The bending moment *M* was applied to both ends of the fuel rod, and the bending curvature κ was estimated from the FEA results within the gauge section. Furthermore, the flexural rigidity *EI* (the product of the Young's modulus *E* and the moment of inertia *I*) of a fuel rod can be estimated using the applied moment *M* and the resultant curvature κ as described in Eq. (7).

$$EI = M/\kappa \tag{7}$$

Based on the resulting σ_{zz}, as shown in Fig. 53(c), the bending moment was calculated for the cladding and pellets, respectively. The total resultant bending moment should be equal to the bending load M_{x}, 7.62 N·m. Estimated bending moments for the cladding and pellets are also summarized for a direct comparison of the load-carrying capacity of the different system components.

Table 6 shows that the flexure rigidity for a perfect bonding condition is 44 N·m^2 for the fuel rod of M5^{TM}. Based on the load-carrying capacity, the perfectly bonded pellets take over more of the bending moment than the cladding.

Table 6. The curvature, flexural rigidity, and bending moment comparison for the perfect interface bonding simulation

	Curvature κ(1/m)	Flexural rigidity *EI* (N·m^2)	Clad bending moment *M* (N·m)	Pellet bending moment *M* (N·m)
Perfect bond with epoxy	0.173	44	3.69	3.93

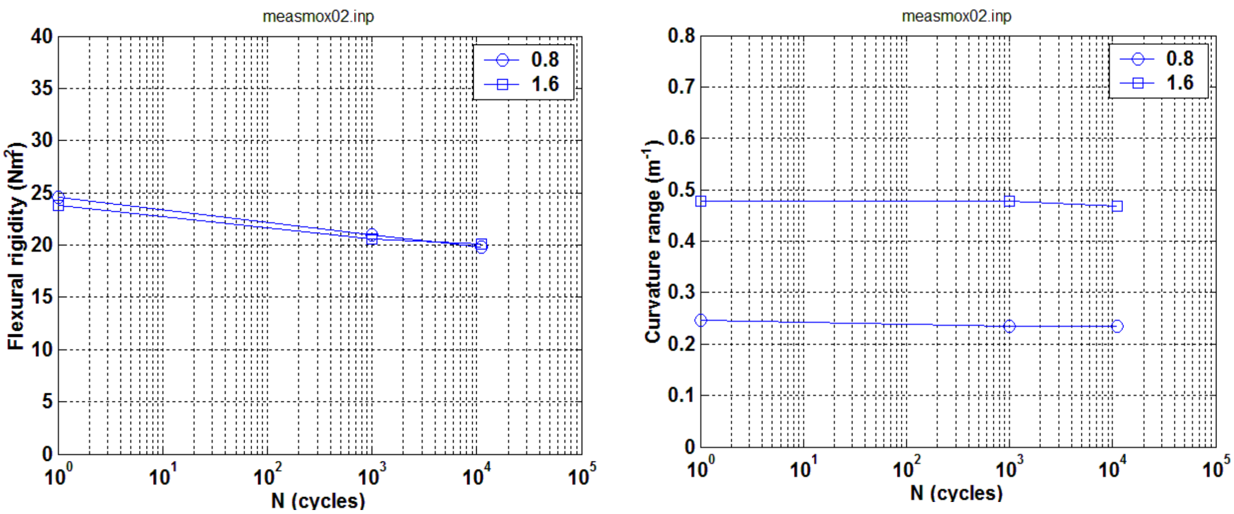

Fig. 55. ORNL hot-cell CIRFT MOX2 data, flexural rigidity, and curvature.

The condition of the ORNL M5^{TM} fuel rod hot-cell testing specimens resembles that of the clad-epoxy-pellet section model with epoxy-filled gaps at the pellet-pellet interfaces. The fuel specimen was tested under a 7.62 N·m bending moment. Figure 55 shows ORNL hot-cell CIRFT test data. The flexural rigidity based on the hot-cell test data was observed to be around 25 N·m^2, and the curvature was around 0.25 m^{-1}. The initial (first cycle) test data usually have the highest flexural rigidity since the pellet-clad and pellet-pellet interface bonds should maintain the best status before bending fatigue damage. The flexural rigidity in the first test data was a little lower than the FEA estimate, which indicates this testing sample probably has interfacial debonding rather than perfect bonding at the initial test stage.

With good interface bonding and without fuel rod fracture, the fuel rod can carry most of the bending moment under normal transportation vibration as a result of the higher Young's modulus of the fuel pellet compared with the clad as shown in Table 5. ORNL fuel data validate that inserted pellets can carry more moment resistance than the clad because of their higher stiffness when the pellet-clad and pellet-pellet interface bonds remain intact. Because of the high flexural strength of the fuel pellets, the fuel rod responds to the bending moment within the linear elastic range. The high flexural rigidity estimated from FEA agrees well with that estimated from bending fatigue testing data. Furthermore, under cyclic loading, it is expected that the interface bond will be progressively degraded as demonstrated in Fig. 55, with decreasing flexural rigidity under increased loading cycles.

5.2.2 Debonding at Pellet-Pellet Interfaces and Bonding at Pellet-Clad Interfaces

Before high-burnup UNF is transported, there are inherited stress fields in the UNF system. For example, there may be axial tensile stress and tangential tensile stress due to (1) pellet-clad mechanical interaction or oxide volume expansion, (2) radial compressive stress due to hydride compaction, and (3) tangential shear stress due to hydride volume expansion. Vibration during transportation will induce reversal bending in a UNF assembly. Repeated expansion and contraction in both the axial and tangential directions of the UNF rod due to reversal bending flexural deformation, combined with stress concentration, can degrade the interface bonding at the fuel pellet-clad and pellet-pellet interfaces (Fig. 56). Although the shear stress is small relative to the normal stress due to bending, that does not mean that it can be neglected. In composite rods or UNF rods, in particular, excessive shear due to material mismatch can be a cause of interfacial bonding failure.

At pellet-pellet interfaces, interfacial bonding failure is caused mostly by normal stress due to reversal bending flexural deformation combined with relatively smaller shear stress (see Fig. 56). At pellet-clad interfaces, localized high shear stress will also arise to compensate for the material mismatch under flexural deformation. As mentioned earlier, the shear stress is small relative to the normal stress; therefore, it is likely that interfacial bonding failure at pellet-pellet interfaces will begin before debonding occurs at pellet-clad interfaces. In addition, the fuel pellets have dished noncontact areas at both end surfaces, so the bonding area at the pellet-pellet interface is limited to a relatively small area, making it easier for the pellet-pellet interfaces to debond. Observations of an ORNL reversal bending fatigue fuel rod verified this hypothesis. In this section, the clad-epoxy-pellet section model with six pellets was used to investigate the fuel rod of M5^{TM} cladding bending response with perfect bonding at pellet-clad interfaces and debonding at pellet-pellet interfaces. The material properties, geometry, and loading and boundary conditions were the same as those used in the previous FEA simulation.

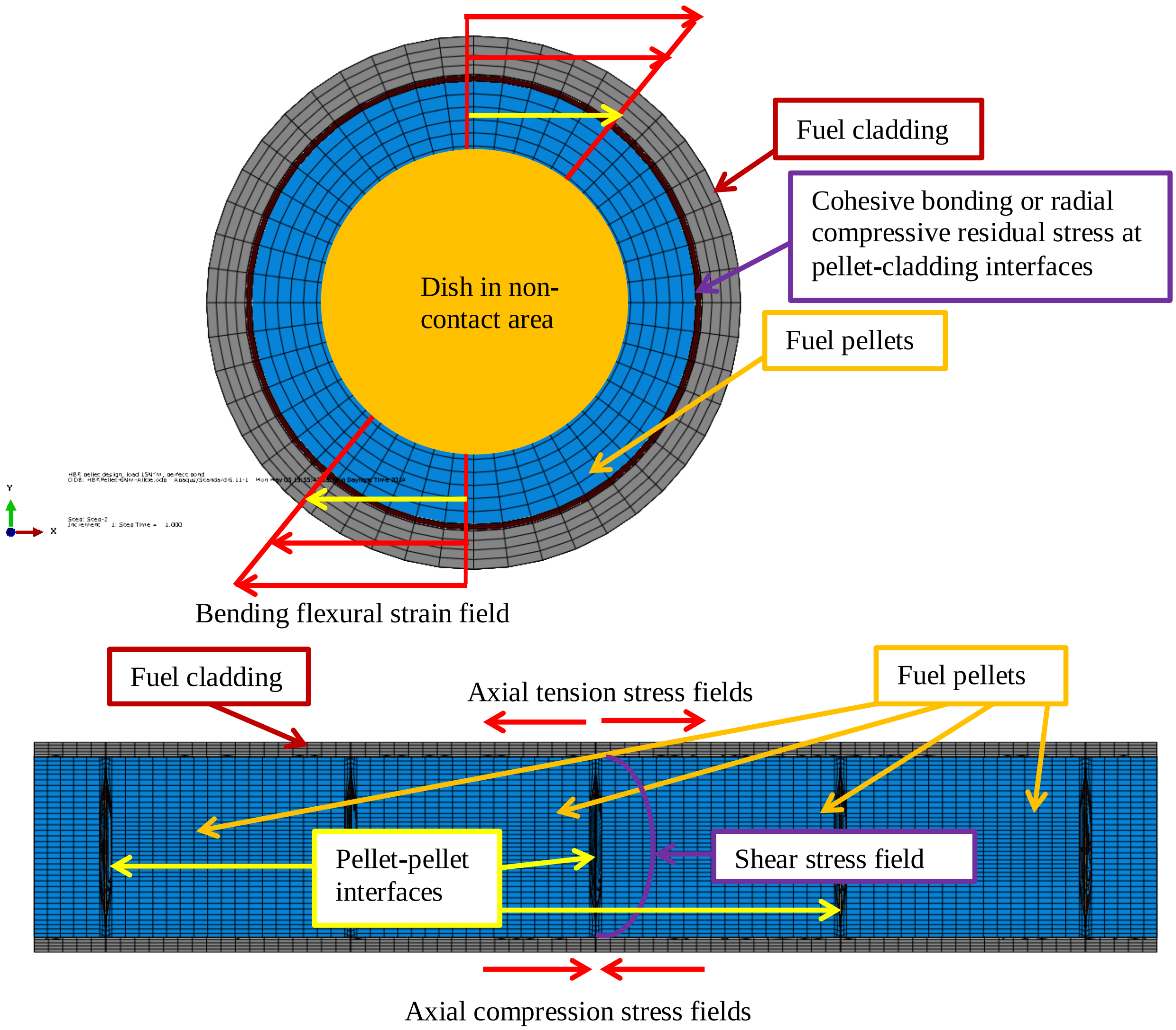

Fig. 56. Transportation-induced reversal bending stress fields in a UNF system.

5.2.2.1 Debonded Pellet-Pellet Interfaces with Empty Gaps

To simulate a good cohesive bond condition or radial compressive residual stress at pellet-clad interfaces, a thin bonding layer was tied to the surfaces at the pellet-clad interfaces. In this section, the case study was designed to simulate the response with a debonded pellet-pellet interface. There are empty gaps at the pellet-pellet interfaces (Fig. 57). During bending flexural deformation, the pellets overcome the gaps and then contact one another at the interfaces. The pellets have dish and end surfaces with a rounding of 0.002 in.

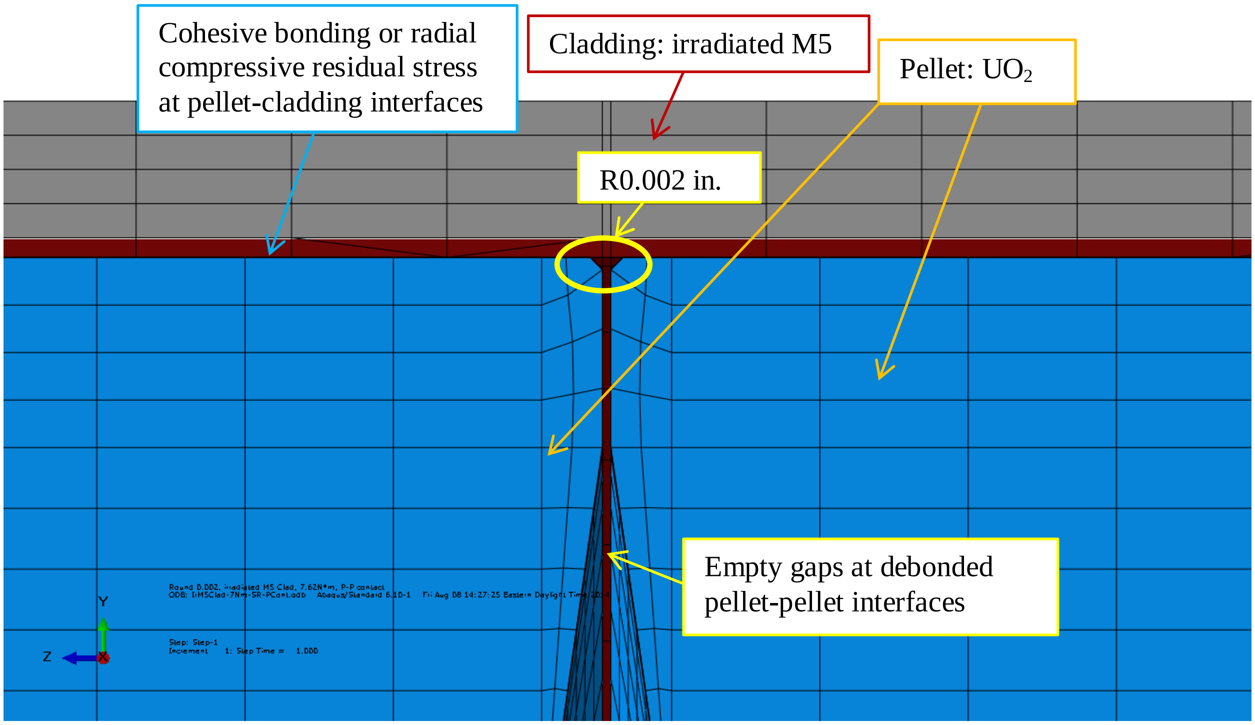

Fig. 57. Detail from Fig. 51 for the case of empty gaps at debonded pellet-pellet interfaces.

The normal stress and curvature responding to the bending moment are illustrated in Fig. 58 below. Compared with the results shown in Fig. 53, there are significant differences in the stress distribution between the pellet-pellet interface bonding case and the pellet-pellet interface debonding case; the pellet-clad interface remains perfectly bonded in both cases. For instance, at the pellet-pellet interface in the debonding case, the maximum stress occurs at the clad and is located at the top and bottom portions of the pellet-pellet interface regions. As a result of the small bending moment, the maximum stress at the clad is 10 times lower than the yield strength of M5^{TM} (see Table 5), so the M5^{TM} clad does not yield. In most of the clad, the stress is much lower than the maximum because the perfect pellet-clad bonding provides good support to the clad. Since there are gaps between pellet-pellet interfaces, the clad deforms continuously until the gaps are reduced by direct contact of the pellet-pellet surfaces. However, no stress concentration is observed at the pellet-pellet contact corners. The resulting σ_{zz} clearly indicates that the clad takes over more of the bending moment resistance than the pellets at the debonded pellet-pellet interfaces.

At the debonded pellet-pellet interfaces, the pellets can transfer load only via hard contact, so the load-carrying capacity shifts significantly from the pellets to the clad. When the M5^{TM} clad starts to carry most of the bending moment at the pellet-pellet interface region, the result is maximum stress concentration at the M5^{TM} clad. However, in most of the gauge section, the pellets still provide sufficient internal support to the clad because of good cohesive bonding at the pellet-clad interfaces, and they will carry most of the bending load. Therefore, there is much lower stress in most regions of the M5^{TM} clad.

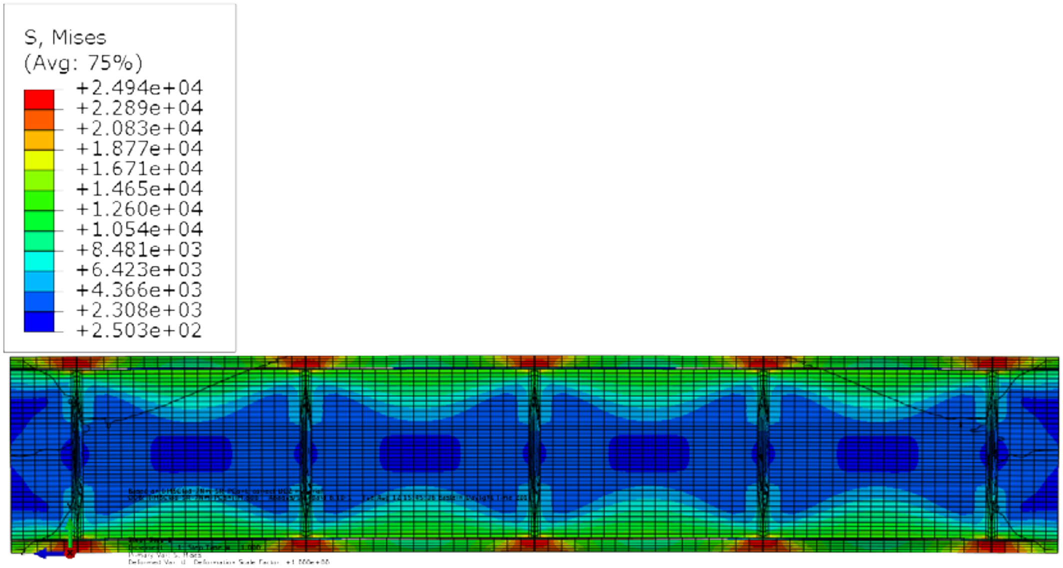

(a) Longitudinal section view of resultant curvature and von Mises stress

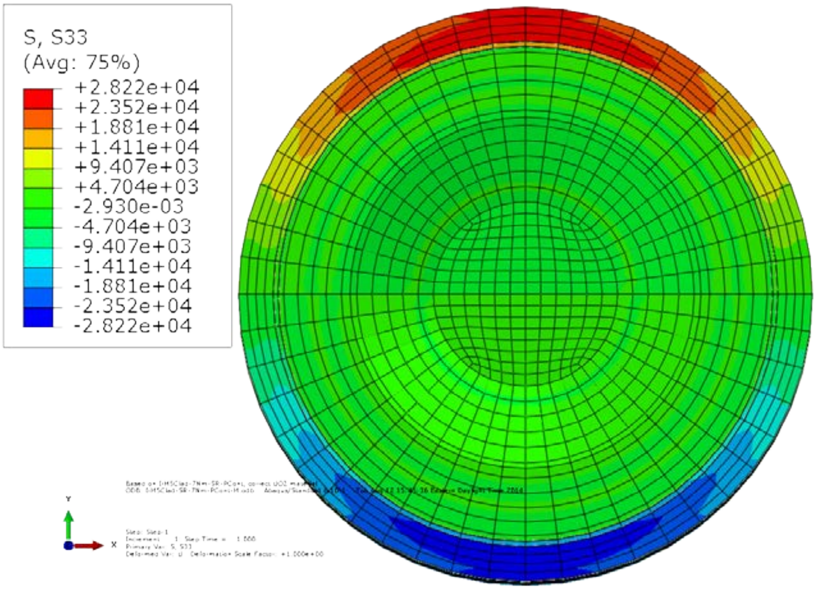

(b) Cross section view of resultant σ_{zz} at a pellet-pellet interface

Fig. 58. Normal stress distribution and curvature results for clad-epoxy-pellet section model of M5^{TM} clad and six UO_2 pellets with debonded pellet-pellet interfaces with gaps and bonded pellet-clad interfaces.

In Fig. 53, the results of the perfect bond case show that the pellets carry sufficient bending moment resistance; the maximum stress resides on the pellets, and there is no yielding or failure at either the pellets or the clad. In Fig. 53, a dog-bone shape appears inside the pellet as a result of von Mises stress distribution; a similar dog-bone shape inside the pellets is shown in Fig. 58. In the debonding case, the curvature is 0.24 m^{-1}, which is 1.4 times that of the perfect bond case shown in Fig. 53.

In Fig. 59, the difference from the results in Fig. 54 for the perfect bond case is apparent. With the pellet-pellet interfaces debonded, the shear stresses surge near the pellet-pellet interface debonding region inside the cladding. The reason might be an increase in shear stress due to a composite material mismatch at the debonded pellet-pellet interface boundary under bending flexural deformation. With good cohesive bonding at pellet-clad interfaces, the clad transfers some shear load at the debonding region. If there are small gaps at the pellet-pellet interfaces, the shear stress concentration occurs at both the top tension and bottom compression regions of the clad. Maximum stress levels are higher than in perfect bond cases; however, the shear stresses are still one order of magnitude lower than the normal stress in the same simulation case.

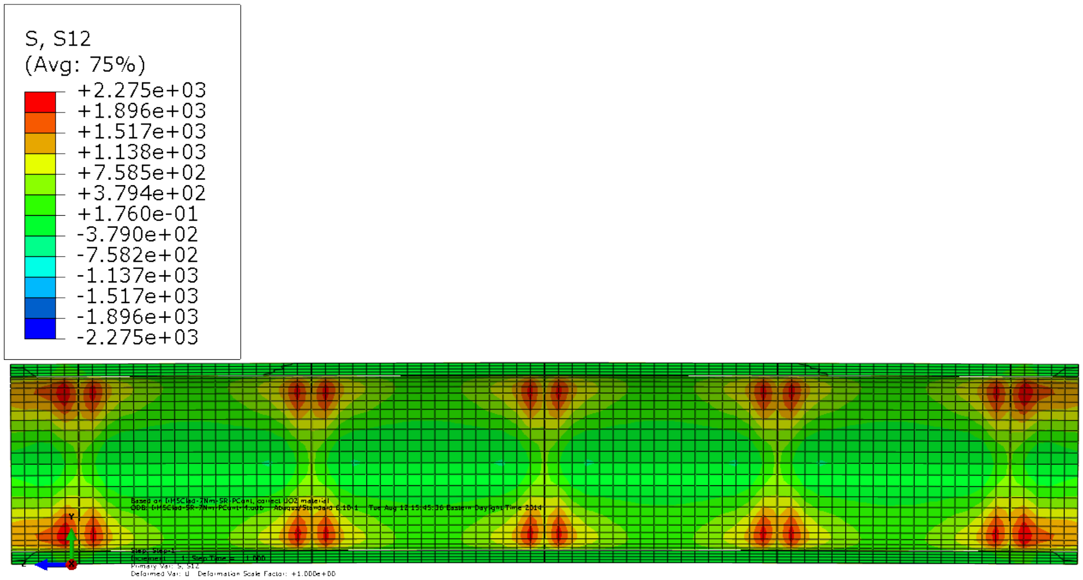

(a) Shear stress σ_{xy}

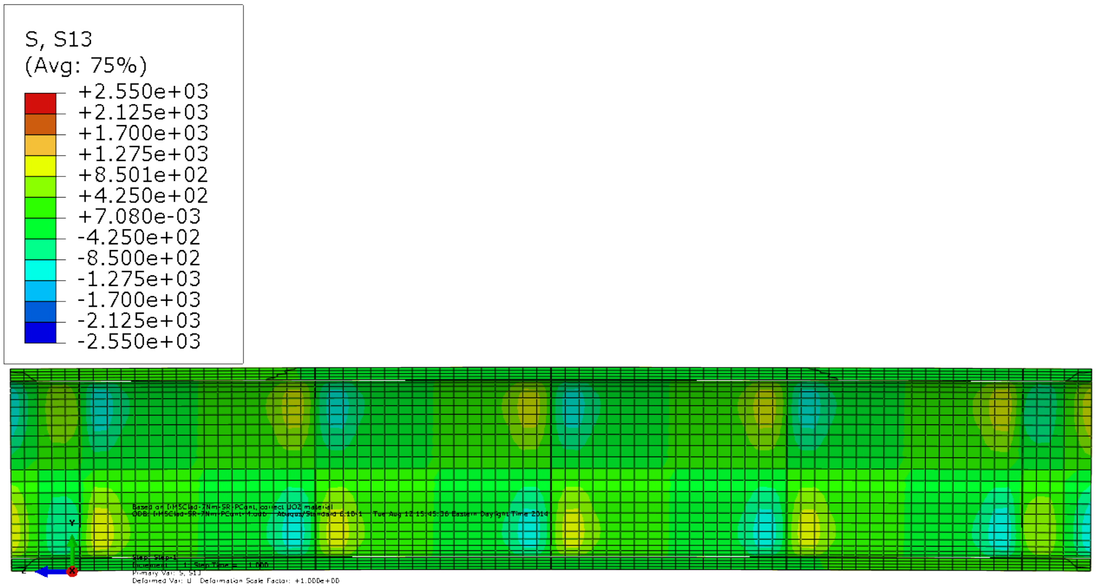

(b) Shear stress σ_{xz}

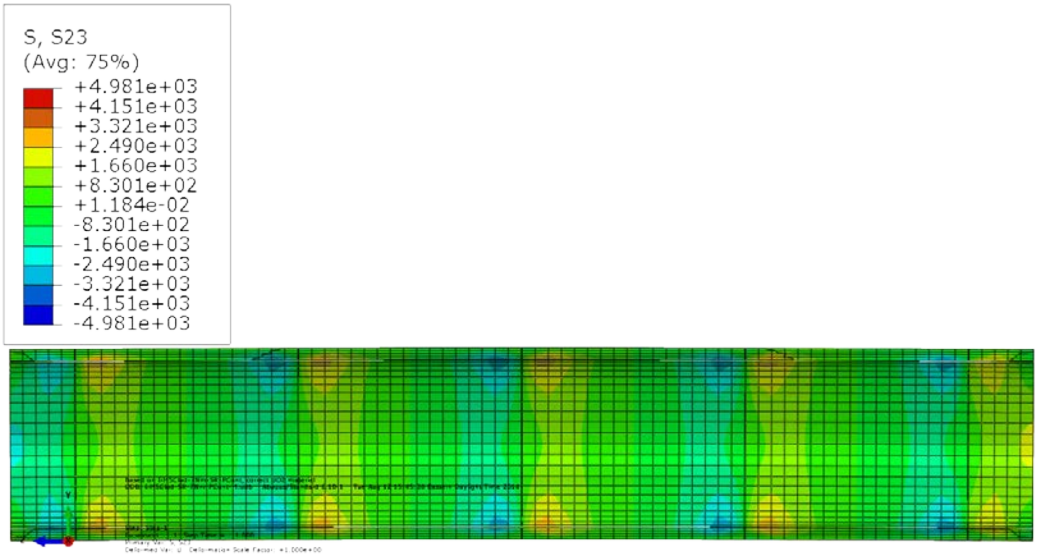

(c) Shear stress σ_{yz}

Fig. 59. Shear stress distribution at the clad of the clad-epoxy-pellet section model of M5^{TM} clad and six UO_2 pellets with debonded pellet-pellet interfaces with gaps and bonded pellet-clad interfaces.

5.2.2.2 Debonded Pellet-Pellet Interfaces without Gaps

Fig. 60 illustrates the simulations of "debond pellet-pellet interface" and "bond pellet-clad interface." There are no gaps at the pellet-pellet interfaces before bending loading is applied. Similar to the previous cases, a thin layer of epoxy is applied and tied to the surfaces at the pellet-clad interfaces to simulate good cohesive bonding or radial compressive residual stress. Except for elimination of the gaps at the pellet-pellet interfaces, the geometry, materials, and loading and boundary conditions are all the same as in the previous simulations.

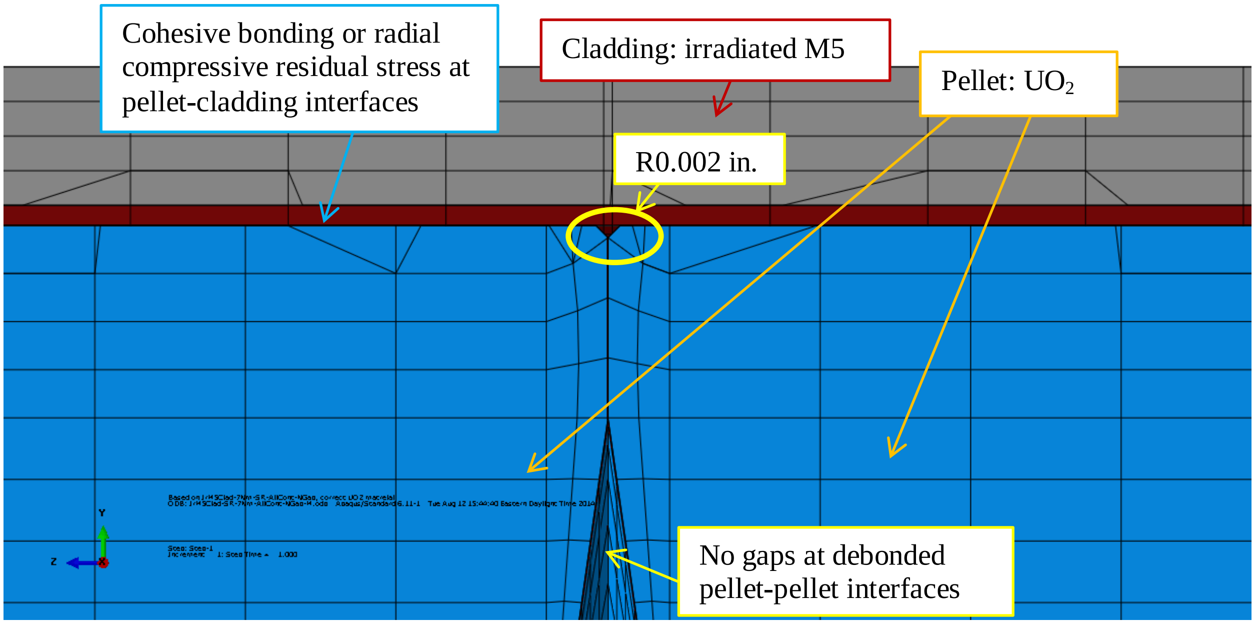

Fig. 60. Detail from Fig. 51 for the case of no gaps at debonded pellet-pellet interfaces.

As illustrated in Fig. 61, the normal stress distribution of this case appears to be different from that of debonded pellet-pellet interface case with empty gaps in Fig. 58. The maximum stress occurs at the top of the clad at pellet-pellet interface regions; however, at the compression side, interface stress concentrations occur at the pellets instead of at the clad. This is because there are no gaps at the pellet-pellet-clad interface region. Thus the contact pellets provide good internal support to the clad tubing structure. Furthermore, the pellets seem to carry a significant portion of the bending moment resistance via pellet-pellet interaction (pinching at pellet corners), which significantly mitigates the stress level of the clad at the bottom (compression) region. The clad shows asymmetric stress distribution between the tension and compression sides at the debonded pellet-pellet interfaces. Because of the high yield strength of the pellet and clad materials, as well as the small bending load, the pellets and the clad are all under the linear elastic range at the maximum stress level. The resultant σ_{zz} profile without gaps at the pellet-pellet interface indicates that the pellets can carry more bending moment resistance than the pellets with gaps shown in Fig. 58.

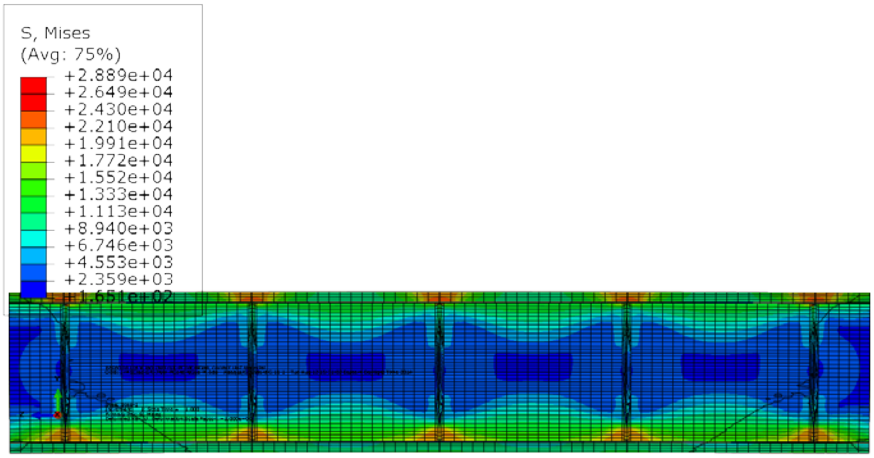

(a) Longitudinal section view of resultant curvature and von Mises stress

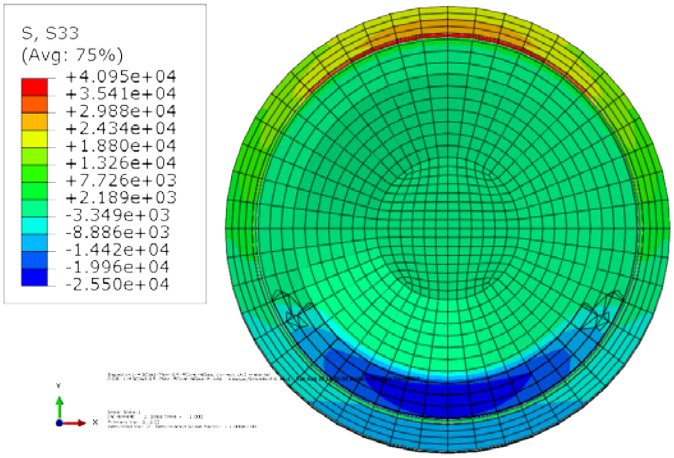

(b) Cross section view of σ_{zz} at a pellet-pellet interface

Fig. 61. Normal stress distribution and curvature results for clad-epoxy-pellet section model of M5^{TM} clad and six UO_2 pellets with debonded pellet-pellet interfaces without gaps and bonded pellet-clad interfaces.

Figure 62 shows the shear stress distribution at the clad for this case. The shear stress concentration occurs only at the top tension side, unlike the case for pellet-pellet interface debonding with small gaps. The maximum stress concentration level is close to the results shown in Fig. 59. At the bottom compression side, the shear stress level is low. The reason is the same as for the normal stress results: when the gaps are eliminated, pellet-to-pellet direct pinning helps lower the stress on the clad at the bottom region.

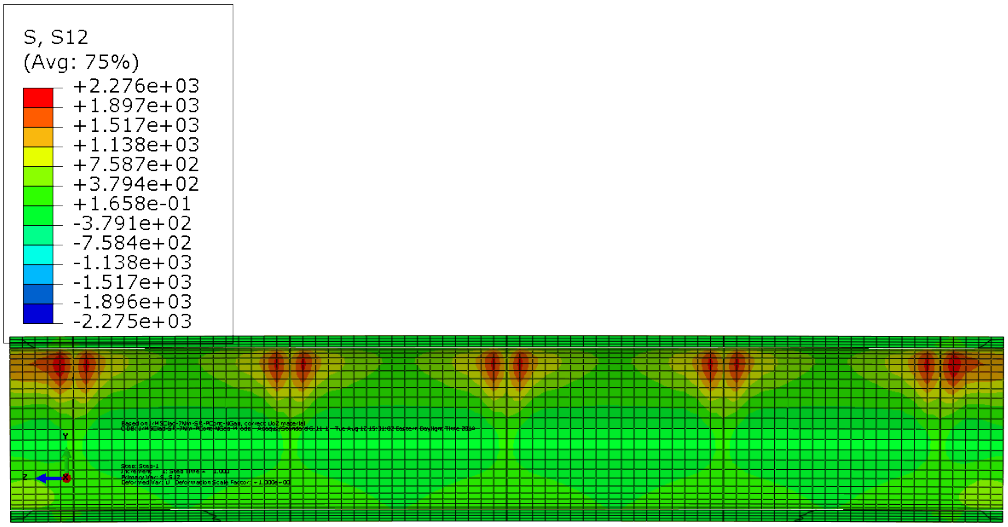

(a) Shear stress σ_{xy}

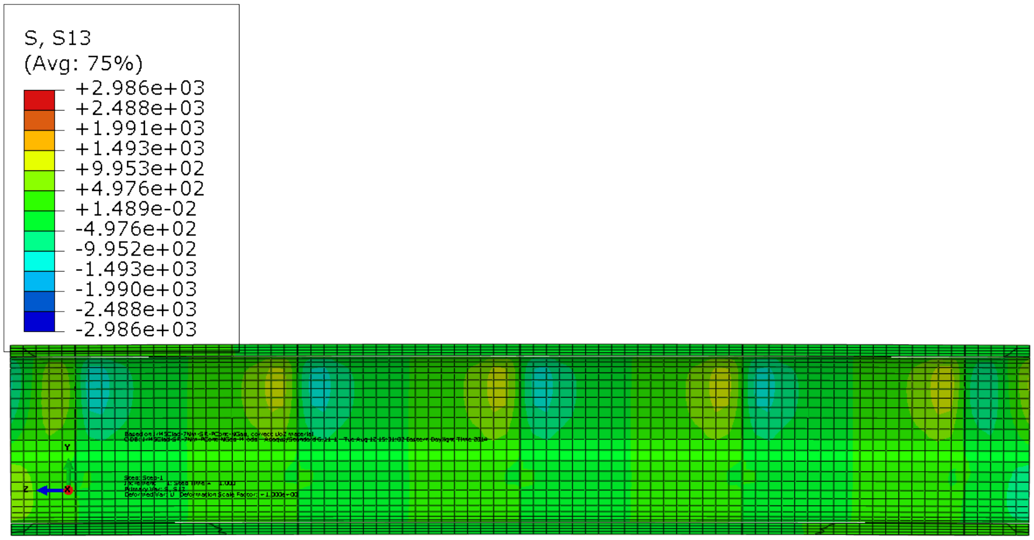

(b) Shear stress σ_{xz}

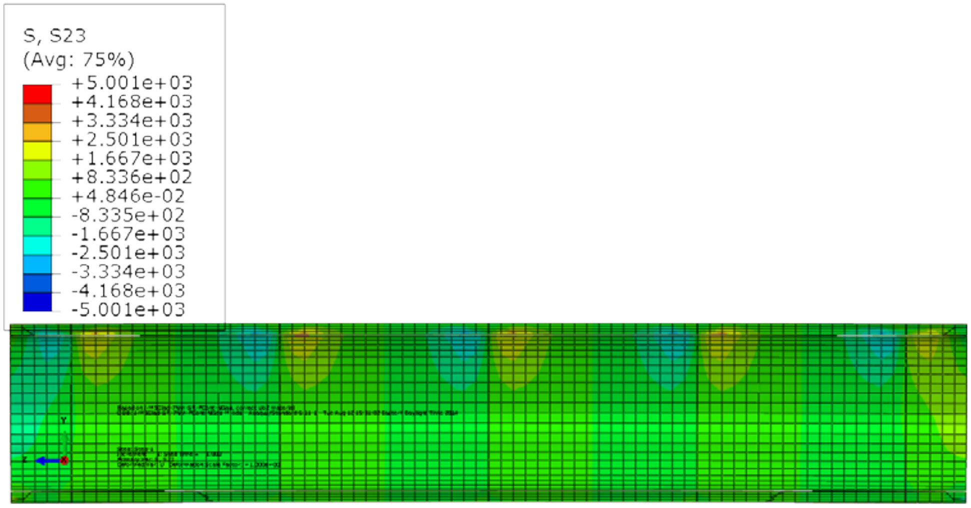

(c) Shear stress σ_{yz}

Fig. 62. Shear stress distribution at the clad of the clad-epoxy-pellet section of M5^{TM} model of six UO$_2$ pellets with debonded pellet-pellet interfaces without gaps and bonded pellet-clad interfaces.

Table 7 summarizes the estimate curvature, flexural rigidity, and components’ loading-carrying capacity from two FEA simulation cases discussed in this section. The same bending load (7.62 N·m) was used in all of the FEA simulations. The curvature and the flexural rigidity listed in Table 7 indicate that for interface bonding simulation, the immediate consequence of debonding at the pellet-pellet interface is a significant increase in curvature, which results in a significant reduction in the estimated flexural rigidity. This phenomenon is primarily due to a shift in the load-carrying capacity from the pellets to the clad.

Table 7. Comparison of curvature, flexural rigidity and bending moment for the bonded pellet-clad and debonded pellet-pellet cases

	Curvature κ(1/m)	**Flexural rigidity *EI* (N·m^2)**	**Clad bending moment *M* (N·m)**	**Pellet bending moment *M* (N·m)**
Pellet-pellet interface with gap debonding; pellet-clad interface bonded	0.24	32	6.35	1.27
Pellet-pellet interface without gap debonding, pellet-clad interface bonded	0.192	40	4.39	3.23

The induced curvature of 0.24 m^{-1} for debonded pellet-pellet interfaces with gaps and a pellet-clad interface bonded with epoxy is 1.4 times the curvature value of 0.173 m^{-1} for the case of perfect bonding. The estimated flexural rigidity of 32 N·m^2 for the case of a debonded pellet-pellet interface is a reduction of about 27% compared with of 44 N·m^2 for perfect interfacial bonding. Gaps at the pellet-pellet interfaces play a critical role in estimating the flexural rigidity of fuel rod with M5^{TM} cladding. The induced curvature of 0.24 m^{-1} for the debonded pellet-pellet interfaces with empty gaps is 1.25 times that of the debonded pellet-pellet interfaces without gaps. The result is a 20% reduction in flexural rigidity from 40 N·m^2 for the case with no gaps to 32 N·m^2 for the case with empty gaps. In Table 6, the perfectly bonded pellets carry more bending moment than the clad. In Table 7, the data clearly show a significant shift in bending moment resistance from the pellets to the clad as a result of debonding at pellet-pellet interfaces. For two simulation cases discussed in this section, the clad takes more of the bending moment than the pellets. When the pellets directly contact one another without gaps, the bending moment on the clad drops by around 30% compared with the pellets with empty gaps.

These results indicate that the gap-induced stress concentration and large deformations of the clad at the pellet-pellet interface region can lead to a significant reduction in the bending stiffness, i.e., flexural rigidity (*EI*), of the fuel rod system. If there are no gaps at the pellet-pellet interfaces, the pellets can carry a significant portion of the bending moment resistance via direct pellet-pellet contact (interaction) to mitigate the stress concentration and potential yielding at the clad.

5.2.3 Debonded Pellet-Clad and Pellet-Pellet Interfaces

Under flexural deformation, high shear stress will arise at the pellet-clad interfaces to compensate for the material mismatch and the flexural shear stress in the UNF system. Thus under reversal bending loading during normal transportation, both cyclic normal stress and shear stress can further degrade the interface bonding at pellet-clad interfaces. In this section, debonded pellet-clad interfaces and debonded pellet-pellet interfaces are investigated using the clad-epoxy-pellet section model with six UO_2 pellets and M5^{TM} cladding.

5.2.3.1 Debonded Pellet-Clad Interfaces and Debonded Pellet-Pellet Interfaces with Empty Gaps

As illustrated in Fig. 63, simulations of interfacial debonding at both pellet-clad and pellet-pellet interfaces first focus on the case with empty gaps at debonded pellet-pellet interfaces and a thin layer at debonded pellet-clad interfaces. At pellet-clad interfaces, the outer pellet surfaces contact the inner surface of the thin layer, and the outer surface of the thin layer contacts the inner surface of the clad. Pellets have dish surfaces at both ends with rounding of 0.002 inches A fuel rod consisting of M5^{TM} clad and UO_2 pellet inserts is used to study the system response to bending moment with debonded interfaces. Loading and boundary conditions are the same as those assumed in the previous cases, and bending moment is assigned at 7.62 N·m.

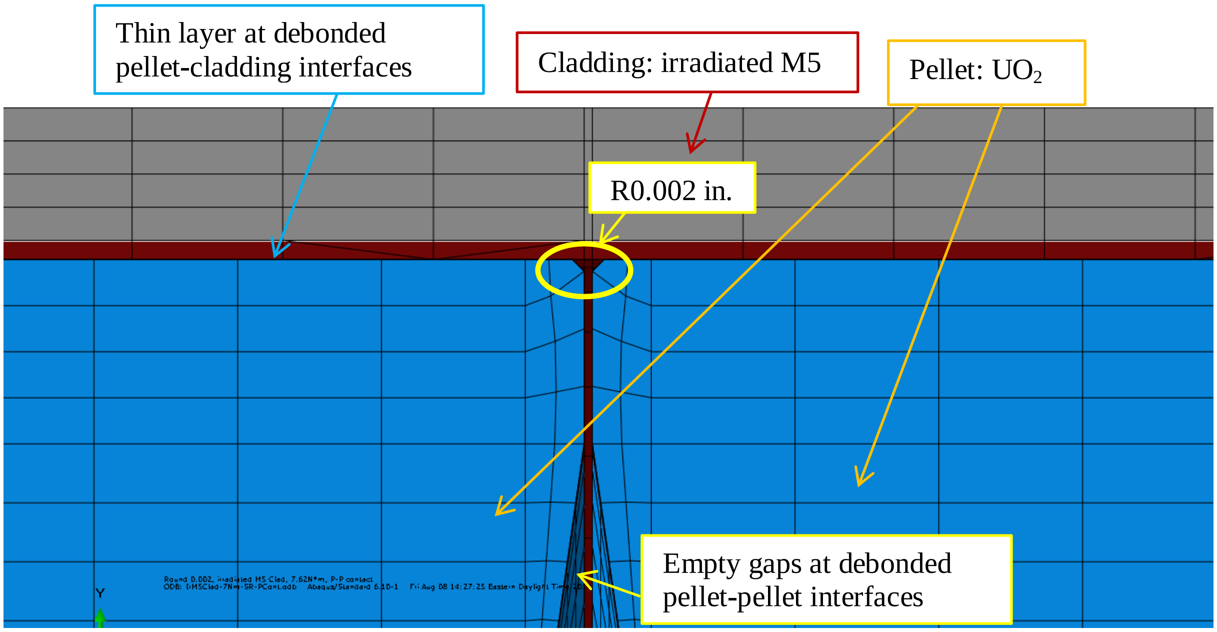

Fig. 63. Detail area from Fig. 51 for the cases of empty gaps at debonded pellet-pellet interfaces, and a thin layer filled at the debonded pellet-clad interfaces.

The resulting normal stress distribution shown in Fig. 64 indicates that the clad reached maximum stress throughout the whole gauge section when interfacial debonding occurred at both pellet-clad and pellet-pellet interfaces. This result is a strong contrast to the results in Fig. 58, where the M5^{TM} clad shows stress concentrations only locally at pellet-pellet interface regions. Because of the small bending load and high material yield strength, the clad did not yield at the maximum stress. The pellets were all below the yielding stress, as well. The induced curvature of 0.462 m^{-1} is almost triple that of the perfect bond case. This suggests that, as a result of the interface debonding at both the pellet-clad and pellet-pellet interfaces, the pellets and the clad can contact (or pin) only at the pellet-pellet-clad interface region, and pellets cannot provide direct internal support to the clad. Therefore, the load-carrying capacity shifts significantly from pellets to the clad at the entire gauge section. The results also indicate that the M5^{TM} clad carries most of the bending moment resistance. The bending deformation in the debonded pellet-clad region is likely to result in further pinning action at pellet-clad interfaces, which may also result in accelerated aging of the clad tubing.

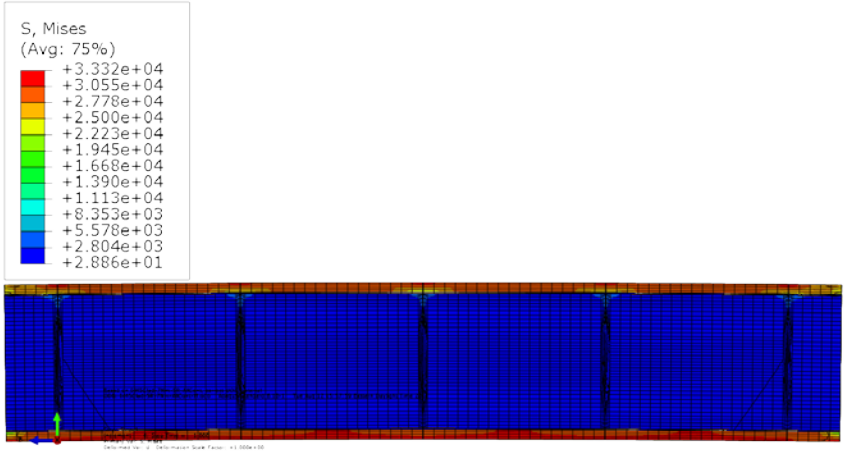

(a) Longitudinal section view of resultant curvature and von Mises stress

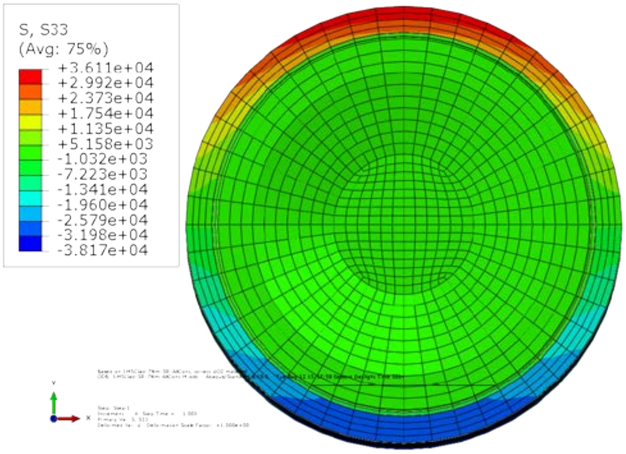

(b) Cross section view of σ_{zz} at a pellet-pellet interface

Fig. 64. Normal stress distribution and curvature results for clad-epoxy-pellet section model of M5^{TM} clad, where six UO2 pellet with empty gaps at debonded pellet-pellet interfaces and an epoxy layer at debonded pellet-clad interfaces.

Figure 65 illustrates the shear stress results for this simulation case. The stress pattern appears to be different compared to the perfect bond case or only pellet-pellet interface debonded case. In particular, the apparent stress concentrations are located near the neutral axis for the shear stress σ_{yz}.

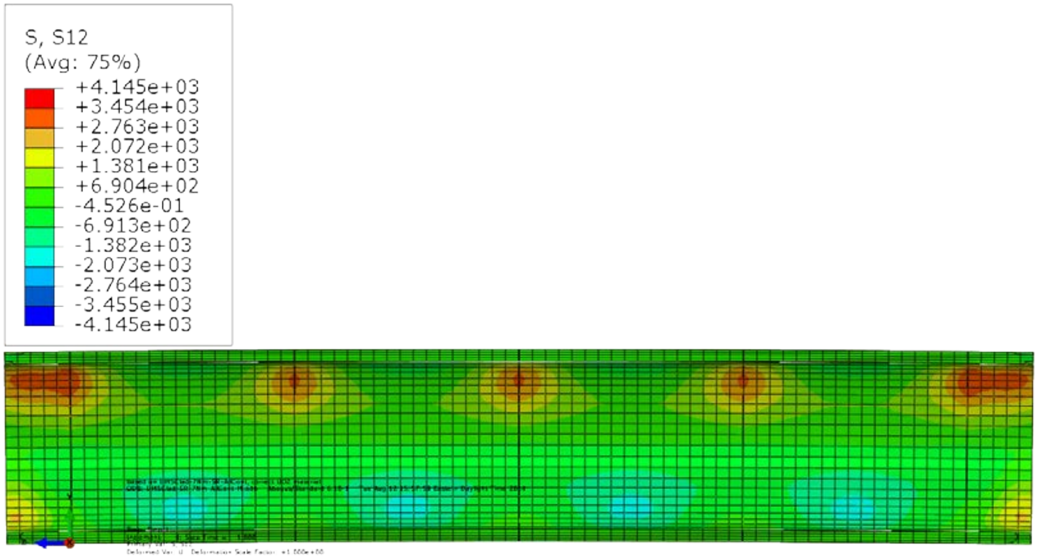

(a) Shear stress σ_{xy}

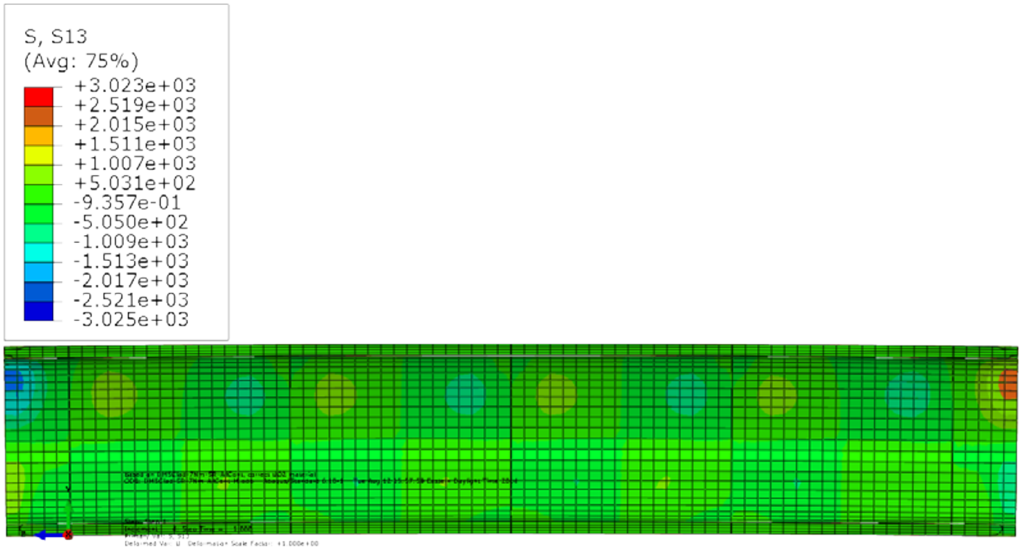

(b) Shear stress σ_{xz}

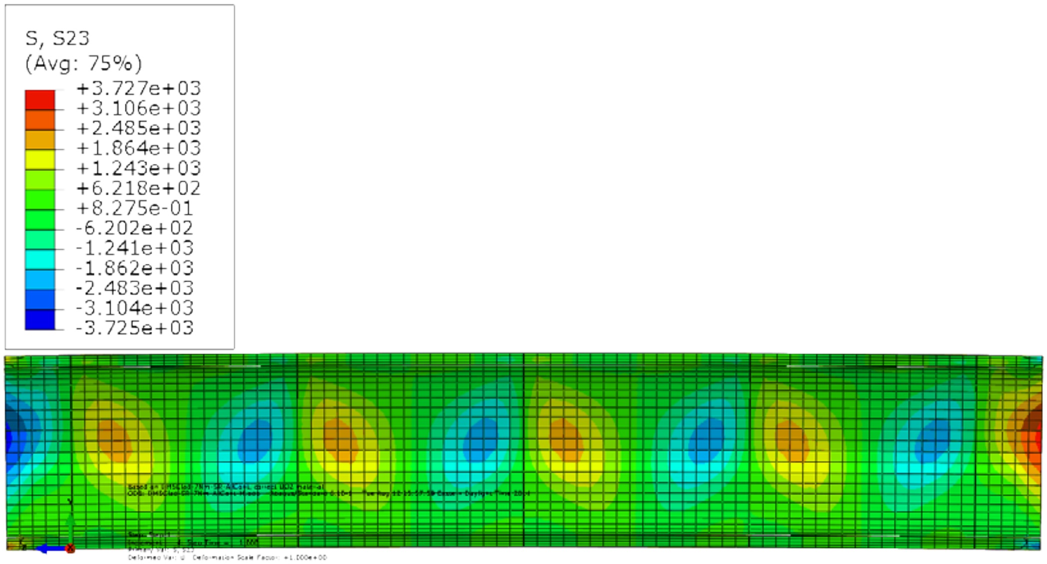

(c) Shear stress σ_{yz}

Fig. 65. Shear stress distribution at the clad of the clad-epoxy-pellet section for M5^{TM} model, where six UO_2 pellet with empty gaps at debonded pellet-pellet interfaces and an epoxy layer at debonded pellet-clad interfaces.

5.2.3.2 Debonded Pellet-Clad Interfaces and Debonded Pellet-Pellet Interfaces without Gaps

The simulation cases for debonded pellet-pellet interfaces without gaps are shown in Fig. 66, where a thin layer of epoxy is filled at debonded pellet-clad interfaces, and the pellets are all in direct contact with one another without gaps at the pellet-pellet interfaces. The loading and boundary conditions and the material properties are the same as in the previous cases. In this case, there are still six pellets with rounding of 0.002 in.

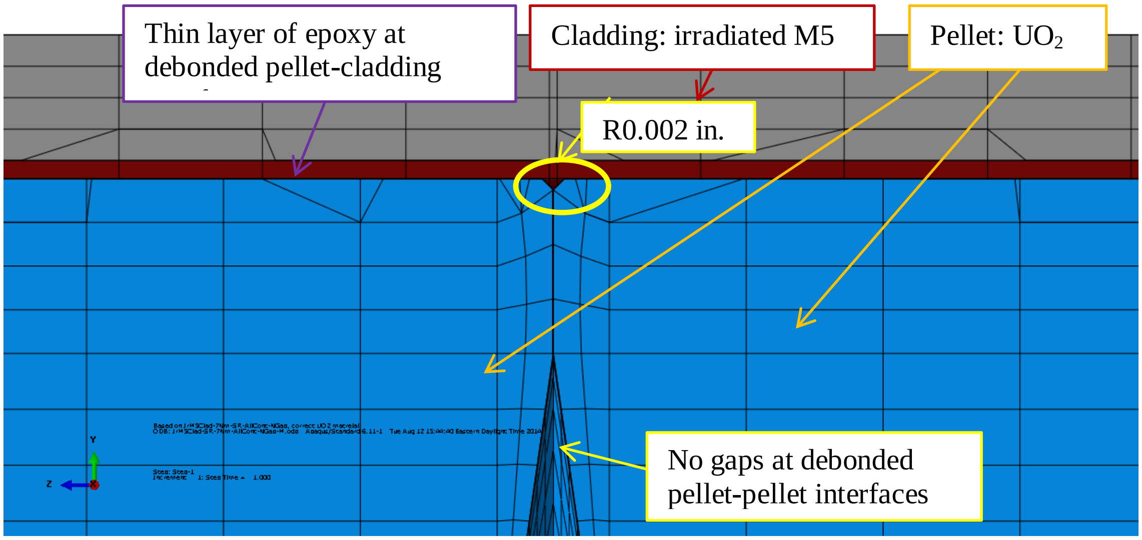

Fig. 66. Detail area from Fig. 51 for the case with no gaps at debonded pellet-pellet interfaces and a thin layer at debonded pellet-clad interfaces.

Figure 67 illustrates the fuel rod with M5^{TM} cladding responses to the bending moment in this simulation. The longitudinal section view shows a stress concentration at the top (tension) region of the M5^{TM} clad throughout the gauge section, but the rod did not yield. In the bottom (compression) region, the stress level is low at the clad. The maximum stress still occurred at the compression side of the pellet region where the pellets were pinned to one another. Figure 67 shows asymmetric stress distribution similar to that observed in Fig. 61 for the bonded pellet-clad interfaces and debonded pellet-pellet interfaces without gaps. The pellets carry a large portion of the bending moment resistance via the pinching pellet corners, and they reduce the stress intensity at the bottom (compression) portion of the clad. The major difference compared with the results shown in Fig. 61 is the extensive stress concentration observed at the top region of the clad throughout the entire gauge section instead of the localized area observed at the interface region in Fig. 61. The clad assumes most of the bending moment resistance because of the lack of a direct mechanism for transferring load from pellet to clad or vice versa due to the debonded pellet-clad interfaces.

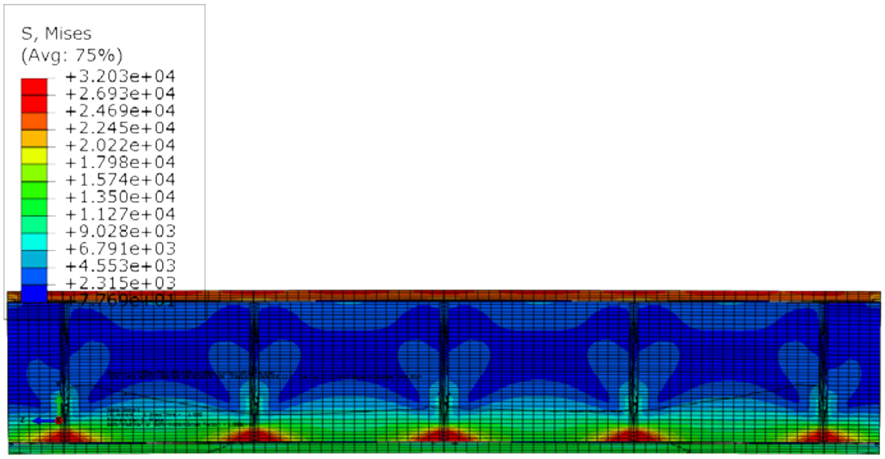

(a) Longitudinal section view of curvature and von Mises stress results

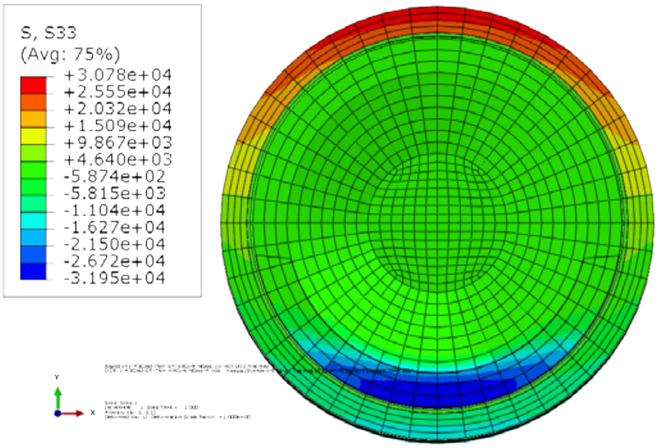

(b) Cross section view of the normal stress, σ_{zz}, results at a pellet-pellet interface

Fig. 67. Normal stress distribution and curvature results for the clad-epoxy-pellet section of HBR pellets without gaps at debonded pellet-pellet interfaces and with an epoxy layer at debonded pellet-clad interfaces.

In Fig. 68 (a), the shear stress in radial direction σ_{xy} shows different stress levels at the top tension side and bottom compression side at the clad. Similar to the normal stress distribution, the shear stress at the bottom side of the clad is significantly lowered by pellet-pellet direct pinching at the compression side. The shear stresses σ_{xz} and σ_{yz} appear indicate a stress pattern similar to that for interface debonding with gaps. However, the maximum stress levels are lower than that for those cases, again because the pellets assume a large portion of the bending load when the gaps are eliminated.

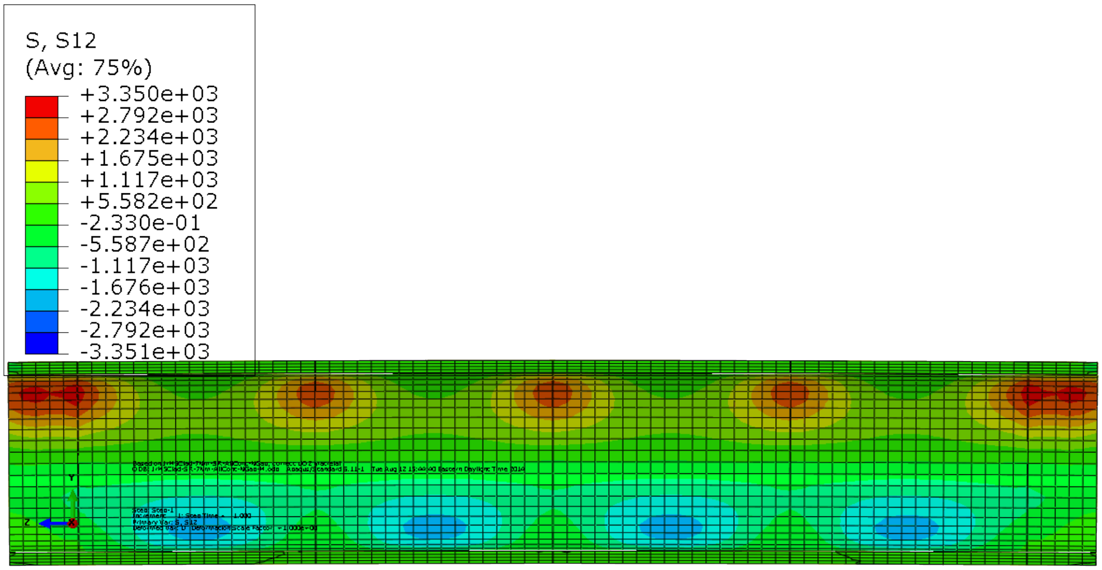

(a) Shear stress σ_{xy}

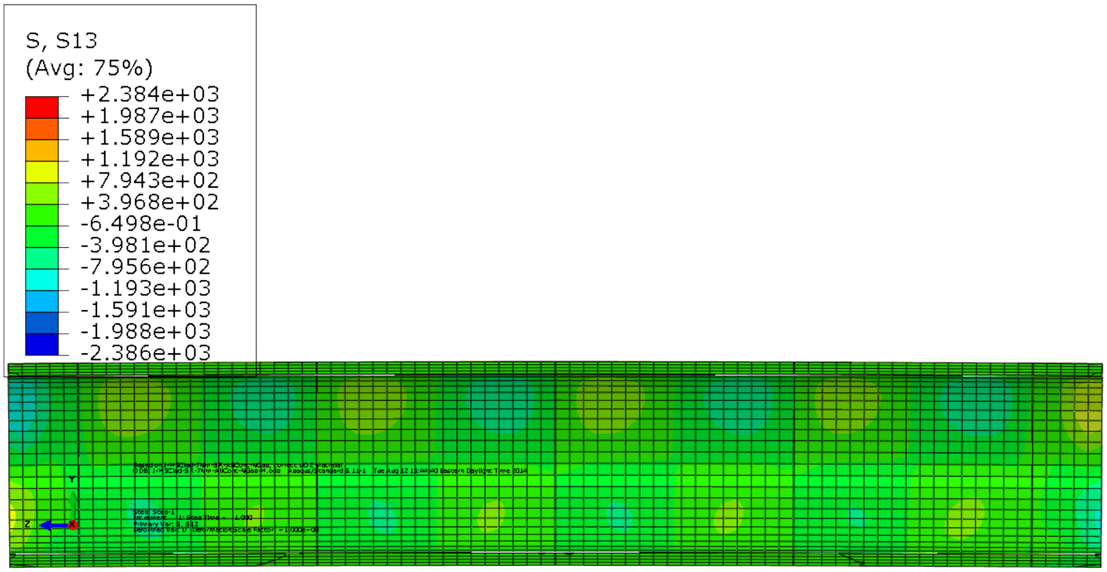

(b) Shear stress σ_{xz}

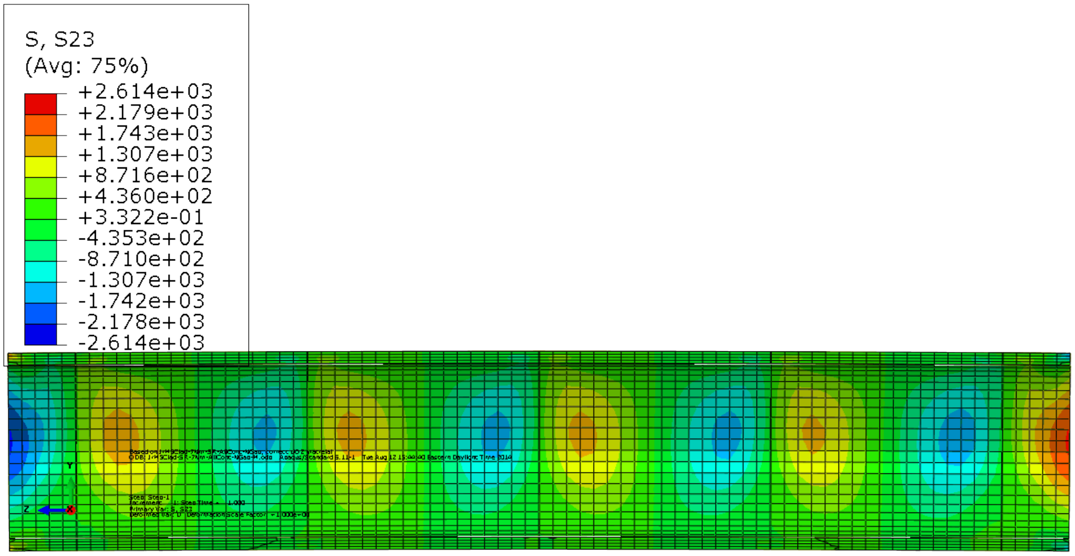

(c) Shear stress σ_{yz}

Fig. 68. Shear stress distribution and curvature results for the clad-epoxy-pellet section of HBR pellets without gaps at debonded pellet-pellet interfaces and with an epoxy layer at debonded pellet-clad interfaces.

Table 8. The curvature, flexural rigidity and bending moment comparison for debonded pellet-clad and pellet-pellet interfaces

	Curvature κ(1/m)	**Flexural rigidity EI ($N{\cdot}m^2$)**	**Clad bending moment M (N·m)**	**Pellet bending moment M (N·m)**
Pellet-pellet interface with gap debonded; pellet-clad interface debonded	0.462	16.5	7.51	0.11
Pellet-pellet interface without gap debonded; pellet-clad interface debonded	0.288	26.5	4.70	2.92

The gaps play an important role in flexural rigidity estimation. In Table 8, the flexural rigidity of the case without gaps at pellet-pellet interfaces is 1.6 times that of the case with gaps. In Table 7, the ratio of the flexural rigidity is 1.25 for the same comparison. The reason for the large increase in flexural rigidity is the direct pellet contact at the pellet-pellet interfaces at the compression side. The direct pellet-pellet contact interaction also provides a significant increase in bending moment resistance; it results in a much smaller curvature deformation, as shown in Table 8.

Table 8 also shows that the bending moment significantly shifts from pellet to clad with all interface debonding, especially when there are gaps at pellet-pellet interfaces. Clad takes 98.5% of the total bending load. When the pellets are in direct contact with one another, the pellets retake a large amount of the bending moment, which helps reduce the bending load on the clad.

5.3 Clad Curvature Estimation

The fuel rod bending curvature is derived from the clad deflection data. In CIRFT testing, there are three linear variable differential transformers (LVDTs) at two in. gauge sections of the fuel rod to measure three points of deflection on the clad outside wall (Fig. 69).

The curvature κ can be defined by the radius of circle R. Three deflection data at the clad outside wall can be used to determine the radius of circle R in Fig. 70, as follows:

$$\begin{cases}(U_{1y}-y)^2+(U_{1z}-z)^2=(U_{2y}-y)^2+(U_{2z}-z)^2=R^2\\(U_{1y}-y)^2+(U_{1z}-z)^2=(U_{3y}-y)^2+(U_{3z}-z)^2=R^2\end{cases} \tag{2}$$

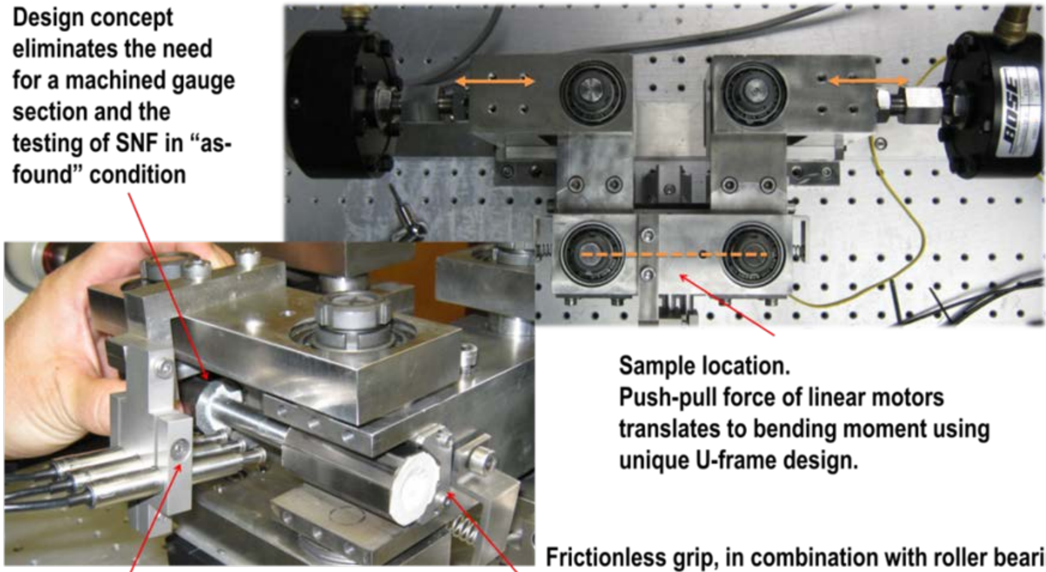

Design concept eliminates the need for a machined gauge section and the testing of SNF in “as-found” condition

Sample location.
Push-pull force of linear motors translates to bending moment using unique U-frame design.

Real-time, direct monitoring with three LVDT setup

Frictionless grip, in combination with roller bearing design, allows for lateral movement, eliminating an axial tensile loading during bending.

Fig. 69. CIRFT testing system with horizontal U-frame test setup integrated to Bose dual LM2 TB.

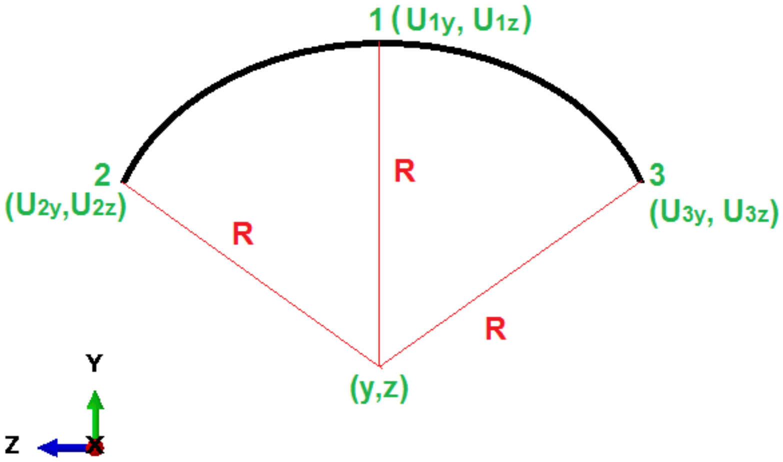

Fig. 70. Sketch for curvature calculation.

Solving Eq. (2), the center coordinate of curvature (y, z) can be obtained as

$$\begin{cases} y = \dfrac{B2*C1-B1*C2}{B2*A1-B1*A2} \\ z = \dfrac{A2*C1-A1*C2}{A2*B1-A1*B2} \end{cases}$$

$$Where \begin{cases} A1 = 2*U_{2y} - 2*U_{1y} \\ A1 = 2*U_{3y} - 2*U_{1y} \\ B1 = 2*U_{2z} - 2*U_{1z} \\ B2 = 2*U_{3z} - 2*U_{1z} \\ C1 = U_{2y}^2 + U_{2z}^2 - U_{1y}^2 - U_{1z}^2 \\ C2 = U_{3y}^2 + U_{3z}^2 - U_{1y}^2 - U_{1z}^2 \end{cases} \tag{3}$$

So the radius of circle R is

$$R = \sqrt{\left(U_{1y}-y\right)^2 + (U_{1z}-z)^2} = \sqrt{\left(U_{2y}-y\right)^2 + (U_{2z}-z)^2} = \sqrt{\left(U_{1y}-y\right)^2 + (U_{2z}-z)^2} \tag{4}$$

The curvature κ can be determined as

$$\kappa = \frac{1}{R} \tag{5}$$

The following sections discuss (1) the investigation of the curvature estimation using the clad deflection data based on both the global two in. gauge section and (2) the localized area where the testing probe cannot focus to determine the difference.

In this section, the cases of pellet-pellet interfacial debonding without gaps and pellet-clad interfaces with good bonding are used as examples to study curvature estimation. As seen in Fig. 71, the normal stress σ_{zz} result for this simulation is distributed nonuniformly in the two in. gauge section. As discussed in the previous section, at pellet-pellet interface debonded regions, the clad takes most of the bending moment, which results in stress concentration. The maximum stress in these regions is 27.1 ksi. At the middle of the pellet-clad bond region, the clad has relatively less stress, an average level of 10.5 ksi. There is significant deviation in stress distribution.

Therefore, two sets of deflection data were chosen to estimate curvature: one from the two in. gauge section, referred to as "global data," and the other from a finite localized area, referred to as "local data." The first two sets of induced deflection data were selected from the tension side of the clad under bending deformation in Fig. 71. One set of the deformed coordinates (U_{1y}, U_{1z}), (U_{2y}, U_{2z}) and (U_{3y}, U_{3z}) from three points at the outside wall of the clad in the global two in. section range was output to calculate the curvature by following Eqs. (2) and (5). The estimated curvature and resultant flexural rigidity are listed in Table 9 for comparison. The other set of data for curvature estimation was selected from the localized area, the enlarged area in Fig. 71. This localized area is at the pellet-pellet interface debonded region. The three points are located at a finite distance, where the LVDT cannot be focused in the testing. These three deformed coordinates were output to estimate curvature and flexural rigidity.

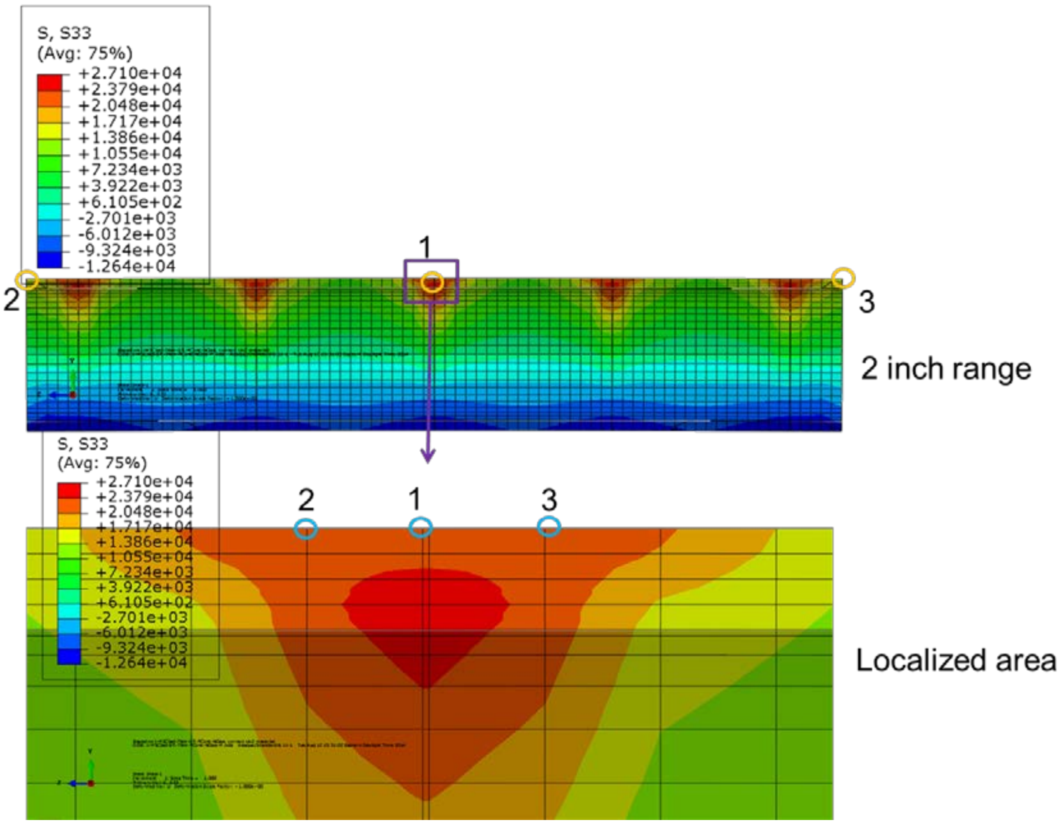

Fig. 71. Curvature estimations from the deflection data at the tension side of the clad for pellet-pellet interface debonded and pellet-clad interface bonded case.

The summarized results in Table 9 show a large difference in curvature estimation and associated flexural rigidity when the three deflection data points are chosen from the relatively global and local areas. The data from the two in. range result in a curvature only ⅓ that in the localized area at the pellet-pellet interface debonded region. The result is due to a lack of pellet support at the debonded interfaces. Therefore, the flexural rigidity estimated from global tensile clad deflection data is ~4 times that estimated from the local data. When a study cannot be completed by testing because of instrumentation limitations, it is important to depend on FEA simulation to investigate fuel rod behavior in detail, as shown in this example.

Table 9. Estimated curvature and flexural rigidity comparison from the tension side of the clad for case using epoxy as the interfacial material

	Curvature κ (1/m)	**Flexural rigidity *EI* (N·m^2)**
2 in. range	0.191	39.920
Localized area	0.684	11.141

The previous discussion established that for debonded pellet-pellet interfaces and bonded pellet-clad interfaces, pellet-pellet direct pinning at the compression side helps significantly lower the stress at the compression side of the clad. Following the same approach, two sets of deflection data were drawn from the compression side of the clad to estimate curvature in the two in. range and the localized area, as shown in Fig. 72.

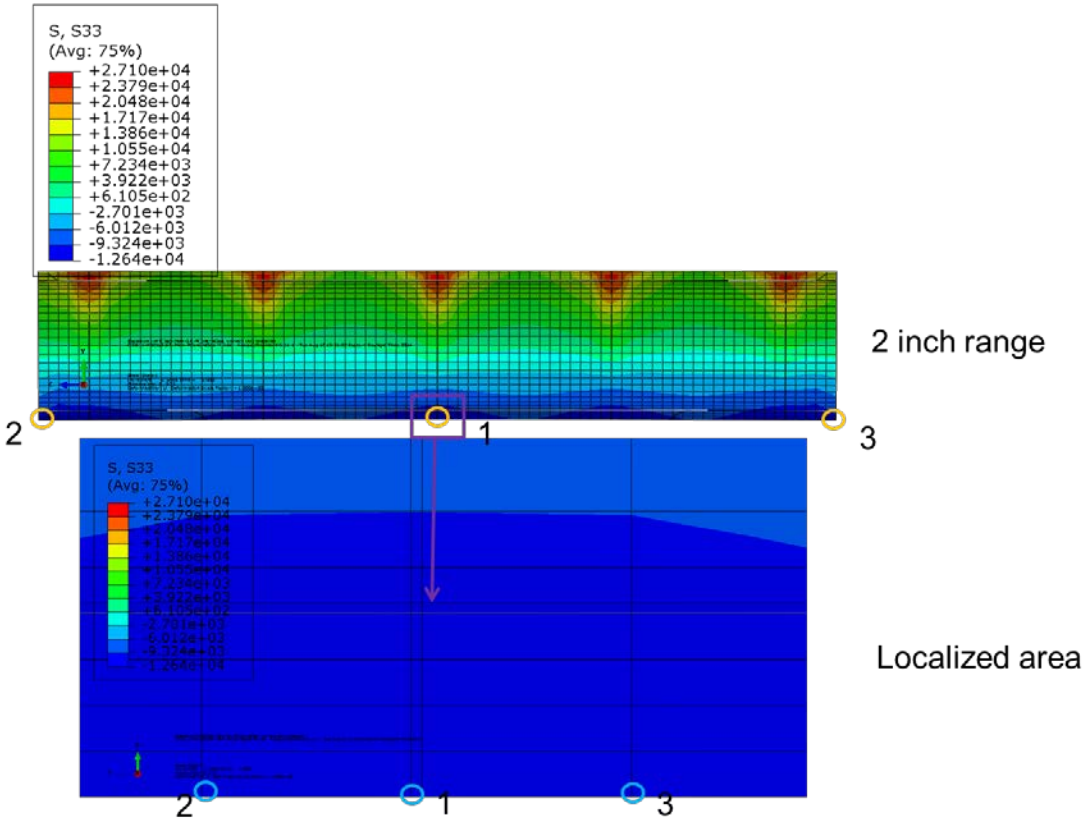

Fig. 72. Curvature estimations from the deflection data at the compression side of the clad for pellet-pellet interface debonded and pellet-clad interface bonded case.

The estimated curvature and flexural rigidity estimated from the deflection data at the compression side of the clad are compared in Table 10. The curvature estimated locally is still 16% higher than the curvature estimated globally, which results in a 16% reduction in flexural rigidity. Compared with the estimation at the tension side in Table 9, the curvature and flexural rigidity estimated from deflection data in the global two in. gauge section range are the same. That is because globally, the nonuniform stress distribution averages out, although the curvature estimated in the localized area from the compression side is only ⅓ that estimated from the tension side. With pellet-pellet debonding at the clad compressive stress region, pellet-pellet pining still provides support for resisting flexural deformation. Therefore, locally, the flexural rigidity on the compression side is triple that on the tension side.

Table 10. Estimated curvature and flexural rigidity comparison from the compression side of the clad for the case using epoxy as the interface material

	Curvature κ (1/m)	**Flexural rigidity *EI* (N·m^2)**
2 in. range	0.192	39.659
Localized area	0.228	33.406

5.4 DISCUSSION

Based on FEA simulation results and further verification from M5^{TM} fuel rod bending test results, the impacts of interfacial bonding efficiency at pellet-pellet and pellet-clad interfaces on the M5^{TM} fuel rod performance can be summarized as follows.

With good interface bonding and without fuel pellet and clad fracturing, the pellets in the fuel rod will carry more bending moment resistance than the clad under NCT vibration. The maximum stress resides in the pellets, and the stresses at the clad and pellet are both below the yield condition. Therefore, the system is in a linear elastic state under the target bending loads. There is no shear stress surge inside the M5^{TM} cladding.

Upon fuel pellet failure, including debonding at the pellet-pellet interfaces, the load-carrying capacity shifts from the fuel pellets to the clad. The clad starts to carry most of the bending moment at the pellet-pellet interface region, resulting in localized stress concentrations in the clad. However, under the target bending moment, the clad does not yield. With good cohesion bonding at the pellet-clad interfaces, the pellets can continue to support the clad and carry a sufficient portion of the bending moment resistance. Therefore, most of the clad at the gauge section remains in the linear elastic range. A shear stress surge occurs inside the cladding at the pellet-pellet interface regions.

When further debonding occurs at the pellet-clad interfaces, the embedded pellets can no longer provide effective structural support to the clad; nor can they assist load transfer within the fuel rod system. Thus most of the load-carrying capacity shifts to the clad throughout the entire gauge section. The shift leads to maximum stress concentrations in the clad in the entire gauge section instead of at localized pellet-pellet interface regions.

When the pellets contact and pinch one another, they tend to take over a significant portion of the bending load resistance, especially where there are no gaps at the pellet-pellet interfaces. This pellet pinning action clearly mitigates and avoids stress concentration and potential yielding at the compression side of the clad.

All of the simulation cases are summarized in Table 11. The main parameter flexural rigidity *EI* is compared case by case. The immediate consequences of interface debonding are (1) a shift in the load-carrying capacity from the fuel to the clad and (2) a reduction in flexural rigidity. For example, the flexural rigidity is 44 N·m^2 when the pellets are perfectly bonded with epoxy. In the case with gaps at the pellet-pellet interfaces, when there is debonding at the pellet-pellet interfaces alone, the flexural rigidity drops by 27% to 32 N·m^2. In the case without gaps, it drops by 9% to 40 N·m^2. Further debonding at the pellet-clad interfaces causes the flexural rigidity to drop further in the cases with gaps by 48% and in the cases without gaps by 34%. Overall, between the perfect bond and the debond cases at all interfaces, flexural rigidity drops by about 62.5% for cases with gaps and 40% for cases without gaps.

Table 11 shows a flexural rigidity about 20–38% higher for the fuel rod without gaps, indicating a significant increase in system stiffness over the case with gaps. Therefore, the gaps at the interfaces of the fuel rod system have a significant impact on system reliability, especially at pellet-pellet interfaces. The flexural rigidity and bending moment resistance capacity of the fuel rod are highly dependent on interface bonding efficiency at pellet-clad and pellet-pellet interfaces. This discovery was validated by ORNL reversal bending fatigue test results performed on the fuel rod with M5^{TM} cladding.

Table 11. The flexural rigidity comparison between the different bonding and debonding cases

Interface bonding conditions	Flexural rigidity *EI* (N·m^2)	Reduction from perfect bond (%)	Reduction from only pellet-pellet debond to further pellet-clad debond (%)	Increase from with gaps to without gaps (%)
Perfect bond	44			
Pellet-pellet interface with gap debond, pellet-clad interface bonded	32	27		
Pellet-pellet interface without gap debond, pellet-clad interface bonded	40	9		20
Pellet-pellet interface with gap debond, pellet-clad interface debonded	16.5	62.5	48	
Pellet-pellet interface without gap debond, pellet-clad interface debonded	26.5	40	34	38

The estimates for curvature and the associated flexural rigidity vary widely between three deflection data points chosen from a relatively global area and a local area. Because of a lack of pellet support at the debonded interface, the local tensile clad curvature is ~4 times that of the global curvature at the tension side of the clad. At the compression side of the clad, the curvature and flexural rigidity estimated from the deflection data in the global two in. gauge section range are the same. However, the curvature estimated in a localized area from the compression side is approximately ⅓ the estimated curvature from the tension side. With pellet-pellet debonding at the clad's compressive stress region, pellet-pellet pinning continues to provide good support to resist flexural deformation. Therefore, the flexural rigidity estimated from the local compression side is triple that estimated from the local tension side.

Based on previous study [14–15], the length of fuel pellets can also have significant impact on system stiffness. Longer pellets would result in higher flexural rigidity.

6 FRACTOGRAPHY

PIE study was performed by using an optical microscope in an ORNL hot cell on the fractured/failed CIRFT specimens, including HBR R4, NA1, NA2, NA4, MOX1 and MOX2 [17]. The failed specimens were tested under pure dynamic loading, except MOX1, in which the dynamic loading followed the static loading cycles discussed in Section 4.6.1. The fracture surfaces for these specimens are presented in Figs. 73–78.

The fracture topography observed in HBR R5 indicated that the failure mode includes the fuel pellets fractured. The stressed surface of the tested rod revealed equally spaced circumferential cracks as reported in Ref. [11]. These cracks apparently are related to the oxide layers of cladding.

No obvious circumferential cracks were seen on the stressed surface of NA and MOX fuels, partly due to low image resolution and the dark grease appearance on the tested rod surface. The failure of NA fuels predominately occurred at the pellet-to-pellet interface. The failure of the two MOX specimens seemingly took place within a fuel pellet where no identifiable mark of pellet ends can be seen from the matching halves of fracture surfaces. The underlying failure mechanism for these MOX fuels remains to be explored.

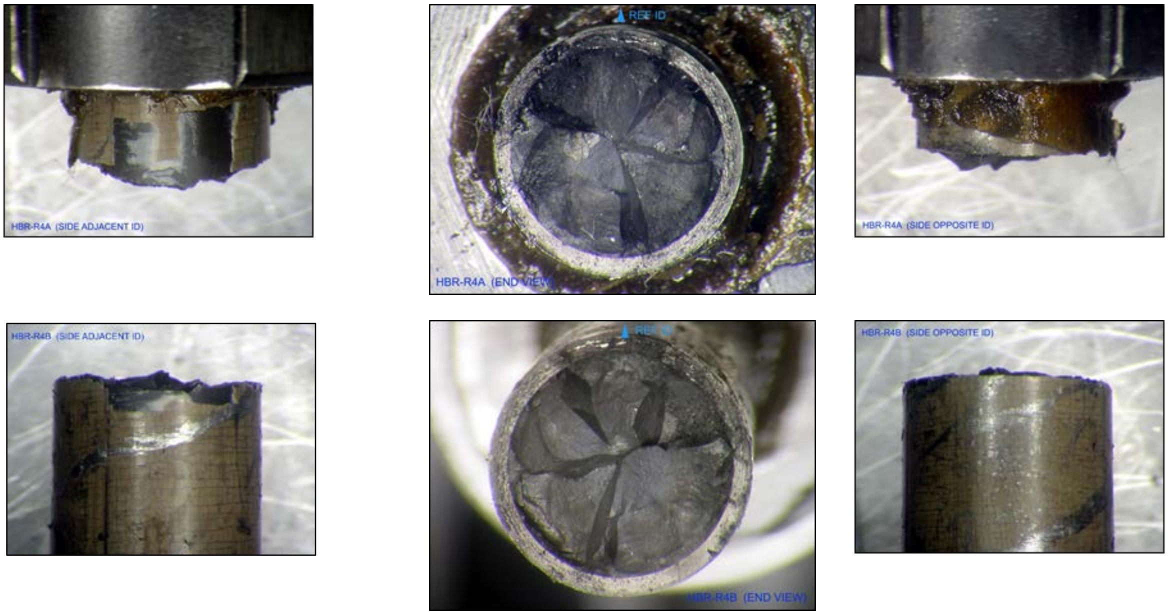

(a) (b) (c)

Fig. 73 (a) Lateral or front view, (b) transverse view, and (c) back view of fracture surface for HBR R4 tested under ±8.89 N·m 5Hz. $N_f = 2.7 \times 10^5$ cycles.

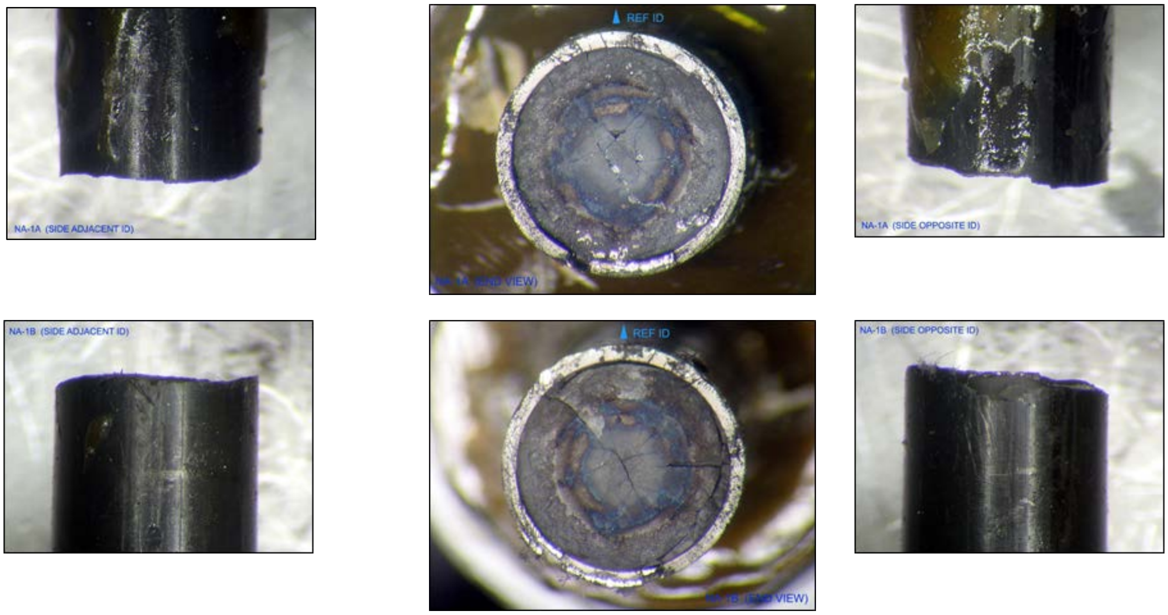

(a) (b) (c)

Fig. 74 (a) Lateral or front view, (b) transverse view, and (c) back view of fracture surface for NA1 tested under ±12.7 N·m 5Hz, $N_f = 1.57 \times 10^4$ cycles.

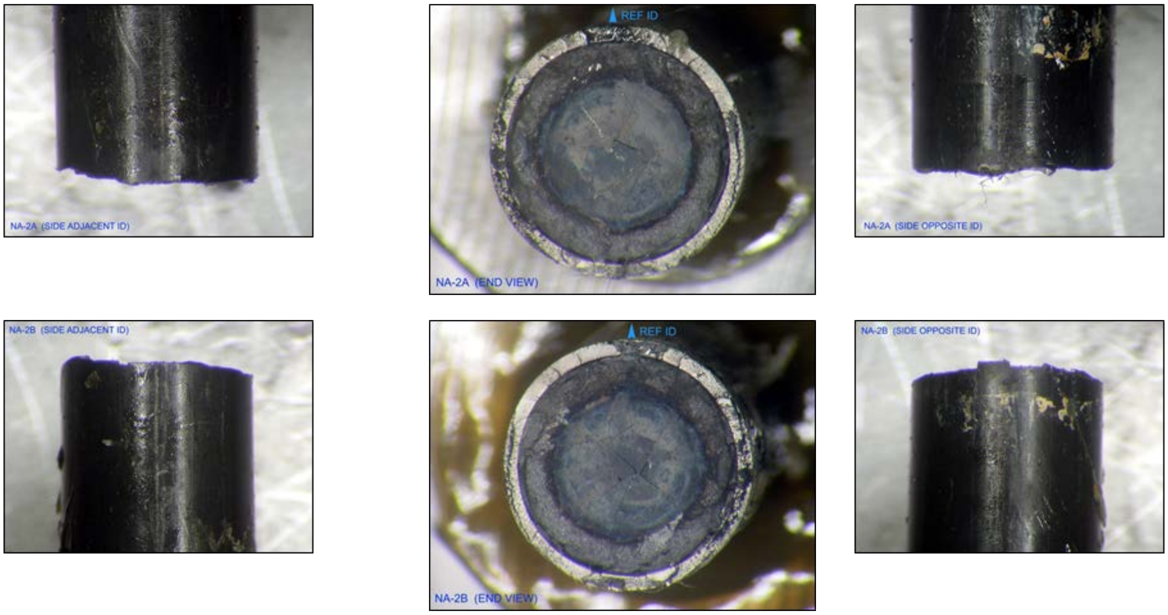

(a) (b) (c)

Fig. 75 (a) Lateral or front view, (b) transverse view, and (c) back view of fracture surface for NA2 tested under ±10.16 N·m 5Hz, $N_f = 2.20 \times 10^4$ cycles.

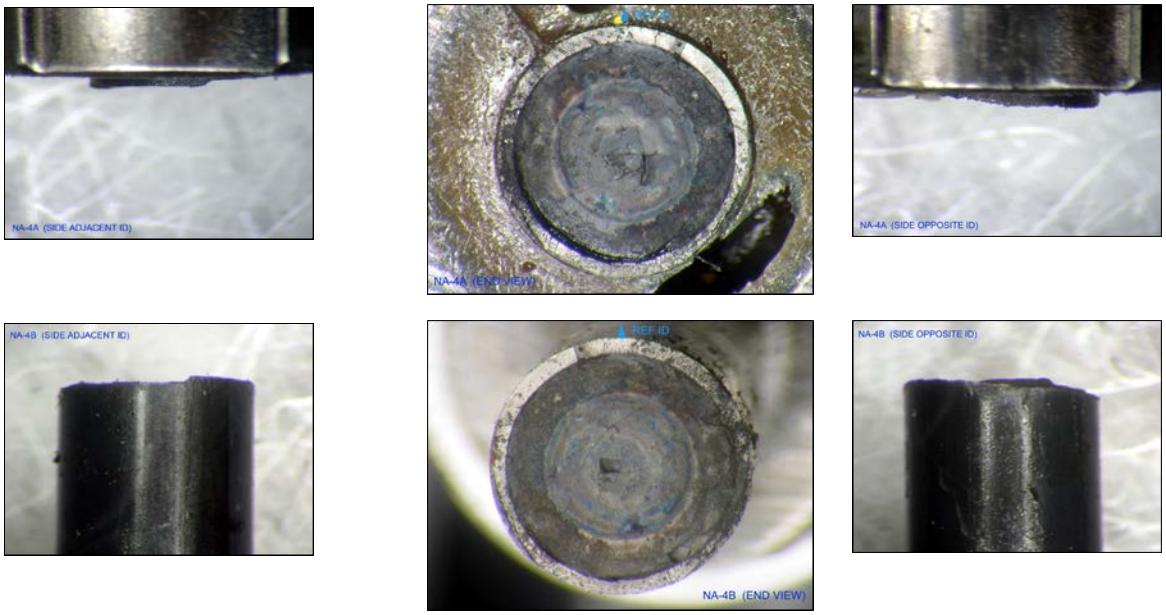

(a) (b) (c)

Fig. 76 (a) Lateral or front view, (b) transverse view, and (c) back view of fracture surface for NA4 tested under ±7.62 N·m 5Hz, $N_f = 6.10 \times 10^4$ cycles.

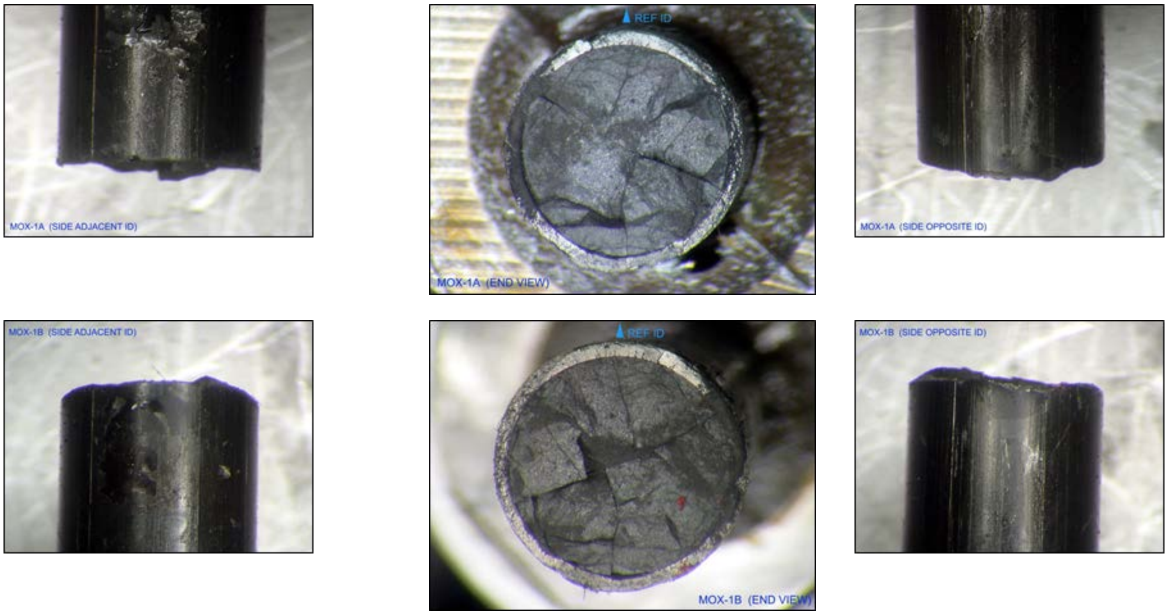

(a) (b) (c)

Fig. 77 (a) Lateral or front view, (b) transverse view, and (c) back view of fracture surface for MOX1 tested first to 47 N·m for two cycles and then dynamic loading under ±15.24 N·m 5Hz, N_f = 4.0×10^3 cycles.

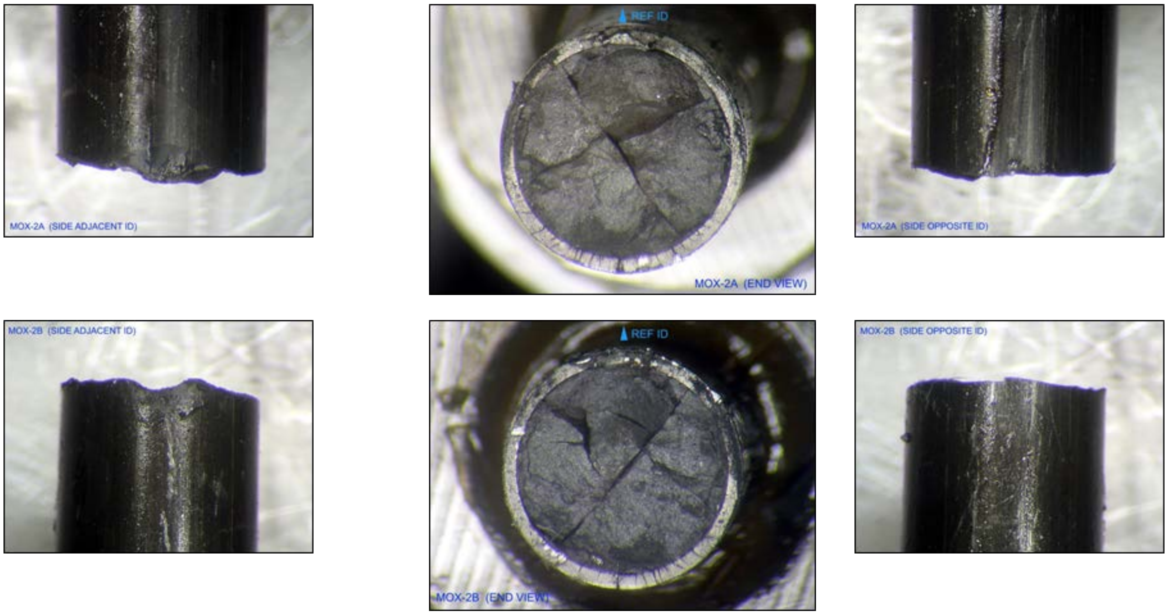

(a) (b) (c)

Fig. 78 (a) Lateral or front view, (b) transverse view, and (c) back view of fracture surface for MOX2 tested under dynamic loading ±10.16 N·m 5 Hz, N_f = 3.70 $\times10^4$ cycles.

7 CONCLUSION

The CIRFT was conducted on three HBR rods (R3, R4, R5); two specimens failed and one specimen did not fail. The total number of cycles in the test of nonfailed specimens went over 2.23×10^7; the test was stopped because the specimen did not show any sign of failure. Data analysis demonstrated that it is necessary to characterize the fatigue life of UNF rods in terms of both the curvature amplitude and the maximum of absolute curvature extremes. The latter is significant because the maxima of extremes signify the maximum of tensile stress of the outer fiber of the bending rod. A large range of hydrogen content has been covered in CIRFT on HBR rods. The load amplitude has been the dominant factor that controls the fatigue life of rods, but the hydrogen content also has an important effect on the fatigue life, as illustrated in Fig. 14.

A preliminary post-irradiation examination was conducted on some selected rod segment/specimens. A large volume of data is made available on fracture systems within pellets, pellet-to-pellet interaction conditions, and hydrides.

A new vise mold was designed and fabricated that is dedicated to rod specimen preparation for NA M5^{TM} and MOX fuels. Epoxy casting in the hot cell demonstrated that the second vise mold works just as effectively as the first one.

The static testing on NA and MOX samples was carried out under displacement control: relative maximum displacement of 24.00 mm (12.00 mm at each motor) with a loading rate of 0.1 mm/s, followed by an unloading rate of 0.2 mm/s at each loading point of the U-frame. The moment–curvature curves and equivalent stress-strain curves were recorded. There was a significant nonlinear deformation after 30 N·m, and a maximum moment of 47 N·m was attained during the initial loading cycle. A deflection point appeared at approximately 8 N·m in this initial loading cycle. Subsequent loading cycles did not produce additional deformation, but a closed hysteresis loop was introduced. The maximum curvature under a relative displacement of 24.00 mm was 3.85–4.1 m^{-1}. The maximum equivalent stress was 520–522 MPa, and the maximum equivalent strain was 1.8–2.0%.

Seven dynamic tests at 5 Hz were conducted in the hot cell: three NA M5^{TM} specimens and four MOX specimens. The moment amplitudes tested were 5.08–12.70 N·m, and the curvature amplitudes were 0.200–0.55 m^{-1}. The equivalent stress amplitudes were 59.12–142.37 MPa, and the equivalent strain amplitudes were 0.10–0.27 %. The fatigue life of the rods decreased from 2.15×10^6 to 1.57×10^4 cycles. It is noted here that the dynamic test also reveals the potential accelerated aging from the drop during handling or the transient shocks of NCT.

LVDTs for curvature measurement in the second CIRFT have been upgraded with rad-hardened grade LVDTs (three RDP D5/200AG-337 with stroke ±5 mm). The second CIRFT continues to demonstrate the effectiveness of out-of-cell testing in addressing the issues related to in-cell testing. When the sign of curvature is changed and the curvature becomes large simultaneously, the difference in curvature measurement implies the impact that LVDT probe contact may have on the curvature measurement.

Based on a series of FEA simulations on M5^{TM} clad, the impact of the interface bonding efficiency on UNF vibration integrity, the distribution of moment carrying capacity between pellets and clad, and the impact of the interface material on the flexural rigidity of the M5^{TM} fuel rod system are all important factors to be considered when evaluating the clad/fuel system under NCT. As the Young's modulus of the interface material increases, the fuel rod system stiffness increases accordingly. As debonding of the pellet-clad interface advances, the impact of the interface material property change is limited.

The immediate consequences of interface debonding are a shift in load-carrying capacity from the fuel pellets to the clad and a reduction in composite rod system flexural rigidity. Therefore, the flexural rigidity of the fuel rod and the bending moment resistance capacity between the clad and fuel pellets are highly dependent on the interface bonding efficiency at the pellet-pellet and pellet-clad interfaces. Furthermore, the curvature and associated flexural rigidity estimates based on global measurement of

CIRFT tests are very different from the localized clad data estimated by FEA. As a result of the lack of pellet support at the debonded interface, the local tensile clad curvature is ~3 to 4 times that of the global curvature at the tension side of the clad.

ACKNOWLEDGMENTS

This research was sponsored by the DOE Used Fuel Disposition Campaign (UFDC) and NRC under DOE contract DE-AC05-00OR22725 with UT-Battelle, LLC. Authors thank ORNL program managers Bruce Bevard and Rob Howard for their support and guidance during the project; Chuck Baldwin for PIE, Josh Schmidlin for fuel rod cutting and dimension measurement; Bryan Woody and Scot Thurman for hot-cell operation support; and Brian Sparks and Randy Parten for drawing and machining support.

REFERENCES

1. J.-A. J. Wang and H. Wang, *Progress Letter Report on Reversal Bending Fatigue Testing of Zry-4 Surrogate Rod (Out-of-Cell Fatigue Testing Development–Task 2.4)*, ORNL/TM-2013/297, Oak Ridge National Laboratory, Oak Ridge, Tenn., August 2013.
2. J.-A. J. Wang et al., *Reversible Bending Fatigue Test System for Investigating Vibration Integrity of Spent Nuclear Fuel During Transportation*, PATRAM 2013, DOE/NRC/DOT, San Francisco, Calif., August 18–23, 2013.
3. J.-A. J. Wang et al., *Progress Letter Report on Bending Fatigue Test System Development for Spent Nuclear Fuel Vibration Integrity Study (Out-of-Cell Fatigue Testing Development–Task 2.4)*, ORNL/TM-2013/225, Oak Ridge National Laboratory, Oak Ridge, Tenn., July 2013.
4. H. Wang, J.-A. J. Wang et al., "Development of U-frame Bending System for Studying the Vibration Integrity of Spent Nuclear Fuel," *Journal of Nuclear Materials* 440, 201–13 (2013).
5. J.-A. J. Wang et al., *SNF Test System for Bending Stiffness and Vibration Integrity*, International High-Level Radioactive Waste Management Conference, Albuquerque, N.M., April 28–May 2, 2013.
6. J.-A. J. Wang, H. Wang, and Ting Tan, *An Innovative Dynamic Reversal Bending Fatigue Testing System for Evaluating Spent Nuclear Fuel Rod Vibration Integrity or Other Materials Fatigue Aging Performance*, ORNL Invention Disclosure 201102593, DOE S-124,149, April 8, 2011. Patent in review, 13/396,413, February 14, 2012.
7. J.-A. J. Wang et al., *Progress Letter Report on U-Frame Test Setup and Bending Fatigue Test for Vibration Integrity Study (Out-of-Cell Fatigue Testing Development–Task 2.3)*, ORNL/TM-2012/417, Oak Ridge National Laboratory, Oak Ridge, Tenn., August 2012.
8. J.-A. J. Wang et al., *Progress Letter Report on U-Frame Test Setup and Bending Fatigue Test for Vibration Integrity Study (Out-of-Cell Fatigue Testing Development–Task 2.2)*, ORNL/TM-2011/531, Oak Ridge National Laboratory, Oak Ridge, Tenn., January 2012.
9. J.-A. J. Wang et al., *High Burn-up Spent Fuel Vibration Integrity Study Progress Letter Report (Out-of-Cell Fatigue Testing Development–Task 2.1)*, ORNL/TM-2010/288, Oak Ridge National Laboratory, Oak Ridge, Tenn., January 2011.
10. J.-A. J. Wang and H. Wang, *2014 Semi-Annual Progress Letter Report on Used Nuclear Fuel Integrity Study in Transportation Environments*, ORNL/TM-2014/63, Oak Ridge National Laoboratory, Oak Ridge, Tenn., April 2014.
11. J.-A. J. Wang and H. Wang, *Mechanical Fatigue Testing of High-Burnup Fuel for Transportation Applications*, ORNL/TM-2014/214, Oak Ridge National Laboratory, Oak Ridge, Tenn., August 2014
12. C. Baldwin, Oak Ridge National Laboratory, Oak Ridge, Tenn., June 2013.
13. J. E. Schmidlin, *Information about NA Fuel Segment Measurements*, Oak Ridge National Laboratory, Oak Ridge, Tenn., July 2, 2014.

14. J.-A.J. Wang, H. Jiang, and H. Wang, Using Surrogate Rods to Investigate the Impact of Interface Bonding Efficiency on Spent Nuclear Fuel Vibration Integrity, ORNL/LTR-2014/257, Oak Ridge National Laboratory, Oak Ridge, Tennessee, 2014.
15. H. Jiang, J. J. A. Wang, and H. Wang, “Potential Impact of Interfacial Bonding Efficiency on Used Nuclear Fuel Vibration Integrity during Normal Transportation,” Proceedings of the ASME 2014 Pressure Vessels and Piping Conference, PVP2014-29117, Anaheim, California, July 2014.
16. R. N. Morris, et. al., “MOX PIE Fuel and Clad Examination Final Report,” ORNL/MD/LTR-352 Rev 2, September 2013.
17. C. A. Baldwin, Fracture Surface Images of Selected CIRFT Tested Samples, Oak Ridge National Laboratory, Oak Ridge, Tenn., August 2013.